

A Study on Uniquely Modified Diamond, Diamond/ β -SiC Nanocomposite and Graphene Nitride (g-C₃N₄) Surfaces

A thesis submitted by

Bommidi Vara Lakshmi

(Reg. No. 12ENPH04)

in the partial fulfillment of the requirement for the award of the degree of

Doctor of Philosophy

in

Nano Science and Technology

Under the supervision of

Dr.-Ing. V. V. S. S. Srikanth



School of Engineering Sciences and Technology
University of Hyderabad
Central University (P.O.)
Hyderabad 500046
India

Declaration

I, **Bommidi Vara Lakshmi**, declare that this thesis work entitled “**A Study on Uniquely Modified Diamond, Diamond/ β -SiC Nanocomposite and Graphene Nitride (g -C₃N₄) Surfaces**”, submitted in partial fulfillment of the requirement for the award of **Doctor of Philosophy (Nano Science and Technology)** in the School of Engineering Sciences and Technology, University of Hyderabad is completely my work except for those referenced. This work was done under the supervision of **Dr.-Ing. V. V. S. S. Srikanth**. This thesis is a record of the bonafide research work carried out by me. The results incorporated in this thesis have not been reproduced/copied from any source. This work has not been submitted to any other University or Institution for the award of any other degree or equivalent.

Bommidi Vara Lakshmi

Reg. No.: 12ENPH04

School of Engineering Sciences and Technology

University of Hyderabad



Certificate

This is to certify that the thesis entitled A Study on Uniquely Modified Diamond, Diamond/ β -SiC Nanocomposite and Graphene Nitride (g -C₃N₄) Surfaces submitted by Bommidi Vara Lakshmi bearing registration number 12ENPH04 (Ph.D. (Nano Science and Technology)) in partial fulfillment of the requirements for award of Doctor of Philosophy in the School of Engineering Sciences and Technology is a bonafide work carried out by him under my supervision and guidance.

This thesis is free from plagiarism and has not been submitted previously in part or in full to this or any other University or Institution for award of any degree or diploma.

Parts of this thesis have been:

A. Published in the following publications:

1. *Nuclear Instruments and Methods in Physics Research Section B: Beam Interactions with Materials and Atoms* 379, 167-170 (2017) (ISSN number: 0168-583X), Chapters 3 and 4

and

B. Presented in the following conferences:

1. *Two Decades of Ion Beam Analysis at 3MV Tandetron-2017* (National)
2. *ICFONM-2016* (International)
3. *NCCM-2015* (National)
4. *REI-18-2014* (International)
5. *IUMRS-ICA 2013* (International)

Further, the student has passed the following courses towards fulfillment of the coursework requirement for Ph.D.

| Course Code | Name | Credits | Pass/Fail |
|-------------|--|---------|-----------|
| AC801 | Research Methodology | 4 | Pass |
| NT401 | Thermodynamics and Phase Equilibria | 4 | Pass |
| NT403 | Characterization of Materials | 4 | Pass |
| NT405 | Advanced Engineering Mathematics | 2 | Pass |
| NT406 | Materials Processing and Characterization Laboratory | 4 | Pass |
| NT407 | Concepts of Nano Science and Technology | 4 | Pass |
| NT408 | Synthesis and Applications of Nanomaterials | 4 | Pass |
| NT457 | Laboratory | 4 | Pass |
| NT458 | Seminar | 2 | Pass |

Supervisor

Dean of School

Acknowledgments

I express with great pleasure my sincere gratitude to my thesis supervisor Dr.-Ing. V. V. S. S. Srikanth for his patience, constant encouragement, constructive criticism, guidance, and timely and cheerful co-operation throughout my PhD studies. I would like to thank my doctoral review committee members, Dr. Koteswararao V. Rajulapati and Dr. Jai Prakash Gautam for their valuable suggestions during the review meetings. I would like to express my gratitude to Prof. K. Bhanu Sankara Rao former Dean, Prof. M. Ghanashyam Krishna, Dean and all faculty members of School of Engineering Sciences and Technology (SEST), University of Hyderabad (UoH). I would also like to take this opportunity to sincerely thank Prof. S. V. S. Nageswara Rao, School of Physics (SoP), UoH for his advice, which initiated my admission into this school. My thanks also to the lab technicians and non-teaching staff, SEST, UoH, for their help.

My sincere thanks to Dr. K. Asokan, Scientist G, Inter University Accelerator center (IUAC), New Delhi for readily allowing me to carry out ion beam irradiation experiments and characterization in his laboratory on electrical conductivity measurements. I would also like to thank Mr. Sunil Ojha and Mr. Umapati, Scientists in IUAC, New Delhi, who helped me in Rutherford backscattering measurements and analysis.

I am also thankful to Dr. Ahamed, and Mr. Muvva D Prasad for helping me in carrying out Raman spectroscopy and transmission electron microscopy experiments, respectively. I would like to thank Ms. Sunita and Mr. Naresh, technical staff in SoP, UoH. I feel great to acknowledge Dr. K. Mohan Kumar, Mr. K. V. Sreenivasulu, Mrs. Regala Aneela and Mrs. Sravani for helping me at various stages of my PhD studies.

The word 'thanks' is just not enough to express my gratitude towards my beloved parents Sri. B. V. S. R. Sastry and Smt. Rajya Lakshmi, in laws Sri. K. S. R.Sarma and Smt. Sailaja, sisters Rukmini, Vijaya Lakshmi and their families for their unfaltering love and continuous support. Special thanks to my husband Mr. K. Phaneendra for his constant support, help and suggestions at various stages of my research work, and his moral support without which I could not have come to the finishing stage of my PhD degree.

Finally, I dedicate this work to my parents, sisters and my husband who are my strength. I will remain ever grateful to DST, India for providing me INSPIRE fellowship.

Bommidi Vara Lakshmi

Table of Contents

| | |
|---|----|
| Abstract..... | i |
| Chapter 1 Introduction..... | 1 |
| 1.1 General Background..... | 1 |
| 1.2 Importance of Surface Modification | 1 |
| 1.3 Gamma Irradiation of Materials | 2 |
| 1.4 Ion Beam Technology | 3 |
| 1.5 Problem Definition and Objectives | 7 |
| 1.6 Overview of the Thesis..... | 8 |
| References | 8 |
| Chapter 2 Literature Review | 12 |
| 2.1 Gamma Rays Irradiated Diamond..... | 12 |
| 2.2 Ion Irradiated Diamond | 13 |
| 2.3 Graphene Nitride | 14 |
| 2.4 Metal-Insulator-Semiconductor Devices | 16 |
| References | 18 |
| Chapter 3 Experimental Work | 24 |
| 3.1 Synthesis of Materials..... | 24 |
| 3.1.1 Synthesis of diamond and diamond/ β -SiC composite thin films | 24 |
| 3.1.2 Graphitic carbon nitride (g - C_3N_4)..... | 25 |
| 3.2 Surface Modification Procedures | 26 |
| 3.2.1 Gamma irradiation | 26 |
| 3.2.2 Ion irradiation..... | 26 |
| 3.3 Characterization | 32 |
| 3.3.1 Electron microscopy | 32 |
| 3.3.2 X-ray and electron diffraction..... | 32 |
| 3.3.3 Spectroscopy | 32 |
| 3.3 Mechanical Contact Damage Tests | 34 |
| 3.4 Electrical Conductivity Measurements..... | 35 |
| Chapter 4 Results and Discussion | 38 |
| 4.1 Gamma (γ) Irradiated Diamond Thin Films..... | 38 |
| 4.1.1 Characteristics of as-deposited diamond thin films..... | 38 |

| | |
|--|-----------|
| 4.1.2 Characteristics of the γ -irradiated diamond thin films | 42 |
| 4.2 Nitrogen Irradiated Diamond Thin Films | 47 |
| 4.3 Indentation Behavior of Diamond and Diamond/β-SiC Thin Films | 67 |
| 4.4 Electrical Conductivity of Diamond/β-SiC Thin Films | 69 |
| 4.5 Si Irradiated g-C₃N₄..... | 71 |
| References | 76 |
| Chapter 5 Conclusions and Future Scope | 79 |
| 5.1 Conclusions..... | 79 |
| 5.2 Future Scope..... | 80 |

Abstract

Diamond and diamond/ β -SiC composite films are being widely studied for their wear resistant, structural and electronic properties. Of the various methods researchers use to modify the structure of these films, using irradiation techniques in particular are of interest due to their versatility. This thesis work was carried out to: (i) understand the indentation damage and electrical properties of diamond/ β -SiC nanocomposite thin films, (ii) modify (i.e., phase, structural and/or morphological) the diamond films by using ion beam implantation/irradiation technique, (iii) modify the surface morphology of g-C₃N₄ by using ion implantation/irradiation, (iv) Fabricate the metal-insulator-semiconductor active structures in diamond films. The forms of diamond and diamond/ β -SiC nanocomposite films resulting from such modifications are investigated using Raman spectroscopy in conjunction with scanning electron microscopy and x-ray diffraction were carried out to understand the microstructure and phase information. Also as-grown diamond/ β -SiC nanocomposite films are investigated with mechanical and electrical testing. The impact of these characterizations will provide the valuable perspective to researchers in materials science. Understanding the changes to the structure and properties of this class of thin films which can be induced through various mechanisms will allow future researchers to refine these films towards technological applications in areas of hard coatings, electronics and biosensing. Raman scattering experiments in conjunction with scanning electron microscopy and x-ray diffraction were carried out to extract microstructure and phase information of the gamma and nitrogen ion irradiated diamond thin film surfaces. The γ -irradiation of diamond films showed no phase, surface and structural changes. The nitrogen ion implantation with 100 keV results increase in sp²-C network in diamond films which leads to improve the surface conductivity of these films. This nitrogen ion implantation of diamond films fabricate the metal-insulator-semiconductor (MIS) active surfaces which are used in electronic device applications. The graphene nitride (g-C₃N₄) materials are used in energy applications. The silicon implanted/irradiated g-C₃N₄ showed sheet like morphology with stable phase and structure of graphene nitride which are used in lithium ion batteries applications.

Chapter 1 Introduction

1.1 General Background

In recent years, diamond and β -SiC thin films [1, 2] have attracted great interest due to their several superlative characteristics like high thermal stability, high radiation resistance, high chemical stability, high melting point, wide band gap, high hardness, low erosion rate etc., that make them excellent candidates for high temperature, high power and high voltage and other related applications [3-5]. Another material that has equally attracted interest in recent times is graphene nitride (g-C₃N₄), which has outstanding chemical and thermal stabilities, which in turn have been used to design favorable metal-free photo catalytic reactions like splitting water [6, 7], pollutant degradation [8-10] and oxidative dehydrogenation of amines [11]. g-C₃N₄ is also used in gas storage [12]. It has unique semiconducting properties and exhibits unusual catalytic activities in a variety of reactions including “artificial photosynthesis”. It can be used in diverse applications such as electronic displays, tribology, proton exchange membrane fuel cell catalyst, hydrogen production, etc. Recently, graphene nitrides have also been touted as excellent materials for energy solutions [13]. However, to realize the potential applications of the above mentioned materials, their surfaces have to be uniquely modified to influence the enhancement in their properties.

1.2 Importance of Surface Modification

Surface modification is an effective means to tailor the physical, chemical and biological properties (that are different from original ones) of materials. The main purpose of surface modification includes enhancing anti-corrosive properties, electrical conductivities, and bioactivities. In order to enhance the functionality [15, 16] of materials, different modification techniques are in use. The methods of surface modification vary with different materials. The most commonly used surface modification techniques, depending on the applications are sacrificial agents' addition [17], mesostructure introduction [18], noble metals deposition [19], compositing semiconductors [20,21], nanostructures engineering [22, 23], surface roughening [24, 25], surface patterning [9, 26-28], chemical modification of surfaces [9,29.30], doping [31-34], irradiation [35-38], and so on. Very often, a combination of these techniques are also used to achieve the desired surface properties. In this thesis work gamma ray and ion irradiation techniques have been used for surface modification. The ion interaction with target materials is the key factor in ion induced modifications. If the incoming ion energy is sufficiently high, the local temperature around the ion track shall raise beyond the melting point

of the target materials. This results in modification of crystalline material into amorphous state and vice versa. Being a thermal process, by using ion irradiation, nanomaterial properties, which are difficult by other conventional methods, could be tailored. Ion implantation has become very fascinating technique for surface modification due to the high potential adoptability in wide spread areas viz., large scale integration (LSI) circuit designing [39], catalysis reactions [40] and modification of surfaces, design of quantum devices [41], light emitting devices (LED) technology [42] and bio-compatibility controllers [43] for nervous system diagnostic and nerve cell treatment.

1.3 Gamma Irradiation of Materials

Gamma (γ) irradiation of materials is the process of exposing various materials to ionizing gamma rays in a highly controlled manner for a specific goal. γ -rays are electromagnetic rays with very high frequency (ν) and short wave length (λ), placed at the extreme right of the electromagnetic spectrum. γ -rays can ionize the material placed within their range. The isotope ^{60}Co is the mostly used γ source for experiments organizing of materials through irradiation. Since the temperature of the target material does not increase considerably after γ irradiation, this process is called as also named as ‘cold process’. It is also called as ‘chemical free process’, in the sense that parameters such as humidity, temperature and pressure have no effect on the samples being irradiated with γ -rays. However, the γ -rays interact with the electrons in the solid by three mechanisms viz (i) photoelectric effect, (ii) Compton scattering and (iii) pair production. In *photoelectric effect* mechanism [44], the gamma photons are absorbed by the core electron (in the material) and gets sufficient energy to excite into conduction band. This electron while de-excites release an Auger electron or an X-rays. However, these Auger electrons possess very small energy to damage crystal structure but they do give to good attenuation of the γ -rays. In *Compton scattering* mechanism [29], due to the interaction of the gamma ray with the material, electrons are ejected due to momentum transfer (Compton effect) and the ejected electrons have energy high enough to displace lattice atoms by the same mechanisms of electron damage [45]. In *pair production* mechanism, when the γ -rays with energy greater than twice the mass energy of an electron (e) are used, an electron-positron pair is created following the law of conservation of momentum. The produced electron and positron have same energy given as $\left(\frac{E_{\gamma}-2mc^2}{2}\right)$. The produced electron energy may contribute to the lattice damage explained by an electron damage mechanisms [30]. The positron annihilates with an electron, generating more γ -rays with less energy to create any further lattice damage.

1.4 Ion Beam Technology

An ion beam is a collection of charged ions of a particular element with almost equal energies. Ion beams have wide spread applications in various fields like electronics from basic research to manufacturing industries. The main applications of ion beam technology include ion sputtering, ion etching, ion beam analysis and most notably in ion implantation in semiconductor industry. Ion beam irradiation can induce effects to modify the various materials viz., metals, polymers, insulators, biological cells etc. Ion beams are capable of modifying crystal structure in the various ways viz., creating defects such as point defects, columnar defects, interstitials and their complexes [46]. It anneals the already existing defects in the material and also produce phase transformation (phase from crystalline to amorphous or vice versa), growth of material in anisotropic way, etc. Ion beams are the powerful tool for preparation, tailoring with anticipated properties, characterization and modifications of materials as per requisite. Owing to the high flexibility and option to tune the key parameters like energy, fluence, size and point of irradiation exactly at atomic level as per required, ion beams are considered as sophisticated technology in material research especially in thin film technology. The surface and material feature modifications caused due to the energetic ion interaction with any material can be classified as: doping, ion beam synthesis, ion deposition, ion mixing, ion irradiation, ion induced adhesion etc.,

Ion implantation is a technique which enables to introduce controlled amount of almost any foreign (ion) species into surface and sub-surface region of any solid material (target). The energies used in this technique generally lies in the range 10-500 keV with a corresponding penetration depth in the range 100 Å - 1µm, depending on the choice of target material and energy of ion beam selected. In ion implantation process, the incoming ions impact on the target material with kinetic energies of 5–6 times higher than binding energy of the target atoms and results modifications in surface or sub-surface region of target material which can lead to the alloy formation. As per the principle any element of the periodic table can be converted into ions and can be injected into surface or near surface region of any kind of target material. But this process is highly depends on source and instrumentation available. The major advantages of ion beam technique among the other available surface modifications methods are: more controlled process, temperature independent and refinishing or heat treatment is not required after irradiation. This technique has showed extremely successful in semiconductor devices [47] fabrication industry.

Introduction

Ion irradiation requires more energies as compared to ion implantation. Ion irradiation using variety of species and wide range of energies, have supported applications at various interfaces, bulk and thin film surfaces, polymers, multilayers, compounds etc. This makes an effect in various new attempts for ion mixing, modifications of surface or sub-surface areas etc., phenomenon. The damage of target material by ion bombardment in ion irradiation is of great practical interest for material processing, characterization, and nuclear reactor technology. There is limited possibility to study the process inside the target material during ion irradiation. Modifying the material properties and tailoring the material structure at nano scale [48, 49] is possible by proper combination of ion beams and irradiation parameters viz., ion species, ion energy, size, fluence etc.

The ion interaction with target (any kind of solid) material is considered as non-equilibrium process. The ion-solid interactions describe the physics of energy loss of ions while slowing down in the solid [50]. The collision process between incoming ions and target atoms can be described by a complex Hamiltonian by approximating the collision as the interaction between ion and scattered particles, such as interaction between projectile (ion beam) - target (nucleus of material) and projectile-electron of the target. When an energetic ion passes through the target material, it loses its energy to the atoms and electronic system of the target material by scattering process through Coulombic interactions. This amount of energy loss governs the depth of projectile ion's penetration into target and the amount of disorder created inside the target lattice.

The energetic ion beam transfers its energy to the target atoms immediately after the interaction with target material. This energy transfer process is termed as “stopping power”, ($-dE/dx$) and described as the amount of energy lost per unit length of an ion on its trajectory inside the target. The stopping of ion inside the target material is explained by two basic energy transfer mechanism process viz., nuclear energy loss (S_n) and electronic energy loss (S_e). The nuclear energy loss is due to elastic collision, similar to ‘ballistic’ billiard ball model and account for interaction of ion with target atoms (nucleus). The electronics energy loss accounts for in energy transferred by inelastic collision between ion and electrons of the target material. The total stopping power is defined as the sum of nuclear and electronic energy transferred inside the target material. The reciprocal integral of stopping power is referred as total projectile range (R_p) of incoming ion in the target material. Both S_n and S_e increases with ion energy linearly and reach their maximum and fall down thereafter as depicted in Fig.1.1. When the S_e reaches maximum it is called ‘Bragg peak’, which has energies of orders of magnitude higher than the

Introduction

S_n . In general heavy energetic ions and light ions of any energy have stopping powers in the range $\sim \text{keV}/\text{\AA}$ and transfer more energy via electronic energy loss. Similarly low energetic heavy ions with stopping power in range $\sim \text{eV}/\text{\AA}$ transfer their energy via nuclear energy loss. In other words, in high energy ion irradiation the electronic energy loss dominates, whereas nuclear energy loss dominates in low energy irradiations. The nuclear energy loss leads to the transfer of kinetic energy of the incoming ion species to the target atoms and displace these atoms from their original positions. Similarly the electronic energy loss leads to excitation of electrons of target atoms. When the transfer of energy for primary knock on atom is adequately high, there is a possibility of higher order (secondary, tertiary, and so on) knock-ons in target.

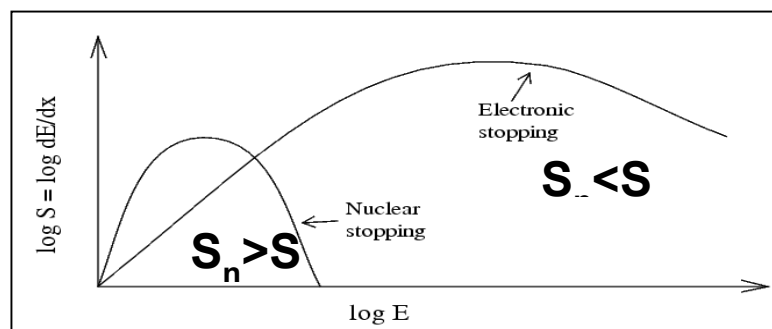


Figure 1.1 Graph for projectile ion energy versus energy loss.

The energetic ion transfers its energy to solid, while it is passing through the target material through elastic and inelastic scattering process. This results in different events, which are shown in Fig. 1.2. The energy of the incoming ion beam is being transferred to the target atoms while the passing through the target material resulting in either displacing the target atoms by elastic collisions known as nuclear stopping or exciting the target atoms by inelastic collision known as electronic stopping. If the energy loss occurs from nuclear stopping then it is known as nuclear energy loss and the energy loss is from electronic stopping is defined as electronic energy loss. One more mechanism which accounts for energy loss of ion beam is known as charge exchange process, between target atoms and incoming ion species. This can be expressed as

$$\left(\frac{dE}{dX}\right)_{loss} = \left(\frac{dE}{dX}\right)_{Elect} + \left(\frac{dE}{dX}\right)_{Nucl} + \left(\frac{dE}{dX}\right)_{Charge\ exchange}$$

where $\left(\frac{dE}{dX}\right)_{Elect}$ is from electron, $\left(\frac{dE}{dX}\right)_{Nucl}$ is from nucleus and $\left(\frac{dE}{dX}\right)_{Charge\ exchange}$ is from the charge exchange process accounts only small amount of total energy loss during ion interaction, it can be neglected.

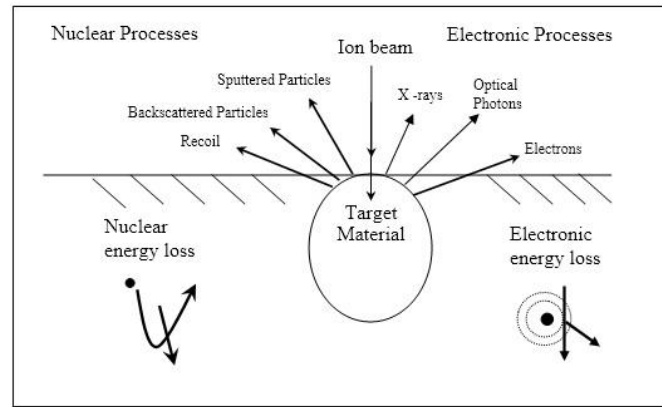


Figure 1.2 Basic ion-solid interaction process.

In general, the slowing down of ion species inside the target material (energy deposition process) is described by “stopping power” $\frac{dE}{dX}$, which can be described as amount of energy (dE) lost by an incoming ion species while traversing a distance (dx) in the target material. Therefore the stopping power can be expressed as

$$\frac{dE}{dX} = \left(\frac{dE}{dX}\right)_e + \left(\frac{dE}{dX}\right)_n \cong S_e + S_n$$

The electronic stopping power (S_e) can be classified into two regimes separated by the velocity $v_0 Z_i^{2/3}$ where v_0 is Bohr velocity. The velocity of ion (“ v_i ”) is in $0.1v_0$ to $v_0 Z_i^{2/3}$ the range. Thus S_e is proportional to v_i for $v_i > v_0 Z_i^{2/3}$. The nuclear stopping power (S_n) and electronic stopping power (S_e) are depicted in Fig. 1.1.

Nuclear energy loss (S_n) accounts for the amount of energy transferred through elastic collision between incoming ion species (projectile) and target atoms. This can be estimated by considering the screened coulomb potential and impulse approximations. The interactive potential between two atoms of atomic number Z_1 and Z_2 can be defined as $V(r) = \frac{Z_1 Z_2}{r^2} \chi\left(\frac{r}{a}\right)$. Here, ‘ χ ’ represents the screening function, ‘ a ’ represents the Thomas-Fermi screening radius and equals to $a = \frac{0.885a_0}{(Z_1^{1/2} + Z_2^{1/2})^{1/2}}$ where a_0 is the Bohr radius.

Considering the appropriate screening potential and impulse estimation, S_n is expressed as

$$S_n = -\left(\frac{dE}{dX}\right)_n = N \frac{\pi^2}{2} Z_1 Z_2 e^2 a \frac{M_1}{M_1 + M_2}$$

Electronic energy loss (S_e) occurs when an ion beam with sufficient energy is bombarded on target material, it interacts immediately with electronic system of the target atoms. In these

Introduction

interactions, electrons encounter an impulse by Coulomb force when the incoming (projectile) ion species pass from that area. When the impulse is sufficiently high, it can either excite or ionize the atoms of target material. The energy of the incoming ion beam is continuously decreased through these interactions resulting in slowing down of the ion inside the target. The expression for electronic energy loss (S_e) inside the target material is given as

$$S_e = -\left(\frac{dE}{dX}\right)_e = \frac{4\pi e^4 Z_p^2 A Z_t N_t}{m_e v^2} \times \left[\ln\left(\frac{2m_e v^2}{I}\right) - \ln\left(1 - \frac{v^2}{c^2}\right) - \frac{v^2}{c^2} \right]$$

Here ' v ' is the velocity and ' $Z_p e$ ' is the charge of projectile ions, while ' Z_t ' is the atomic number and ' N_t ' is number density of target atoms. The quantities ' m_e ' and ' e ' represents rest mass of electron and charge of electron respectively. The ' I ' is ionization potential of the target.

1.5 Problem Definition and Objectives

An important aspect which was not addressed properly in the literature was the low and high energy facing capabilities of different kind of polycrystalline diamond thin films. In the past (as discussed in the next chapter), the choice of diamond films was poor. In view of this, the best possible polycrystalline diamond films have been selected to see the variation in results, if any. In this context ion beam and gamma ray irradiations of typical diamond thin films were planned and executed. It was also planned to check any formation of phases like C-N, C \equiv N, etc., due N⁺ beam irradiation. In this study, N⁺ ions are implanted into the surface and sub-surface regions of typical polycrystalline diamond thin films, which are deposited using microwave plasma enhanced chemical vapor deposition (MWCVD) technique, which is expected to give better diamond films, phase-wise, than the hot-filament assisted chemical vapor deposition (HFCVD) under the similar input gas mixture conditions; in other words, MWCVD diamond films are better for implantation without considerable changes in diamond phase and thereby retaining mechanical stability of the films. Previously, N⁺ ion implantation in MWCVD diamond films enhanced the tribological properties while in-situ N doping was used to achieve through thickness conductivity. Simultaneously the research plan was also to prepare metal (conductive top diamond layer due to nitrogen implantation)-Insulator (diamond)-Semiconductor (Si substrate) structure using ion beam irradiation technique. This would pave a wave to novel fabrication method of MIS type structures involving diamond thin films [51] by avoiding otherwise complicated fabrication methods when diamond like material is involved. On the other hand, if diamond and diamond/ β -SiC nanocomposite thin films are to be used in the above mentioned applications, their mechanical stability (mainly surface

Introduction

hardness and adhesion to the underlying substrate) has to be ensured. It was envisaged that inclusion of β -SiC along with diamond in the film, the toughness and adhesion of the nanocomposite film would enhance [52]. In this context, critical understanding of the mechanical contact damage of the diamond/ β -SiC nanocomposite thin films was planned in this thesis work. Diamond/ β -SiC nanocomposite thin films were expected to be excellent candidates for bio-sensing applications [53]. However the I-V characteristics which are very important for developing these nanocomposite surfaces for bio-sensing have not been reported. Therefore explaining the I-V characteristics of diamond/ β -SiC nanocomposite thin films with varying β -SiC content was also taken up. With regards to g-C₃N₄, it was shown that when it is doped with Si, it shows outstanding cyclic performance as an anode material in lithium ion batteries. However, it is very difficult (multi-steps and time consuming) to incorporate Si into g-C₃N₄ surface by virtue of synthesis procedures. In this regard Si ion implantation into g-C₃N₄ was planned and executed. This is a new way to dope Si into g-C₃N₄ and this method may work in the case of other carbonaceous materials.

1.6 Overview of the Thesis

Chapter 1 discusses about the introduction of diamond, β -SiC, graphene nitride materials and importance of surface modification of these materials. Also, the introduction about irradiation techniques. In Chapter 2 literature survey of surface modified techniques for diamond and graphene nitride materials and their applications as MIS electronic devices are described. Chapter 3 discusses the detailed experimental work carried out in this thesis work. The experimental work consists of irradiation of materials and surface characterization of the materials in concerned applications. Chapter 4 covers the results and discussions of the present thesis work. Chapter 5 presents conclusions of the thesis work and future scope of research in relation to this work. All the references that have been cited in the thesis have been arranged and numbered in the order they appear in the main text under the heading 'References' at the end of each chapter.

References

- [1] "Synthetic Diamond Films: Preparation, Electrochemistry, Characterization and Applications", Ed: E. Brillas and C. A. M. Huitle, John Wiley and Sons (2010).
- [2] "Physics and Technology of Silicon Carbide Devices", Ed: Y. Hijikata, Intech Open (2012).
- [3] "Ultrananocrystalline diamond: Synthesis, properties, and applications", Ed: O. A. Shenderova, D. M. Gruen, Oxford: William Andrew (2012).

- [4] N. Yang, H. Zhuang, R. Hoffmann, W. Smirnov, J. Hees, X. Jiang, and C. E. Nebel, *Chem. Eur. J.* 18, 6514 (2012).
- [5] N. Yang, H. Zhuang, R. Hoffmann, W. Smirnov, J. Hees, X. Jiang, and C. E. Nebel, *Anal. Chem.* 83, 5827 (2011).
- [6] D. J. Martin, K. P. Qiu, S. A. Shevlin, A.D. Handoko, X. W. Chen, Z. X. Guo, and J. W. Tang, *Angew. Chem. Int. Ed.* 53, 9240 (2014).
- [7] J. Wirth, R. Neumann, M. Antonietti, and P. Saalfrank, *Phys. Chem. Chem. Phys.* 16, 15917 (2014).
- [8] K. Dai, L. Lu, C. Liang, Q. Liu, and G. Zhu, *Appl. Catal. B: Environ.* 156–157, 331 (2014).
- [9] W. C. Peng, and X. Y. Li, *Catal. Commun.* 49, 63 (2014).
- [10] Y. Li, Y. Zhao, L. Fang, R. Jin, Y. Yang, and Y. Xing, *Mater. Lett.* 126, 5 (2014).
- [11] F. Su, S. C. Mathew, G. Lipner, X. Fu, M. Antonietti, S. Blechert, and X. Wang, *J. Am. Chem. Soc.* 132, 16299 (2010).
- [12] X. D. Bai, D. Y. Zhong, G. Y. Zhang, X. C. Ma, S. Liu, E. G. Wang, Y. Chen, and D. T. Shaw, *Appl. Phys. Lett.* 79, 1552 (2001).
- [13] G. Wu, Y. Hu, Y. Liu, J. Zhao, X. Chen, V. Whoehling, C. Plesse, G. T. M. Nguyen, F. Vidal, and W. Chen, *Nat. Commun.* 6, 7258 (2015).
- [14] R. Lin, Z. Li, D. I. A. El Amaiem, B. Zhang, D. J. L. Brett, G. He, and I. P. Parkin, *J. Mat. Chem A* 5, 25545 (2017).
- [15] P. K. Chu, J. Y. Chen, L. P. Wang, and N. Huang, *Mater. Sci. Eng. Rep.* 36, 143 (2002).
- [16] B. D. Ratner, *Biosens. Bioelectron.* 10, 797 (1995).
- [17] X. S. Zhou, Z. H. Luo, P. F. Tao, B. Jin, Z. J. Wu, and Y. S. Huang, *Mater. Chem. Phys.* 143, 1462 (2014).
- [18] S. Samanta, S. Martha, and K. Parida, *Chem. Cat. Chem.* 6, 1453 (2014).
- [19] X. Bai, L. Wang, Y. Wang, W. Yao, and Y. Zhu, *Appl. Catal. B: Environ.* 152–153, 262 (2014).
- [20] L.Y. Chen, and W. D. Zhang, *Appl. Surf. Sci.* 301, 428 (2014).
- [21] S. Wang, C. Li, T. Wang, P. Zhang, A. Li, and J. Gong, *J. Mater. Chem. A* 2, 2885 (2014).
- [22] G. Koh, Y. W. Zhang, and H. Pan, *Int. J. Hydrogen Energy* 37, 4170 (2012).
- [23] S. Lu, Z. W. Chen, C. Li, H. H. Li, Y.F. Zhao, Y. Y. Gong, L. Y. Niu, X. J. Liu, T. Wang, and C. Q. Sun, *J. Mater. Chem. A* 4, 14827 (2016).
- [24] A. W. Martinez, and E. L. Chaikof, *Nanomed. Nanobiotechnol.* 3, 256 (2011).
- [25] Y. Ikada, *Biomater.* 15, 725 (1994).
- [26] D. Khang, J. Lu, C. Yao, K. M. Haberstroh and T. J. Webster, *Biomater.* 29, 970 (2008).

Introduction

- [27] A. Ranjan, and T. J. Webster, *Nanotechnol.* 20, 305102 (2009).
- [28] M. K. Kuntumalla, K. Rajamudili, N. R. Desai, and V. V. S. S. Srikanth, *Appl. Phys. Lett.* 104, 161607 (2014).
- [29] H. Lee, S. M. Dellatore, W. M. Miller, and P. B. Messersmith, *Science* 318, 426 (2007).
- [30] M. M. M. Bilek, D. V. Bax, A. Kondyurin, Y. Yin, N. J. Nosworthy, K. Fisher, A. Waterhouse, A. S. Weiss, C. G. D. Remedios, and D. R. McKenzie, *Proc. Natl. Acad. Sci.* 108, 14405 (2011).
- [31] A. Kraft, *Int. J. Electrochem. Sci.* 2, 355 (2007).
- [32] “Quantum Information Processing with Diamond”, Ed: S. Praver, I. Aharonovich, Woodhead Publishing (2014).
- [33] A. Bolker, C. Saguy, and R. Kalish, *Nanotechnol.* 25, 385702 (2014).
- [34] R. Kalish, *Nucl. Instrum. Methods Phys. Res. B* 272, 42 (2012).
- [35] S. A. Rakhaa, J. Taja, and G. Yu, *J. Exp. Nanosci.* 8, 555 (2013).
- [36] A. Kayani, E. Garratt, S. AlFaify, A. Dissanayake, G. Tecos, D. C. Mancini, and M. Syed, *AIP Conf. Proc.* 1336, 271 (2011).
- [37] Y. Watanabe, and N. Kitazawa, *New Diam. Front. C. Tec.* 15, 131 (2005).
- [38] S. Talapatra, J. Y. Cheng, N. Chakrapani, S. Trasobares, A. Cao, R. Vajtai, M. B. Huang, and P. M. Ajayan, *Nanotechnol.* 17, 305 (2006).
- [39] M. Sugitani, *Rev. Sci. Instrum.* 85, 02C315 (2014).
- [40] J. Ishikawa, H. Tsuji, and Y. Gotoh, *Surf. Coat. Technol.* 203, 2351 (2009).
- [41] L. H. Zhou, C. H. Zhang, Y.T. Yang, B. S. Li, L. Q. Zhang, Y.C. Fu, and H. H. Zhang, *Nucl. Instrum. Methods Phys. Res. B.* 267, 58 (2009).
- [42] N. A. Sobolev, *Semiconductors* 44, 1 (2010).
- [43] H. Tsuji, H. Sato, T. Baba, S. Ikemura, Y. Gotoh, and J. Ishikawa, *Nucl. Instrum. Methods Phys. Res. B* 166–167, 815 (2000).
- [44] V. A. J. Van Lint, T. M. Flanagan, R. E. Leadon, J. A. Naber, and V. C. Rogers, *Wiley IEEE Proc.* 128, 359 (1981).
- [45] B. Campbell and A. Mainwood, *Phys. Stat. Sol. (a)* 181, 99 (2000).
- [46] J. P. Singh, R. Singh, N.C. Mishra, D. Kanjilal, and V. Ganesan, *J. Appl. Phys.* 87, 2742 (2000).
- [47] S. B. Felch, M. I. Current, and M. C. Taylor, WEYB2, Proceedings of PAC 2013, CA, USA.

Introduction

- [48] S. V. Rogozhkin, A. A. Aleev, A. G. Zaluzhnyi, R. P. Kuibida, T. V. Kulevoi, A. A. Nikitin, N. N. Orlov, B. B. Chalykh, and V. B. Shishmarev, *Phys. Met. Metallogr.* 113, 200 (2012).
- [49] M. Miglierini, and M. Hasiak, *J. Nanomater.*, 2015, 175407 (2015).
- [50] I. P. Jain, and G. Agarwal, *Surf. Sci. Rep.* 66, 77 (2011).
- [53] K. Hirama, S. Miyamoto, H. Matsudaira, K. Yamada, and H. Kawarada, *Appl. Phys. Lett.*, 88, 112117 (2006).
- [52] “Deposition and Characterization of Nanocrystalline Diamond/ β -SiC Composite Film System”, V. V. S. S. Srikanth, Shaker Verlag GmbH, Aachen, Germany (2008).
- [53] H. Zhuang, B. Song, and V. V. S. S. Srikanth, X. Jiang, and H. Schonherr, *J. Phys. Chem. C*, 114, 20207 (2010).

Chapter 2 Literature Review

2.1 Gamma Rays Irradiated Diamond

Defects produced by electron, neutron, gamma and ion irradiation of diamonds have been investigated for about 100 years. Gamma radiation consists of energetic photons that are eventually absorbed as they penetrate a dense material. Even though diamond is considered as an extremely hard radiation material, the basic mechanisms underlying the lattice damage caused by high energy ions and photons (i.e., ion beam irradiation, γ rays, etc.) are not fully understood. Some models based on Monte Carlo simulations, known as TRIM were developed for predicting the damage in diamond caused by electron and γ -irradiations. The energies investigated range for electron irradiation is from 0.25 to 10 MeV and for γ -rays it is 1 to 15 MeV [1]. The γ -rays with energy below 15 MeV lack sufficient nuclear cross section for direct interaction. It is also understood that lattice disorder in diamond takes place by γ -rays in indirect way through Compton scattering. Vacancies and interstitials [2] are created in this scattering process which leads to the lattice distortion. The range (penetration depth) of γ -rays are much greater and are capable to penetrate in diamond film of thickness ~ 5 mm without affecting the lattice structure. Figure 1 shows the cross-section for gamma rays process in diamond. It shows that Compton scattering dominates in a broad range of energies. But the pair production begins to become just significant at the highest energies. Even though the photo electric effect dominates at energies below 100 keV, the electrons produced do not contribute significant damage to the crystal.

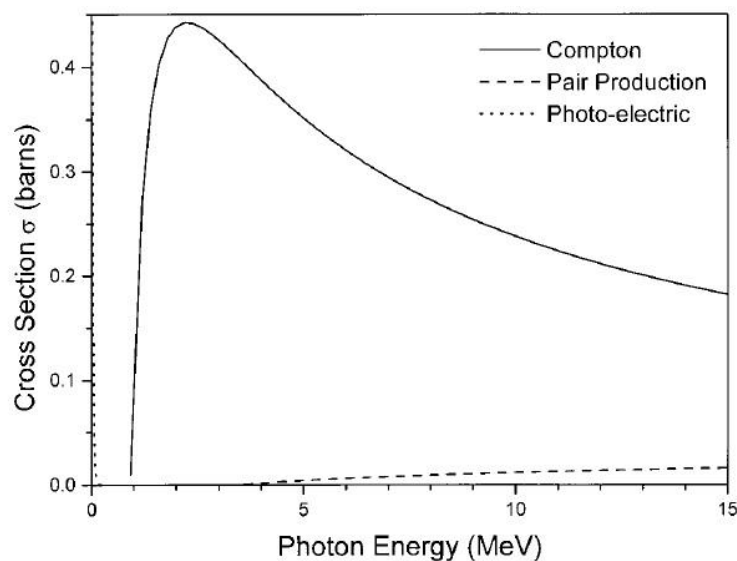


Figure 2.1 Cross-section processes for gamma ray interaction with diamond [1].

Diamond has excellent intrinsic properties such as mechanical, electrical, chemical, optical, and biocompatibility [3, 4]. These properties make the diamond, a good candidate for bioelectronics applications [5-10]. The high radiation hardness of diamond is accepted as a most appropriate material for using in radiation therapy [7-14] such as oncology and radiology. Synthetic CVD diamond, being non-toxic and tissue supportive, has been proposed for radiation dosimetry [15-20] and radiotherapy applications [11-14, 21-22]. Diamond based radiation detectors are being used in clinics for many years [23-27]. CVD diamond films are highly potential for radiation dosimetry [28-32]. The electrical resistance of diamond varies inversely with absorbed dose in radiation detectors [33]. Diamond is also used as a detector material in harsh environments [34-36]. It is a promising material for X-ray, γ -ray, and charged particles' detection. This is owing to the unique properties of diamond such as, high resistance to radiation conditions and good number of charge carriers with high mobility. Basically the fission chambers are radiation resistant and the coating materials used in this should possess high radiation facing capability. So, the detectors coated with diamond are only used in radiation hardness testing. During the operation of ITER reactor, plasma provides large quantities of neutron and gamma flux with huge amount of energy. This radiated flux creates damage and activation effects on plasma as well as numerous detectors modules. In order to establish a good material for the radiation hardness and extremely withstanding with gamma radiation, single crystal diamond detectors are examined. These gamma radiation tests are performed in dark environment and ambient temperature with varying absorbed dose [37], which are essential to ITER Radial Neutron Camera (RNC) [38]. This test showed huge damage to diamond contacts and contact destruction at 1MGy and 4.7 MGy [37], respectively. The HPHT diamonds are tested in radiation detecting devices [39] and their current response was different when they are exposed to gamma irradiation [39]. The effect of structural transformation on MWCVD microcrystalline diamond [40-42] films through γ -irradiation in their electron field emission (EFE) properties are reported [43]. The effects of γ -radiation on structural modifications of diamond thin films are reported [44]. Nanocrystalline diamond films become more resilient in radiation studies due to the phase transformation from sp^3 to sp^2 . The electron field emission has been improved in both kind of films after γ irradiation. Diamond films are tested up to the dose of 150 kGy and 4.4×10^{13} neutrons/cm² with X-rays and neutron radiation, respectively without any electronic or structural changes [45]. However, it must be noted that the diamond thin films reported in the literature are not apt w.r.t their microstructure, phase information and crystallinity. Over the years CVD diamond processes have evolved and as a consequence far better diamond thin films are being produced. Therefore

these films are expected to show different behavior to γ -ray irradiation.

2.2 Ion Irradiated Diamond

The probing of ion beam (projectile) into the target material (here diamond and graphene nitride) acts as a valuable tool for tailoring the material properties viz., structural, chemical, transport (electrical), magnetic etc., in controlled fashion. Metals are made as corrosive resistance by irradiating with high energy ion beams. For example, irradiation with N^+ ions forms high resistive nitride layers on the surface, which withstand tribological load much longer [46]. Ion irradiation phase change effects on carbon allotropes such as diamond and fullerite are important for better technological applications. These materials produce sp^2 rich phase, non-graphitic phase after the irradiation which can be used to construct electronic displays (field emission displays), FETs, electronic devices such as tunable electronically anisotropic material on semiconductors (TEAMS) [47]. The bonding inter-conversions from sp^3 to sp^2 and vice versa is most noticeable phenomena in carbon materials which occurs during the irradiation process. The exceptional properties of diamond including, high hardness, large band gap, abundant ingredient element, chemical stability, bio-congenial etc., make diamond thin films (hetero and homo epitaxial) are good candidates for technological applications such as mechanical tools, biomedical and optoelectronic devices. In particular, the high hardness to radiation environment of diamond is becoming more useful in designing particle detectors, nuclear radiation batteries, dosimeters, nuclear micro battery, space equipment and other devices which are operated at harsh radiation environments [48-50].

Ion irradiation of diamond modifies its lattice, and thereby its optical, thermal, mechanical, electronic and transport properties are expected to be modified. Diamond is often considered as an insulator with high resistivity (ρ) $\sim 10^{16}$ Ω cm and a wide band gap (5.47 eV). The resistivity of diamonds can be lowered by introducing dopants. Diamond is not easy to dope since it is difficult to get non-carbon atoms to occupy substitutional sites within the dense crystal lattice. In ion irradiation process, the energy of the incoming ion beam is transferred to the target atoms and as a consequence the ion is slowed down inside the target material. The effects of ion irradiation on the target material can be modified by controlling the ion dose and energy as per desired. As observed in many covalently bonded materials, high intense ion irradiation breaks the bond and leads to amorphization. But in case of diamond irradiated with ion beam, the broken bonds rearrange themselves to form more stable sp^2 structure. The effects of ion implantation of diamond like carbon (DLC) films, carbon fibers and CVD diamond thin

films are investigated by various groups [51,52]. It was found that irradiation leads to phase modification by reducing sp^3 phase and increasing sp^2 phase in diamond films. Most of the ion irradiation studies on diamond films are focused on effects on chemical bonding (sp^3 to sp^2 or sp^2 to sp^3) of carbon, conductivity, surface morphology and very few investigations are there in field emission effects. Ion implantation in diamond creates defect states which act as donors. Hence n-type conductivity can be introduced in diamond by surface modification of the diamond by ion implantation. In spite of that, the tendency of sp^3 bonds of diamond to change to sp^2 by ion implantation and hence to form graphitic bonds which effects the electrical properties due to doping. Large decrease in resistivity of ion irradiated diamonds are due to the formation of highly conductive graphitic islands. The hopping conductivity between these islands are responsible for low resistivities which are measured in ion implanted diamond.

The microwave plasma assisted CVD technique is used to grow diamond thin films [51-52] and their morphology, microstructure and physical properties are reported after B doping of these films [53, 54]. Diamond is a large band gap material and is not suitable for electrode applications. However, similar to other wide band gap materials like AlN, SiC etc., there is a possibility to improve the conductive properties of diamond by doping with suitable dopants. Boron and nitrogen are the widely demonstrated dopant species, forming acceptor and donor states respectively, but both require high levels of thermal activation to release free carriers (0.37 and 1.7 eV). Most widely, boron is used as dopant to produce conducting diamond electrode [55] due to its less activation energy (0.37 eV) [53] and is used in sensor applications [56-65]. Diamond doped with boron acts as a p-type semiconductor. Similarly doping with phosphorus [66], sulfur [67, 68] and nitrogen results in n-type conductivity in diamond. The charge carrier activation energy for phosphorus and nitrogen are 0.6 eV [65] and 1.7 eV [65, 69-70], respectively. The conductivity of diamond electrodes depend on both nature and amount of dopants. For example the resistivity (ρ) in B doped diamond varies from 5 to 100 $m\Omega$ cm [53, 71]. Typical boron concentration in doped diamond is between 10^{19} - 10^{21} atoms/cm³ [68].

Owing to exceptional electrochemical properties, diamond electrodes doped with suitable dopants, find various applications. The possibility for modifications of conducting diamond thin films is with metal ion implantation [72-74]. The implanted diamond electrodes also have good electroanalytical applications [75-76]. Diamond electrodes implanted with Ni and Cu are used to detect glucose content in amperometric measurements [69] and Pt doped electrodes used for H₂O₂ analysis [70]. Similarly Ir implanted electrode is used for As(III) deduction [71].

Ultra-nanocrystalline diamond (UNCD) films grown by microwave plasma enhanced chemical vapor deposition (MPCVD) technique are found to be prominent for nano electronic device uses [77, 78] after doping them with the nitrogen. The conductivity of these diamond films can be modified by varying doping concentration of nitrogen [79] which is different from conventional semiconductors. Some reports of UNCD films grown through MPCVD technique showed the metallic behavior and negative magneto-resistance (MR) features [74-75, 80] after the heavy nitrogen doping.

A great interest is paid on synthesis and understanding the effects of surface and structural studies of nitrogen doped CVD nano-diamond films. The nanocrystalline diamond films have small grains and tight grain boundaries leading to improvement in the performance of devices. The density of localized states in nano-diamond thin films can be increased by addition of amorphous carbon, which further leads to dominant hopping processes [81]. This indicates the significance of sp^2 phases in grain boundaries (GB) [78]. The NCD films grown by hot filament chemical vapor deposition (HFCVD) technique [82-83], exhibit high activated conduction over wide temperatures range. The transport (conduction) studies in diamond films place a foundation for novel fast switching devices [80].

2.3 Graphene Nitride

Carbon nitride (CN_x) materials have lot of potential as hard coatings [84], electronic materials [85], lithium intercalation electrodes [86], catalyst supports [87], and gas separation systems [88]. Graphitic carbon nitride (g- C_3N_4) is considered as an attractive polymeric organic semiconductor and has been extensively studied owing to its special optical and electronic behaviors [89-92]. In recent years different possible techniques have been used to improve the photo-catalysis ability and surface modifications of g- C_3N_4 . For example, by doping metal and non-metals [93-95] in to g- C_3N_4 . The 2D single layered g- C_3N_4 structure exhibits large specific surface area which offers more active sites for better electronic and optical properties than in its bulk form [96]. The large specific surface area is an important parameter for high mass transfer process and prevention of the photo-generated carriers' combination in g- C_3N_4 . Doping is an effective tool for modifying the structure, surface, phase, electronic and magnetic properties of materials. Doping with suitable elements supports either formation of new chemical bonds or relaxing the nearby chemical bonds in vicinity of dopants. Remarkable results of improved g- C_3N_4 properties by various dopants are reported in literature and few of them are listed here; ultrathin g- C_3N_4 nanosheets improve the quantum yield of photo

luminesces [97] and photo-absorption, and Li doped g-C₃N₄ monolayer improves light absorption performance [98]. Similarly oxygen doped g-C₃N₄ exhibits superior photo reactivity [99] and also enhances the mobility of carriers and reduces the combination of electron-hole pairs which are photo-generated [100]. Carbon materials doped with Si are known as friction coefficient reduction materials in moist atmosphere [101]. The Si doped carbon materials find applications in oxidation resistance at higher temperatures [102] and are used in gas sensing technology [103-104]. Some previous reports suggested that the visible light absorption coefficient of g-C₃N₄ [105] can be improved by doping with non-metals. In spite of realizing the various optical and electronic behavior of 2D g-C₃N₄ thin films doped with various elements, the real mechanism underlying the chemical bond formation and/or bond relaxation in the vicinity of dopant is not yet fully understood. This is very crucial to modify the surface, phase, optical, structural, catalytic, electronic and magnetic properties of g-C₃N₄ material, because the optical and electronic properties can be modified by chemical bond relaxation [102, 106]. Hence it has great importance to know the fundamental mechanism of doping with non-metal viz., H, B, C, O, F, Si etc., atoms in g-C₃N₄ to tailor the optical, surface, structural, phase and electronic properties of g-C₃N₄. It is very difficult to obtain Si doped g-C₃N₄ by virtue of its synthesis procedures. Several techniques are proposed to obtain Si doped g-C₃N₄ viz., magnetron sputtering (DC & AC), RF Plasma enhanced CVD, hot filament plasma enhanced CVD and pyrolysis etc., [92-107]. These doping techniques are not selective and controllable in comparison to ion beam technique.

2.4 Metal-Insulator-Semiconductor Devices

Carbon materials are attractive (for MIS devices) due to their high reliable properties such as thermal conductivity, chemical rigidity, mechanical strength and resistance to harsh radiation environments, [108,109] etc., Diamond films are exploited as dielectric materials in Metal-Oxide-Semiconductor devices [110]. Similarly diamond is used as a conductivity layer (p-type) in SiC detectors [111] and to protect the device reliability after the irradiation. Diamond is used in monitoring the radiation beams. Biosensors made with diamond thin films are great helpful for real-time monitoring during the biochemical reactions. The effect of gamma radiation (up to 300 Gy) on function and stability of hydrogen-terminated diamond solution-gated field effect transistors are investigated [112]. The enhancement in Total Ionizing Dose effects (TID) [113] on field effect transistors e.g., MOSFET is a substantial interest of concern for an aerospace industry. This enables the preparation of low cost and less memory consuming Complementary Metal Oxide Semiconductor (CMOS) integrated circuits for device

applications in hard radiation environment [114-116]. Recently, a new layout design based on ‘interface engineering’ has been introduced. This design involves the modification of regions between drain and channel and channel and source of MOSFET. In other words this design can be considered as change in the layout of gate in MOSFET by employing the non-standard geometries. Based on the above explanation, diamond MOSFET [117-121] can be examined as an effective less cost device for CMOS ICs in space applications [109, 110].

References

- [1] B. Campbell and A. Mainwood, *Phys. Stat. Sol. (a)* 181, 99 (2000).
- [2] “Mechanisms of Radiation effects in Electronic Materials”, V. A. J. Van Lint, Wiley, New York (1980).
- [3] M. G. Donato, G. Faggio, G. Messina, S. Santangelo, M. Marinelli, E. Milani, G. Pucella, and G. Verona-Rinati, *Diam. Relat. Mater.* 13, 923 (2004).
- [4] L. Bacakova, I. Kopova, L. Stankova, J. Liskova, J. Vacik, V. Lavrentiev, A. Kromka, S. Potocky, and D. Stranska, *Phys. Stat. Sol. (a)* 211, 2688 (2014).
- [5] C. E. Nebel, B. Rezek, D. Shin, H. Uetsuka, and N. Yang, *J. Phys. D: Appl. Phys.* 40, 6443 (2007).
- [6] J. A. Carlisle, *Nat. Mater.* 3, 668 (2004).
- [7] M. Dankerl, S. Eick, B. Hofmann, M. Hauf, S. Ingebrandt, A. Offenhäusser, M. Stutzmann, and J. A. Garrido, *Adv. Funct. Mater.* 19, 2915 (2009).
- [8] B. Rezek, M. Krátká, A. Kromka, and M. Kalbacova, *Biosens. Bioelectron.* 26, 1307 (2010).
- [9] T. Ižák, K. Novotná, I. Kopová, L. Bačáková, B. Rezek, and A. Kromka, *Phys. Status Solidi B* 250, 2741 (2013).
- [10] O. Babchenko, A. Kromka, J.P. Conde, V. Chu, T. Schmiedinger, and B. Rezek, *Phys. Stat. Sol. (b)* 251, 2593 (2014).
- [11] A. Piermattei, L. Azario, A. Fidanzio, and G. Arcovito, *Phys. Med.* 14, 9 (1998).
- [12] S. Ramkumar, C. M. Buttar, J. Conway, A. J. Whitehead, R. S. Sussman, G. Hill, and S. Walker, *Nucl. Instrum. Methods Phys. Res. A* 460, 401 (2001).
- [13] A. Fidanzio, L. Azario, C. Venanzi, F. Pinzari, and A. Piermattei, *Nucl. Instrum. Methods Phys. Res. A* 479, 661 (2002).
- [14] P. Bergonzo, D. Tromson, and C. Mer, *Semicond. Sci. Technol.* 18, S105 (2003).
- [15] B. Planskoy, *Phys. Med. Biol.* 25, 519 (1980).
- [16] E. A. Burgermeister, *Phys. Med. Biol.* 26, 269 (1981).

- [17] S. Varnitsky and H. Jarvinen, *Phys. Med. Biol.* 32, 173 (1993).
- [18] P. W. Hoban, M. Heydariyan, W. A. Beckam, and A. H. Beddoe, *Phys. Med. Biol.* 39, 1219 (1994).
- [19] R. J. Keddy, T. L. Nam, and R. C. Burns, *Phys. Med. Biol.* 32, 751 (1987).
- [20] E. A. Burgemeister, *Physica*, 111B, 319 (1981).
- [21] M. Bruzzi, M. Bucciolini, G. A. P. Cirrone, G. Cuttone, A. Guasti, S. Mazzocchi, S. Pirollo, M. G. Sabini, and S. Sciortino, *IEEE Trans. Nucl. Sci.* 47, 1430 (2000).
- [22] M. Bruzzi, M. Bucciolini, G.A.P. Cirrone, G. Cuttone, S. Mazzocchi, S. Pirollo, and S. Sciortino, *Nucl. Instrum. Meth.* 454, 142 (2000).
- [23] C. DeAngelis, M. Bucciolini, M. Casati, I. Lovik, M. Bruzzi, S. Lagomarsino, S. Sciortino, and S. Onori, *Radiat. Prot. Dosim.* 120, 38 (2006).
- [24] A. J. Whitehead, R. Airey, C.M. Buttar, J. Conway, G. Hill, S. Ramkumar, G. A. Scarsbrook, R. S. Sussmann, and S. Walker, *Nucl. Instrum. Methods. Phys. Res. A* 460, 20 (2001).
- [25] G. A. P. Cirrone, G. Cuttone, L. Raffaele, M. G. Sabini, C. de Angelis, S. Onori, M. Pacilio, M. Bucciolini, M. Bruzzi, and S. Sciortino, *Nucl. Phys. B* 125, 179 (2003).
- [26] B. Marczewska, P. Olko, M. Nesladek, M. P. R. Waligorski, and Y. Kerremans, *Rad. Prot. Dosim.* 101, 485 (2002).
- [27] M. J. Guerrero, D. Tromson, C. Descamps and P. Bergonzo, *Diam. Relat. Mater.* 15, 811 (2006).
- [28] G. A. P. Cirrone, G. Cuttone, S. Lo Nigro, V. Mongelli, L. Raffaele, and M. G. Sabini, *Nucl. Phys. B* 150, 330 (2006).
- [29] M. Bucciolini, E. Borchini, M. Bruzzi, M. Casati, P. Cirrone, G. Cuttone, C. de Angelis, I. Lovik, S. Onori, L. Raffaele, and S. Sciortino, *Nucl. Instrum. Methods A* 552, 189 (2005).
- [30] A. Fidanzio, L. Azario, P. Viola, P. Ascarelli, E. Cappelli, G. Conte, and A. Piermattei, *Nucl. Instrum. Methods A* 524, 115 (2004).
- [31] C. Manfredotti, *Diam. Relat. Mater.* 14, 531 (2005)
- [32] A. Balducci, Y. Garino, A. Lo Giudice, C. Manfredotti, Marco Marinelli, G. Pucella, and G. Verona-Rinati, *Diam. Relat. Mater.* 15, 797 (2006)
- [33] E.A. Burgemeister, *Phys. Med. Biol.* 26, 269 (1981).
- [34] B. Campbell, and A. Mainwood, *Phys. Stat. Sol. (a)* 181, 99 (2000).
- [35] C. D. Clark, and E. W. J. Mitchell, *Radiat. Eff.* 9, 219 (1971).
- [36] M. Kitajima, K. Nakamura, M. Fujitsuka, H. Shinno, T. Tanabe, and M. Yumoto, *J. Nucl. Mater.* 180, 179 (1991); J. Wei and J. Ahn, *Cryst. Res. Technol.* 34, 133 (1999).

- [37] S. Baccaro et al., Radiation damage tests on diamond and scintillation detector components for the ITER Radial Neutron Camera. Poster n. P2-36, SCINT 2017.
- [38] D. Marocco et al., System Level Design and Performances of the ITER Radial Neutron Camera, FIP/P4-16, Proceedings of 26th IAEA FEC 2016.
- [39] F. Schirru, I. Kupriyanov, B. Marczewska, and T. Nowak, *Phys. Stat. Sol. (a)* 205, 2216 (2008).
- [40] K. Okano, S. Koizumi, S. Ravi, P. Silva, and G. A. J. Amaratunga, *Nature* 381, 140 (1996).
- [41] W. Zhu, G. P. Kochanski, S. Jin, and L. Seibles, *J. Appl. Phys.* 78, 2707 (1995).
- [42] C. Wang, A. Garcia, D. C. Ingram, and M. E. Kordesh, *Electron. Lett.* 27, 1459 (1991).
- [43] S. Gupta, B. L. Weiss, B. R. Weiner, L. Pilione, A. Badzian, and G. Morell, *J. Appl. Phys.* 92 (2002) 3311.
- [44] S. Gupta, M. Muralikiran, J. Farmer, L. R. Cao and R. G. Downing, *J. Mater. Res.* 24, 1498 (2009).
- [45] K. Subramanian, W.P. Kang, J.L. Davidson, N. Ghosh, and K.F. Galloway, *Microelectron. Eng.* 88, 2924 (2011).
- [46] H. Kakiuchi, T. Kobayashi, and T. Terai, *Nucl. Instr. and Meth. B* 166, 415 (2000).
- [47] D. Fink and L. T. Chadderton, *Braz. J. Phys.* 35 (3B), 735 (2005).
- [48] C. J. Eiting, V. Krishnamoorthy, S. Rodgers, T. George, J. D. Robertson, and J. Brockman, *Appl. Phys. Lett.* 88, 064101 (2006).
- [49] W. Adam et. Al, *Nucl. Instrum. Methods Phys. Res. A* 434, 131 (1999).
- [50] R. J. Tapper, *Rep. Prog. Phys.* 63, 1273 (2000).
- [51] H. Kakiuchi, T. Kobayashi, and T. Terai, *Nucl. Instr. and Meth. B* 166, 415 (2000).
- [52] J. Wang, W. Z. Li, and H. D. Li, *J. Mater. Sci. Lett.* 18, 1481 (1999).
- [53] S. Gupta, J. Farmer, D. Daghero, and R. Gonnelli, *J. Mater. Res.* 25, 444 (2010)
- [54] S. Gupta, M. Muralikiran, J. Farmer, L. R. Cao, and R. G. Downing, *J. Mater. Res.* 24, 1498 (2009).
- [55] W. Haenni, P. Rychen, M. Fryda, and C. Comninellis, "Thin-Film Diamond Part B", Ed. C. Nebel, Academic Press, Semiconductors and Semimetals Series, Elsevier, 2004, p. 149.
- [56] S. Pysarevska, L. Dubenska, S. Plotycya, and L. Svorc, *Sensors and Actuators B* 270, 9 (2018).
- [57] L. Svorc, K. Borovska, K. Cinkova, D. M. Stankovic, and A. Plankova, *Electrochim. Acta* 251, 621 (2017).
- [58] R.T. S. Oliveira, G. R. Salazar-Banda, V. S. Ferreira, S.C. Oliveira, and L. A. Avaca, *Electroanalysis* 19, 1189 (2007).

- [59] J. Scremin, and E.R. Sartori, *Can. J. Chem.*, 96, 1 (2018).
- [60] N. Alpar, P. T. Pinar, Y. Yardim, and Z. Şentürk, *Electroanalysis* 29, 1691 (2017).
- [61] R.F. Brocenschi, T.A. Silva, B.C. Lourencao, O. Fatibello-Filho, and R.C. Rocha-Filho, *Electrochim. Acta* 243, 374 (2017).
- [62] H. S. Ali, A. A. Abdullah, P. T. Pinar, Y. Yardim, and Z. Şentürk, *Talanta* 170, 384 (2017).
- [63] E. H. Duarte, J. Casarin, E. R. Sartori, and C. R. T. Tarley, *Sens. Actuators B* 255, 166 (2018).
- [64] K. Peckova, J. Musilova, and J. Barek, *Crit. Rev. Anal. Chem.* 39, 148 (2009).
- [65] J. Svítková, T. Ignat, Ľ. Švorc, J. Labuda, and J. Barek, *Crit. Rev. Anal. Chem.* 46, 248 (2016).
- [66] M. Nesladek, *Semicond. Sci. Technol.* 20, R19 (2005).
- [67] S. C. Eaton, A. B. Anderson, J. C. Angus, Y. E. Evstefeeva, and Y. V. Pleskov, *Electrochem. Solid State Lett.* 5, G65 (2002).
- [68] S. Vaddiraju, S. Eaton-Magana, J. A. Chaney, and M. K. Sunkara, *Electrochem. Solid-State Lett.* 7, G331 (2004).
- [69] J. Svítková, T. Ignat, Ľ. Švorc, J. Labuda, and J. Barek, *Crit. Rev. Anal. Chem.* 46, 248 (2016).
- [70] Q. Chen, D. M. Gruen, A. R. Krauss, T. D. Corrigan, M. Witek and G. M. Swain, *J. Electrochem. Soc.* 148, E44 (2001).
- [71] M. Fryda, T. Matthee, S. Mulcahy, A. Hampel, L. Schäfer and I. Tröster, *Diam. Relat. Mater.* 12, 1950 (2003).
- [72] T. A. Ivandini, R. Sato, Y. Makide, A. Fujishima, and Y. Einaga, *Diam. Relat. Mater.* 13, 2003 (2004).
- [73] T. A. Ivandini, R. Sato, Y. Makide, A. Fujishima, and Y. Einaga, *Diam. Relat. Mater.* 14, 2133 (2005).
- [74] T.A. Ivandini, R. Sato, Y. Makide, A. Fujishima and Y. Einaga, *Anal. Chem.* 78, 6291 (2006).
- [75] R. G. Compton, J. S. Foord, and F. Marken, *Electroanal.* 15, 1349 (2003).
- [76] O. Chailapakul, W. Siangproh, and D.A. Tryk, *Sensor Lett.* 4, 99 (2006).
- [77] O. A. Williams, M. Nesladek, M. Daenen, S. Michaelson, A. Hoffman, E. Osawa, and K. Haenen, R. B. Jackman, *Diam. Relat. Mater.* 17, 1080 (2008).
- [78] J. J. Mares, M. Nesladek M, P. Hubik, D. Kindl, and J. Kristofik, *Diam. Relat. Mater.* 16, 1 (2007).

- [79] S. Bhattacharyya, O. Auciello, J. Birrell, J. A. Carlisle, L. A. Curtiss, A. N. Goyette, D. M. Gruen, A. R. Krauss, J. Schueter, A. Sumant, and P. Zapol, *Appl. Phys. Lett.* 79, 1441 (2001).
- [80] T. C. Choy, A. M. Stoneham, M. Ortuno, and A. M. Somoza, *Appl. Phys. Lett.* 92, 012120 (2008).
- [81] P. Zapol, M. Sternberg, L. A. Curtiss, T. Frauenheim, and D. M. Gruen, *Phys. Rev. B* 65, 045403 (2001).
- [82] P. W. May and Y. A. Mankelevich, *J. Appl. Phys.* 101, 053115 (2007).
- [83] G. Chimowa, D. Churochkin and S. Bhattacharyya, *EPL*, 99, 27004 (2012).
- [84] D. M. Teter, *MRS Bull.* 23, 22 (1998)
- [85] R. Yakimova, E. Janzen, *Diam. Relat. Mater.* 9, 432 (2000)
- [86] M. Winter, J. O. Besenhard, M. E. Spahr, and P. Novak, *Adv. Mater.* 10, 725 (1998).
- [87] C. Park, and T. K. Baker, *J. Phys. Chem B.* 102, 5168 (1998).
- [88] "Advances in Chemistry Series", Eds. L. V. Interrante, L. A. Caspar, and A. B. Ellis, American Chemical Society, Washington DC, (1995).
- [89] A.H. Reshak, S.A. Khan, and S. Auluck, *RSC Adv.* 4, 6957 (2014).
- [90] A. Thomas, A. Fischer, F. Goettmann, M. Antonietti, J. O. M. Üller, R. Schlögl, and J. M. Carlsson, *J. Mater. Chem.* 18, 4893 (2008).
- [91] X. Wang, K. Maeda, A. Thomas, K. Takanabe, G. Xin, J.M. Carlsson, K. Domen, and M. Antonietti, *Nat. Mater.* 8, 76 (2009).
- [92] G. Liu, P. Niu, C. H. Sun, S. C. Smith, Z. G. Chen, G. Q. Lu, and H. M. Cheng, *J. Am. Chem. Soc.* 130, 7176 (2010).
- [93] S. Z. Hu, L. Ma, J. G. You, F. Y. Li, Z. P. Fan, G. Lu, D. Liu, and J. Z. Gui, *Appl. Surf. Sci.* 311, 164 (2014).
- [94] D. Ghosh, G. Periyasamy, and S. K. Pati, *J. Phys. Chem. C* 118, 15487 (2014).
- [95] Q. Y. Lin, L. Li, S. J. Liang, M. H. Liu, J. H. Bi, and L. Wu, *Appl. Catal. B: Environ.* 163, 135 (2015).
- [96] X. Zhang, X. Xie, H. Wang, J. Zhang, B. Pan, and Y. Xie, *J. Am. Chem. Soc.* 135, 18 (2013).
- [97] L.W. Ruan, G. S. Xu, L. Gu, C. Li, Y. J. Zhu, and Y. X. Lu, *Mater. Res. Bull.* 66, 156 (2015).
- [98] J. Li, B. Shen, Z. Hong, B. Lin, B. Gao, and Y. Chen, *Chem. Commun.* 48, 12017 (2012).
- [99] J. Cui, S. Liang, X. Wang, and J. Zhang, *Mater. Chem. Phys.* 161, 194 (2015).
- [100] X. Ma, Y. Lv, J. Xu, Y. Liu, R. Zhang, and Y. Zhu, *J. Phys. Chem. C* 116, 23485 (2012).

- [101] C. Fernández-Ramos, J. C. Sánchez-López, M. Belin, C. Donnet, L. Ponsonnet, and A. Fernández, *Diam. Relat. Mater.* 11, 169 (2002).
- [102] R. Riedel, H. J. Kleebe, H. Schonfelder, and F. Aldinger, *Nature* 374, 526 (1995).
- [103] Y. Chen, B. Gao, J. X. Zhao, Q.-H. Cai, and H. G. Fu, *J. Mol. Model.* 18, 2043 (2012).
- [104] P. A. Gowri Sankar and K. Udhayakumar, *J. Nanomater.* 2013, 293936 (2013).
- [105] C. Li, Y. F. Zhao, Y. Y. Gong, T. Wang, and C. Q. Sun, *Phys. Chem. Chem. Phys.* 16, 21446 (2014).
- [106] S. Lu, C. Li, Y. F. Zhao, Y. Y. Gong, L.Y. Niu, and X. J. Liu, *Appl. Surf. Sci.* 384, 360 (2016).
- [107] C. F. Ramos, J. C. S. Lopez, M. Belin, C. Donnet, L. Ponsonnet, and A. Fernandez, *Diam. Relat. Mater.* 11, 169 (2002).
- [108] *Diamond: Electronic Properties and Applications*, edited by L. S. Pan and D. R. Kania (Kluwer Academic, Boston, 1995). {I have to check this}
- [109] S. Gupta, R. S. Katiyar, D. R. Gilbert, R. K. Singh, and G. Morell, *J. Appl. Phys.* 88, 5695 (2000).
- [110] D. M. Fleetwood, *Microelectron. Reliab.* 42, 523 (2002).
- [111] M. Bruzzi, M. Bucciolini, F. Nava, S. Pini, and S. Russo, *Nucl. Instrum. Methods Phys. Res. Sect. A* 485, 172 (2002).
- [112] M. Kratka, O. Babchenko, E. Ukraintsev, J. Vachelova, M. Davidkova, M. Vandrovцова, A. Kromka and B. Rezek, *Diam. Relat. Mater.* 63, 186 (2016).
- [113] L. E. Seixas, O. L. Goncalvez, R. Souza, S. Finco, R. G. Vaz, G. A. da Silva and S. P. Gimenez, *IEEE Trans. Device Mater. Reliab.* 17, 593 (2017).
- [114] H. Barnaby, *IEEE Trans. Nuclear Science*, 53, 3103 (2006).
- [115] T. R. Oldham, and F. B. Mclean, *IEEE Trans. Nucl. Sci.* 50, 483 (2003).
- [116] R. C. Laco, *IEEE Trans. Nucl. Sci.* 55, 1903 (2008).
- [117] S. P. Gimenez, E. Davini, V. V. Peruzzi, C. Renaux, and D. Flandre, *Electron. Lett.* 50, 1618 (2014).
- [118] S. P. Gimenez, E. H. S. Galembeck, C. Renaux, and D. Flandre, *Microelectron. Reliab.* 55, 783 (2015).
- [119] S. P. Gimenez, *Solid-State Electron.* 54, 1690 (2010).
- [120] S. P. Gimenez, R. D. Leoni, C. Renaux, and D. Flandre, *Electron. Lett.* 50, 398 (2014).
- [121] L. E. Seixas, S. Finco, M. A. G. Silveira, N. H. Medina, and S. P. Gimenez, *Mater. Res. Exp.* 4, 015901 (2017).

Chapter 3 Experimental Work

3.1 Synthesis of Materials

3.1.1 Synthesis of diamond and diamond/ β -SiC composite thin films

The diamond and diamond/ β -SiC nanocomposite thin films used in this work were deposited by utilizing microwave plasma enhanced chemical vapor deposition (MWCVD) technique. The films were deposited using ASTeX 1500W S-1500i model 2.45 GHz MWCVD reactor by varying MWCVD parameters namely total reaction gas pressure, reaction gas composition, substrate temperature and microwave power. With regards to diamond thin films, typical polycrystalline diamond thin films were deposited for this work. With regards to diamond/ β -SiC composite thin films, β -SiC content in the films was systematically varied. All the considered diamond thin films were deposited on one-side mirror polished (100) single crystal Silicon (Si) substrates. The deposited diamond thin films are designated as NCD1, NCD2, and NCD3. The experimental conditions are tabulated in Table 3.1. In the case of NCD1 and NCD2, before their deposition, manually diamond pre-treatment substrate's surface was carried out. In this manual treatment a small amount of synthetic polycrystalline diamond paste ($\sim 1 \mu\text{m}$) was applied on to the substrate's surface and then scratched against a quartz plate. After scratching, ultrasonic cleaning was carried out first with acetone followed by ethanol and then dried in air at room temperature. In the case of NCD3, bias enhanced nucleation was carried out for 10 min before the thin film deposition by applying a negative bias voltage of -200 V to the substrate. In all the cases of diamond thin films, microwave power of 700 W was used.

Table 3.1 Experimental conditions used to deposit different diamond thin films.

| Name of thin film | Deposition Parameters | Parameter Value |
|-------------------|-------------------------------------|---|
| NCD1 | % CH ₄ in H ₂ | <1% |
| | Substrate Temperature (°C) | 600 |
| | Deposition Time (h) | 6 |
| NCD2 | % CH ₄ in H ₂ | <1% |
| | Substrate Temperature (°C) | 700 |
| | Deposition Time (h) | 6 |
| NCD3 | % CH ₄ in H ₂ | 4% during nucleation and <1% during growth |
| | Substrate Temperature (°C) | 850 |
| | Deposition Time (h) | 3 |

Experimental Work

Diamond/ β -SiC nanocomposite thin films were deposited on one-side mirror polished (100) single crystal Si substrates. The deposited diamond/ β -SiC nanocomposite thin films are designated as NCDS1, NCDS2, and NCDS3. In all the cases, bias enhanced nucleation was carried out for 10 min before the thin film deposition by applying a negative bias voltage of -150 V to the Si substrate. NCDS2 and NCDS3 are deposited using gas mixtures of H₂, CH₄, and tetramethylsilane (TMS). It may be noted that NCDS1 is a diamond film i.e., it is deposited without the use of TMS. In NCDS1, NCDS2, and NCDS3 thin film depositions, the gas mixtures used had less than 1% CH₄ in H₂, reaction gas pressure was 25 Torr, and microwave power was 700 W. TMS gas is used to co-deposit β -SiC phase along with the diamond phase. The TMS gas used in this work is 1% in H₂ and therefore the exact percentage of TMS in the case of NCDS2, and NCDS3 corresponds to 0.0066 and 0.0384% for 2.5 and 15 sccm, respectively while H₂ and CH₄ gas flow rates are 400 and 2.5 sccm, respectively. NCDS1, NCDS2, and NCDS3 are deposited for 6 h. Percentage of CH₄ in H₂ during bias enhanced nucleation was 4%. It is evident from the choice of TMS flow rate that the incorporation of β -SiC phase varied significantly in the resultant diamond/ β -SiC nanocomposite thin films NCDS2 and NCDS3 in comparison to NCDS1.

To test the mechanical contact damage behavior of the diamond/ β -SiC nanocomposite films, a ~ 3 μm thick diamond/ β -SiC nanocomposite film grown on manually diamond pre-treated polycrystalline W substrate was considered. The considered thin film was deposited using the same experimental conditions of NCDS series samples except for the TMS flow rate of 5 sccm. For comparison purpose, a ~ 3 μm thick diamond thin film grown (using the exact experimental conditions as that of the diamond/ β -SiC nanocomposite film grown on W) on manually diamond pre-treated polycrystalline W substrate was also considered.

3.1.2 Graphitic carbon nitride ($g\text{-C}_3\text{N}_4$)

In this work, as-synthesized $g\text{-C}_3\text{N}_4$ was named as GCN. The graphitic carbon nitride ($g\text{-C}_3\text{N}_4$) was synthesized by thermal decomposition of Urea at 500 °C. As-synthesized GCN powder was made into pellets of size ~ 10 mm diameter and thickness of ~ 2.5 mm by applying a pressure of ~ 3 Tons.

3.2 Surface Modification Procedures

3.2.1 Gamma irradiation

The gamma (γ) irradiated diamond films are named as NCD1-100, NCD1-1000, NCD1-2000, NCD2-100, NCD2-1000, NCD2-2000, NCD3-100, NCD3-1000 and NCD3-2000 depending on the dose (100, 1000 and 2000 kGy) of radiation. γ irradiation was carried out using gamma chamber (GC 1200) shown in Fig. 3.1. Co^{60} is the radiation source, which emits gamma rays. The average energy of the gamma rays is ~ 1.258 MeV. The GC1200 gamma chamber contains various required components viz., gamma source, gamma shielding, sample space, outer cabinet and controlling system etc. The whole system is operated electronically. The chamber has an irradiation volume $\sim 1,000$ cm³ with uniform gamma environment where samples are placed for irradiation. The samples are placed inside the irradiation zone by using a steel rod which is operated from outside. The sample position can be adjusted at desired place by using steel rope and geared motor operates electronically from outside. The gamma rays dose rate was 5.49 kGy/h at the time of irradiation.



Figure 3.1 Gamma Chamber (GC 1200) at the Inter University Accelerator Center (IUAC), New Delhi (www.iuac.res.in)

3.2.2 Ion irradiation

Ion beams are utilized to alter the chemical, electronic and structural properties by injecting (doping) atoms into the target (here diamond films and $\text{g-C}_3\text{N}_4$). Ion irradiation may result in atomic displacement of target and further causes its damage. The kinetic effects of ion beam interactions with target material are estimated by using Monte Carlo simulation of ‘*Stopping and Range of Ions in Matter (SRIM)*’[®] software. In the present work, all three diamond thin

Experimental Work

films (NCD1, NCD2 and NCD3) were irradiated with three different energies of nitrogen beam viz., 12 keV, 100 keV and 70 MeV at different fluences. Also, as-synthesized g-C₃N₄ pellets were irradiated with 200 keV Si beam at different fluences. Before ion beam irradiation, the samples were mounted on ladder as shown in Fig. 3.2 and placed inside a high vacuum chamber maintained at a vacuum of 1×10^{-6} Torr. In order to homogeneously irradiate the samples, the focused ion beam was carefully scanned over an area of 10×10 mm². The irradiation experiments were performed at ambient conditions i.e., at room temperature using the different accelerator facilities explained in the following paragraphs.



Figure 3.2 Ion irradiation experimental ladder with mounted samples.

Table top ion accelerator: The considered diamond thin films were irradiated with nitrogen ion beam of energy 12 keV with a fluence of 1×10^{16} ions/cm² by using the table top ion accelerator shown in Fig. 3.3. This facility provides implantation using Alpha (α), Proton (H^+), Molecular Hydrogen (H_2) and Nitrogen beams up to 60 kV without any hazardous radiation effects. The major parts of this machine are Penning Ion Generator (PIG) ion Source, Electrostatic Quadrupole Triplet and Permanent Magnets known as Bending Magnets. The PIG works on cold plasma and able to produce 300 μ A constant current. This ion source is placed inside a nylon chamber and coupled to a 60 kV power supply. The required gas for which ion beam is needed is sent through a needle valve mounted at the high voltage end. The electromagnets used for the confinement of beam are made up of Al placed inside a stainless steel vacuum jacket. The nitrogen irradiated diamond films using this facility are named as NCD1L-1E16, NCD2L-1E16 and NCD3L-1E16.



Figure 3.3 Table top ion accelerator set-up at IUAC, New Delhi.

Experimental Work

Low energy ion beam accelerator: The diamond thin films were irradiated with nitrogen ion beam of energy 100 keV with fluences $1E16$ and $1E17$ ions/cm² using low energy ion beam accelerator shown in Fig. 3.4. This facility is based on electron cyclotron resonance (ECR) ion source. It can provide ion beams of energy ranging from keV to few MeV. The special feature of this machine is the availability of multiple positive ions with large currents. The ion source in this facility is operated at a frequency of 10 GHz. The ion beam is extracted by electromagnet and focused on the sample by using Einzel lens, a type of charged particle lens which can focus the ion beam without losing the energy. The Einzel lens is operated at 200 kV and controlled using an optical fibre communication. The energy (E) of ion beam coming out from this facility is calculated by using the equation, $E = q (v_s + v_p)$ where q is the charge state of the ion, v_s is the potential of ion source (in kV) and v_p is the potential of high voltage platform (in kV).



Figure 3.4 Low energy ion beam facility setup at IUAC, New Delhi.

Samples are mounted on a ladder (shown in Fig 3.2) made up of stainless steel and placed in a high vacuum chamber, which is connected with beam line at one end. The ion beam falls directly on the samples at 90° angle. For uniform irradiation, an electrostatic beam scanner which can scan an area of 10 mm x 10 mm both in x- and y-directions is used. The irradiated diamond films using this facility are named as NCD1-1E16, NCD1-1E17, NCD2-1E16, NCD2-1E17, NCD3-1E16 and NCD3-1E17 corresponding to the fluences used.

Source of negative ions by Cs sputtering (SNICS): In SNICS the negative ions of desired elements are produced by bombarding hot Cesium ions (Cs^+) with the solid material (source) atoms. The setup contains a discharge chamber in which a reservoir at high temperature is maintained. A small cylindrical piece of Cu on which Cs is coated acts as cathode. The element for which negative beam is required is taken in the form of powder inside the chamber. Total setup is maintained under ultra-high vacuum conditions. When the Cs atoms come in vicinity of hot reservoir, it boils away and gets ionized. These ionized Cs^+ ions get accelerated towards

Experimental Work

the cathode on the way sputtering the atoms of powdered sample and resulting in the production of negative ions. These negative ions are further accelerated and extracted out at the end of the chamber. The negative ion implanter setup is depicted in Figure 3.5.



Figure 3.5 Source of negative ions by cesium sputtering setup at IUAC, New Delhi.

Pelletron accelerator: A high energy Pelletron accelerator [11] (shown in Fig. 3.6) was used to irradiate NCD1, NCD2, and NCD3 thin films with nitrogen ion beam of energy 70 MeV. The fluences used are 1×10^{12} and 1×10^{13} ions/cm². The pelletron accelerator used in this work is known as 15 UD Pelletron. Here the number 15 represents 15 MV terminal voltage, which is maintained at the center of the machine and “UD” signifies unit double. The pelletron is able to accelerate any ions from proton (H⁺) to uranium (U) up to energies of a few hundred MeV based on nature of the ions. The negative ions, for which desired beam is required are obtained by SNICS method (previous page). The obtained negative ions are feed into the pelletron tank by using injector magnets. These negative ions are accelerated towards the centre of the tank, which is maintained at positive 15 MV. There is a stripper foil, which removes some of the electrons from the ions making them as positive. These positive ions are further repelled towards the ground at zero potential. The positive ions are accelerated twice by maintaining 15 MV potential at the centre, resulting in ions getting accelerated with twice energy which is the above mentioned UD. The total energy gained by an ion is given by $\mathbf{E} = [\mathbf{E}_{\text{deck}} + \mathbf{V}(\mathbf{q} + \mathbf{1})] \text{ MeV}$, where V and q represents the terminal voltage (in MV), charge state of ions respectively being accelerated after passing through the stripper foils, and \mathbf{E}_{deck} is the deck potential of the SNICS which is in the order of few hundred kV. The energetic ion beams are analyzed by using permanent dipole magnets known as analyzer magnets and further directed into the experimental chambers through dedicated beam lines by using multi pole switching magnets. The entire beam line is maintained at ultra-high vacuum (at pressure $< 10^{-8}$ mbar) conditions with ion beam passing along the centre of the beam line. The ion beam is

Experimental Work

focused on the sample (here diamond thin films) by using steering magnet and quadrupole magnet. The size of ion beam is around 1 mm. The sample is irradiated by ion beam through scanning the entire area in a roaster format. A constant beam current of 1pA^* is being maintained throughout the irradiation. The time of irradiation of the sample for various fluences is calculated by the following formula as described in next page. The irradiated diamond films using this facility were named as NCD1-1E12, NCD1-1E13, NCD2-1E12, NCD2-1E13, NCD3-1E12 and NCD3-1E13 corresponding to the fluences 1×10^{12} and 1×10^{13} ions/cm².

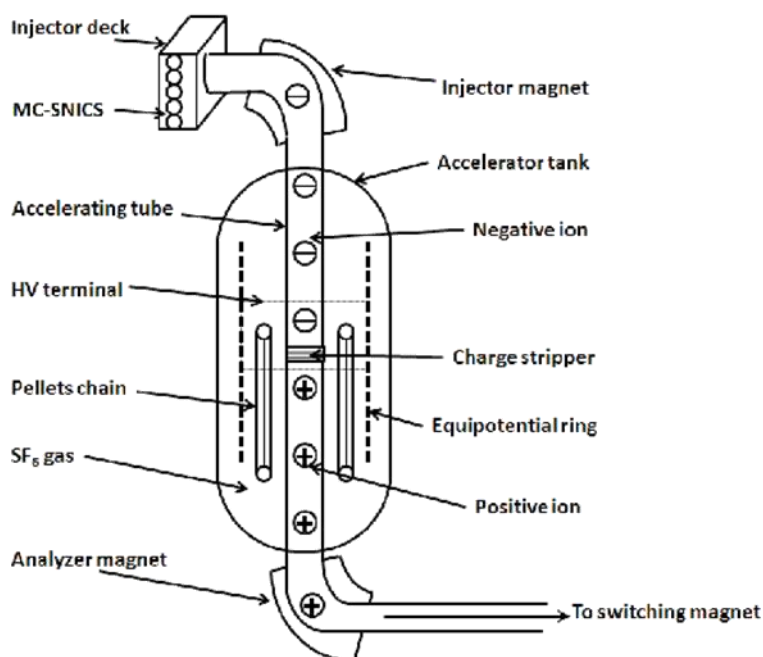


Figure 3.6 Schematic of the pelletron accelerator used in this work.

In this work, as-synthesized g-C₃N₄ pellets were also irradiated with Si beam of energy 200 keV with fluences 2×10^{15} , 3×10^{15} , 5×10^{15} , 1×10^{16} , 2×10^{16} and 3×10^{16} ions/cm². These samples are correspondingly named as Si-2E15, Si-3E15, Si-5E15, Si-1E16, Si-2E16 and Si-3E16. From the “Stopping and Range of Ions in Matter (SRIM)” simulation, for Si ion implantation in g-C₃N₄ the range (R_P), electronic energy loss (S_e) and nuclear energy loss (S_n) are calculated as ~ 345 nm, 380.3 and 166.4 keV/ μm , respectively.

* PnA stands for particle nano Ampere, which is the practical unit for ion irradiation purpose. An ion beam is a collection of ions with different charge states from single element. In order to calculate the effective current of the ion beam the total current of the beam is divided by charge state to attain particle nano ampere (pna).

Experimental Work

The considered diamond thin films (NCD1, NCD2 and NCD3) were irradiated with different ion fluences. The ion fluence (ϕ in ions/cm²) directly depends on the beam current (I in pA), time of irradiation (T) and area of the sample (A). The T required for a particular fluence is given by $T = \frac{\phi A}{I \cdot 6.25 \cdot 10^9}$. An energetic ion passing through the target loses its kinetic energy (KE) through sattering, which involves the Coulomb interaction between incoming ion species and both target atom and its electronic system as well. This energy loss determines the final range (penetration depth) of the incoming ion beam (projectile) into the target (solid) and the lattice disorder created by the ions. The interaction of energetic ions with solid material (named as target) results in energy loss of ions. Depending on the thickness of the target, when the ions pass through a target, energy loss of ions must be considered. Energy losses vary with the target materials. The energy loss of ions in matter (target) is calculated using SRIM® software which is based on Monte Carlo simulation of interactions between ions and target materials. SRIM provides quick calculations of stopping energies, projected range and straggling distributions for any energetic ion in single and multi-layer targets. In the present work, the range (R_p), nuclear energy loss (S_n) and electronic energy loss (S_e) are calculated using SRIM software for all the diamond thin films. The depth profile of nitrogen ion beam in diamond film with 100 keV energy is shown in Fig. 3.7. Similarly, the calculated R_p , S_n , S_e values for nitrogen ion beam with different energies are given in Table 3.2 which also shows the N^+ irradiation parameters in different experiments.

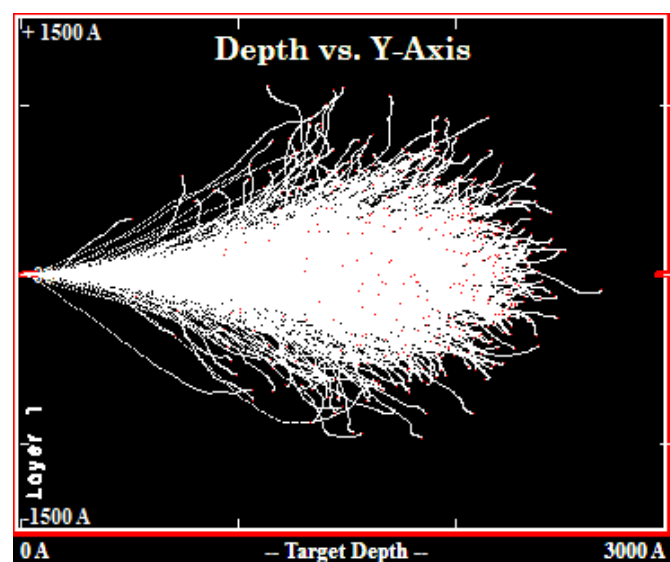


Figure 3.7 Nitrogen ion (100 keV) depth profile within a diamond film as calculated by SRIM software.

Experimental Work

Table 3.2 Experimental details of N⁺ ion irradiation on the considered diamond thin films.

| Energy (keV) | Facility | Fluence (ions/cm ²) | Current (μA) | Range (nm) | S _n (keV/μm) | S _e (keV/μm) |
|--------------|-----------------------|--|--------------|------------|-------------------------|-------------------------|
| 12 | Table Top Accelerator | 1x10 ¹⁶ | 50 | 26.2 | 204 | 210 |
| 100 | LEIBF | 1x10 ¹⁶ 1x10 ¹⁷ | 2 | 179.8 | 75.9 | 525 |
| 70000 | 15 UD Pelletron | 1x10 ¹² 1x10 ¹³ | 0.003 | 61.2 | 0.4 | 758.4 |

3.3 Characterization

3.3.1 Electron microscopy

In the present work, Scanning Electron Microscopy (SEM) was used to obtain the morphologies of both surface and cross-sectional views of the samples. In order to get the secondary electron (SE) images of the sample surfaces, surface must be electrically conducting. Otherwise, the surfaces being probed get charged up. In case of diamond and diamond/β-SiC composite thin films, the conducting graphite phases present in the grain boundaries make the sample surface conducting on the whole. Therefore no conducting coating was used on these film surfaces. However, in the case of graphene nitride (g-C₃N₄) samples, since they are not good conductors and conducting Au coating was used on these samples prior to the examination. Zeiss Ultra55 ultra high resolution field emission scanning electron microscope (FESEM) was used to observe the morphological surface changes of the samples at a working distance of ~5 mm and at an accelerating voltage of 5 kV. The energy dispersive x-ray (EDX) analysis was used to obtain elemental composition of sample surfaces. In this analysis, emitted x-rays (due to interaction with sample surface) are collected using a detector which carries the characteristics of elements present in the sample surface. In this analysis, working distance of 7 mm and an accelerating voltage of 15 kV were used. Transmission electron microscope (TEM, model FEI Technai G2 S-Twin) was also used to observe morphological features in selective diamond films. Free standing thin diamond films were placed on a holy carbon coated copper grid for TEM examination. The TEM was operated at 200 kV.

3.3.2 X-ray and electron diffraction

In this work, grazing incidence x-ray diffraction (GIXRD) measurements were accomplished in grazing incidence geometry to determine the crystallinity of the thin films in the range of 2θ from 30-100° (range varies with material) with a step size of 0.02°. For the considered thin

Experimental Work

films, Bruker D8 Discover diffractometer was used to obtain the GIXRD patterns. Cu K α ($\lambda=1.54 \text{ \AA}$) source was used and a separate rotating base was mounted as a detector. The x-rays were produced from Cu target by electron beam of current 40 mA. The angle between incident x-rays and sample surface was fixed at 1.5° and the rotating detector measured the 2θ angle. The standard Scherrer's formula was used to estimate the crystallite sizes in the considered diamond thin films. The crystallinity of bulk g-C $_3$ N $_4$ powder samples was determined using the standard powder XRD technique. In this case, XRD measurements were performed using Bruker AXS model D8 Advanced system in the range of 2θ from $5-70^\circ$ with a step size of 0.02° . Selected area electron diffraction (SAED) patterns were also recorded in the case of selected samples to complement the XRD results. In few cases, high resolution transmission electron microscope (HRTEM) images were also used to confirm the crystallinity (by directly marking the inter-planar spacing between the lattice fringes). XRD and SAED patterns were indexed by following the standard procedures. In the case of powder XRD patterns, matching with the standard JCPDS data files was also carried out.

3.3.3 Spectroscopy

To understand the phase content of different samples, micro-Raman spectroscopy measurements were accomplished using Wi-Tec alpha 300 AR laser confocal optical microscope (T-LCOM) in a back scattering mode. Raman spectra were collected by an argon ion 488 nm CW laser as the excitation source. This facility contains charge coupled device (CCD) detector, which is cooled by means of Peltier. In the case of diamond thin films, micro-Raman spectroscopy measurements was carried out with the laser power and numerical aperture as 20 mW and 0.95, respectively. The beam was focused onto the diamond thin film surfaces by means of 20x objective lens. The integration time was typically 1 second and the data acquisition time was 10 seconds. Similarly, in the case of diamond/ β -SiC composite thin films, micro-Raman spectroscopy measurements were carried out with LabRam HR800 Raman spectrometer. In this case, 514.5 nm Ar $^+$ ion laser with 2.8 mW power was used as an excitation source with 10x objective lens. In these measurements the data acquisition time was 5 seconds. In both diamond and diamond/ β -SiC composite thin films' cases, the spectral resolution was 1 cm^{-1} and the scattered light from the samples was dispersed on to the CCD detector.

In this work, all implanted diamond films are characterized with Rutherford backscattering (RBS) technique to analyse the elemental composition and depth profile of the implanted ion. RBS system used in this work was equipped with 1.7 MV 5SDH-2 Pelletron accelerator,

Experimental Work

manufactured by National Electrostatics Corp, USA. The alpha ion (He^{2+}) beam (produced from an alphasource ion source) with 3.72 MeV energy was used for the scattering purpose. One end of RBS beam line is attached to the sample chamber maintained under ultra-high vacuum conditions. This system contains 4 axis goniometer on which samples up to 15, based on the size can be mounted at one time for analysis. A surface barrier detector and corresponding electronic communication setup is used to detect the number and energy of backscattered ions after colliding with atoms of the sample. This enables to find out elemental composition and concentration with respect to depth of the sample under study. The obtained data from RBS spectrum of samples is carried out by using RUMP software to find out elemental analysis and depth profile of the all implanted diamond films.

To understand the molecular structure and quality of bonding of carbon at the surface of as-deposited diamond films X-ray absorption fine structure (XAFS) spectroscopy technique was used. XAFS utilizes high energy x-rays to probe the core electron shell of atoms. In this one can obtain the data about electronic structure depending on the mode in which x-rays are collected and therefore molecular bonding states of matter within first few nanometers in a sample. Within the body of XAFS technique, near-edge x-ray absorption fine structure (NEXAFS) probes the electron transition from K-shell of low Z elements (here carbon) within the first few nanometers of a material. The bond length or orientation of molecular bonds can be observed from location of peaks within a NEXAFS absorption spectra. In this work (Model: 10D XAS KIST B/L) NEXAFS was utilized to confirm the presence of diamond, sp^2 structure and to assess the general quality of sp^3 bonds between the diamond films. XAFS spectroscopy was carried out to know the quality of the as-deposited diamond films in correlation with XRD and Raman scattering results.

In the case of $\text{g-C}_3\text{N}_4$, Fourier transform infrared (FTIR) spectroscopy measurements were done using Perkin-Elmer (spectrum bx) in the wavenumber range of $400\text{-}4000\text{ cm}^{-1}$. In the IR spectroscopy, when the IR rays incident on all $\text{g-C}_3\text{N}_4$ samples, some of the rays are absorbed by the sample and some are transmitted (passes) through the sample. The absorption occurs when the energy of the beam of light is transferred to the sample constituents. These constituents get excited and the transferred energy cause vibrations in the molecular bonds. The recorded signal at the detector is a spectrum representing a molecules present the $\text{g-C}_3\text{N}_4$ sample. By employing the interferometer, FTIR spectroscopy record the information of material which is exposed by IR rays. The spectral resolution of the measurements was 8 cm^{-1} and the transmitted light from the samples was detected by Liquid nitrogen cooled mercury

Experimental Work

cadmium telluride (MCT) detectors which have higher sensitivity and faster response. The C_3N_4 samples were mixed with spectroscopic grade KBr and pressed into transparent thin pellets. These pellets were used for FTIR measurements.

3.3 Mechanical Contact Damage Tests

In order to assess the mechanical contact damage behavior of diamond/ β -SiC nanocomposite thin film in comparison to a diamond thin film, Brinell indentation tests were carried out. The idea behind such an indentation test is to cause film failure at the interface and then to evaluate the adhesion strength by measuring the load applied to the indenter leading to the film's plastic deformation. The indenter had a spherical shape (diameter = 3.45 mm) and was made of WC. Discrete indentation loads of 30, 60, 125 and 150 kgf were applied on the surface of diamond and diamond/ β -SiC nanocomposite thin film surfaces. If the normal load is high enough then the circumferential and lateral cracks are initiated and propagated between the film and the substrate and also appear on the surface due to the plastic deformation of the films. Qualitative adhesion evaluation was then made depending on scanning electron microscope (SEM) observations of the crack formation and evolution on the surface of the films. Using SEM the lateral crack length was carefully measured. The obtained results were then plotted with respect to the applied normal loads. The slope acquired from this plot resembles the ease of lateral crack propagation, which changes linearly with $1/G_c$ where G_c indicates release rate of critical strain energy of the crack evolution and was therefore used as a measure to evaluate adhesion.

3.4 Electrical Conductivity Measurements

To understand the variation in electrical properties in the case of selected irradiated samples, transport (electrical) properties and Hall measurements were accomplished. In case of selected N^+ implanted diamond films, electrical measurements (I-V) were carried out with four probe method by using Keysight Semiconductor Device Analyzer (model: B1500A) in the voltage range of -5 V to 5 V. By using this instrument, accurate and precise current measurements in the range 0.1 fA to 1 A can be measured. The resolution and accuracy of the device are 100 aA and $\pm (0.9\%+12 \text{ fA})$, respectively. The diamond films are placed on stainless steel (SS) platform which are mounted on a probe station. In order to isolate the samples electrically with SS platform a small piece of mica sheet was placed beneath them. To ensure better electrical contact, gold coated electrical probes are used. Figure 3.8 shows the probe station used in this study. The device analyzer is automated for better recording of data to a computer through General Purpose Interface Buss (GPIB) cables by using a LabVIEW^(TM) program.

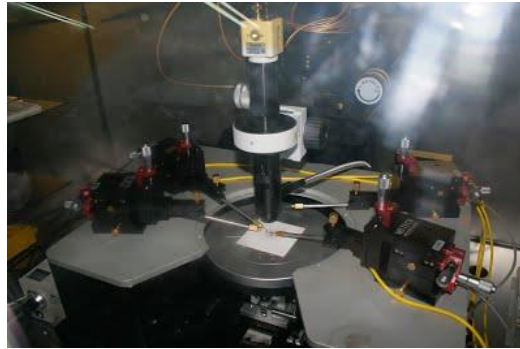


Figure 3.8 Probe station microscope used to measure I-V characteristics of selected N^+ ions implanted diamond thin films in comparison to the as-deposited diamond thin film.

I-V characteristics were also measured in the case of diamond/ β -SiC composite thin films were measured by two point probe (Fig. 3.9) method in the applied voltage range of -5 V to 5 V. Two Ag-paint dots (diameter ~ 1 mm) spaced ~ 0.5 mm from each other on the film surface are used at the electrodes. I-V characteristics of thin film/substrate junction were also measured in the case of diamond/ β -SiC composite thin films. The measurements were carried out by using the configuration shown in Fig. 3.10. Ag-paint dot (diameter ~ 2 mm) is placed on the surface of the film and exactly at the back of the Si substrate. Then, the sample is placed on a Cu sheet and the I-V characteristics are acquired between the Ag-paint dot on the film and the Cu sheet. The samples were dipped in 5% HF solution for 15 s to remove oxide layer before placing the Ag-paint dots. The voltage range used is -10 V to 10 V.



Figure 3.9 Schematic of the two point probe configuration for measurements of surface I-V characteristics of diamond/ β -SiC composite thin films.



Figure 3.10 Schematic of the configuration for measurements of I-V characteristics of diamond/ β -SiC composite thin film/Si substrate junction.

In the case of diamond/ β -SiC composite thin films, Hall measurements (to know carrier density, type of charge carriers and Hall mobility due to the presence of β -SiC phase along with

Experimental Work

diamond) were also performed in the Van der Pauw geometry (Fig. 3.11) at room temperature in an external magnetic field range of 0.1 T to 1 T. Four Ag-paint dots (diameter ~ 1 mm) were placed as metal contacts. L in Fig. 3.11 varied in different cases and accordingly the calculations were carried out. Also the thickness of the thin films (~ 3 μm) was considered in calculating the corresponding carrier densities.



Figure 3.11 Schematic of the configuration for Hall measurements on diamond/ β -SiC composite thin films.

Chapter 4 Results and Discussion

4.1 Gamma (γ) Irradiated Diamond Thin Films

4.1.1 Characteristics of as-deposited diamond thin films

Low and high magnification plane view secondary electron (SE) micrographs of as-deposited NCD1, NCD2 and NCD3 films are shown in Fig. 4.1. In all the cases of as-deposited NCD1, NCD2 and NCD3 films, the thin film surface morphology is homogeneous with randomly oriented features (diamond grains). In the case of NCD1 and NCD2 films, the diamond grain-edges are sharp and diamond grains are of different sizes. In the case of NCD3, a cauliflower-like morphology is witnessed. The discernable feature sizes in the cases of NCD1, NCD2 and NCD3 are less than 100 nm, tens of nm to 200 nm, and few nm to 10 nm, respectively.

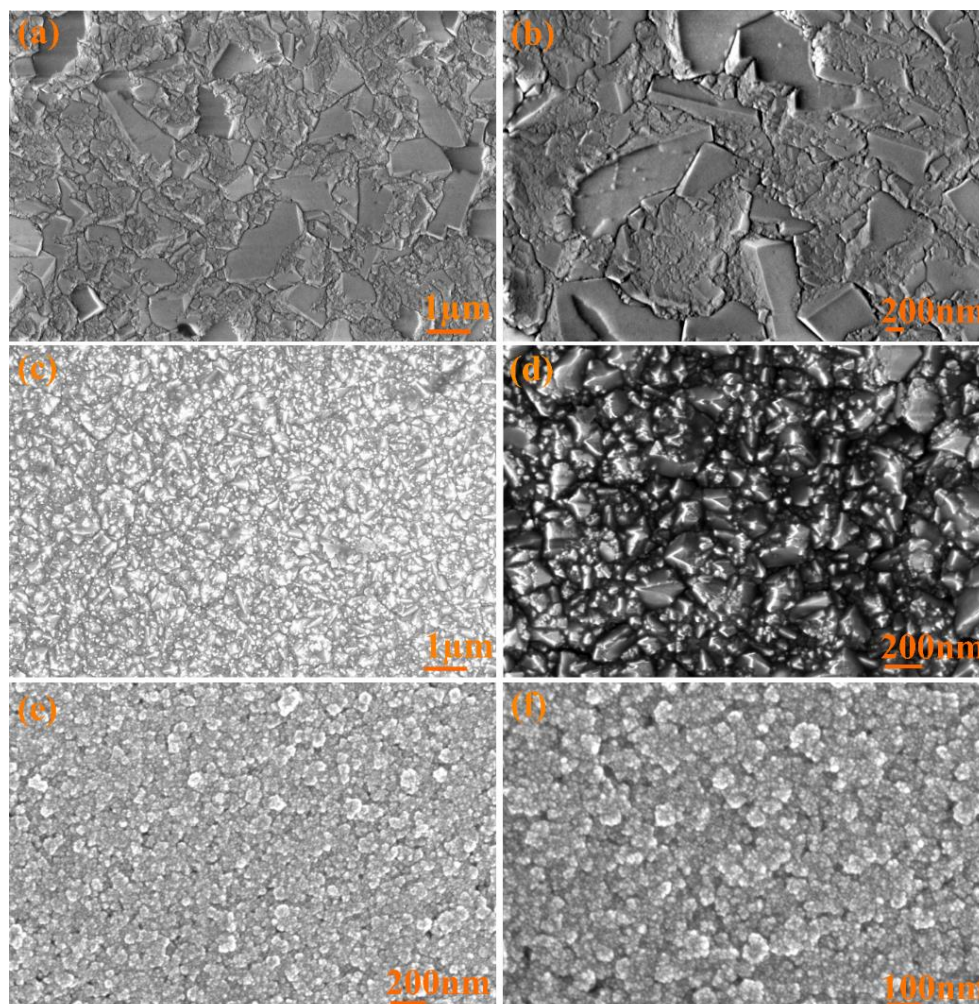


Figure 4.1 Plane view secondary electron micrographs of (a) NCD1, (c) NCD2, (e) NCD3 at low magnification; (b), (d), and (f) are the corresponding high magnification micrographs.

Results and Discussion

GIXRD patterns of NCD1, NCD2 and NCD3 are presented in Fig. 4.2. In case of NCD1 and NCD2, the characteristic diffraction peaks at $2\theta = 43.9^\circ$, 75.2° and 91.4° correspond to (111), (220) and (400) diffraction planes in diamond, respectively and their appearance indicates the polycrystalline nature of NCD1 and NCD2 films. The peak broadening in NCD2 film as compared to NCD1 film indicates decrease in diamond grain size. In the case of NCD3, only a faint (111) diamond diffraction peak is observed. The background noise levels in the case of NCD2 and NCD3 are higher in comparison to NCD1 indicating lesser diamond phase purity in the former two cases. The average grain size (calculated by taking into account (111) diffraction peak) in NCD1, NCD2, and NCD3 films is ~ 55 , 25 , and ~ 16 nm, respectively. These values are comparable to the surface features in the respective films shown in Fig. 4.1. The GIXRD results confirm the nanocrystalline nature of diamond in NCD1, NCD2 and NCD3 films [1-5].

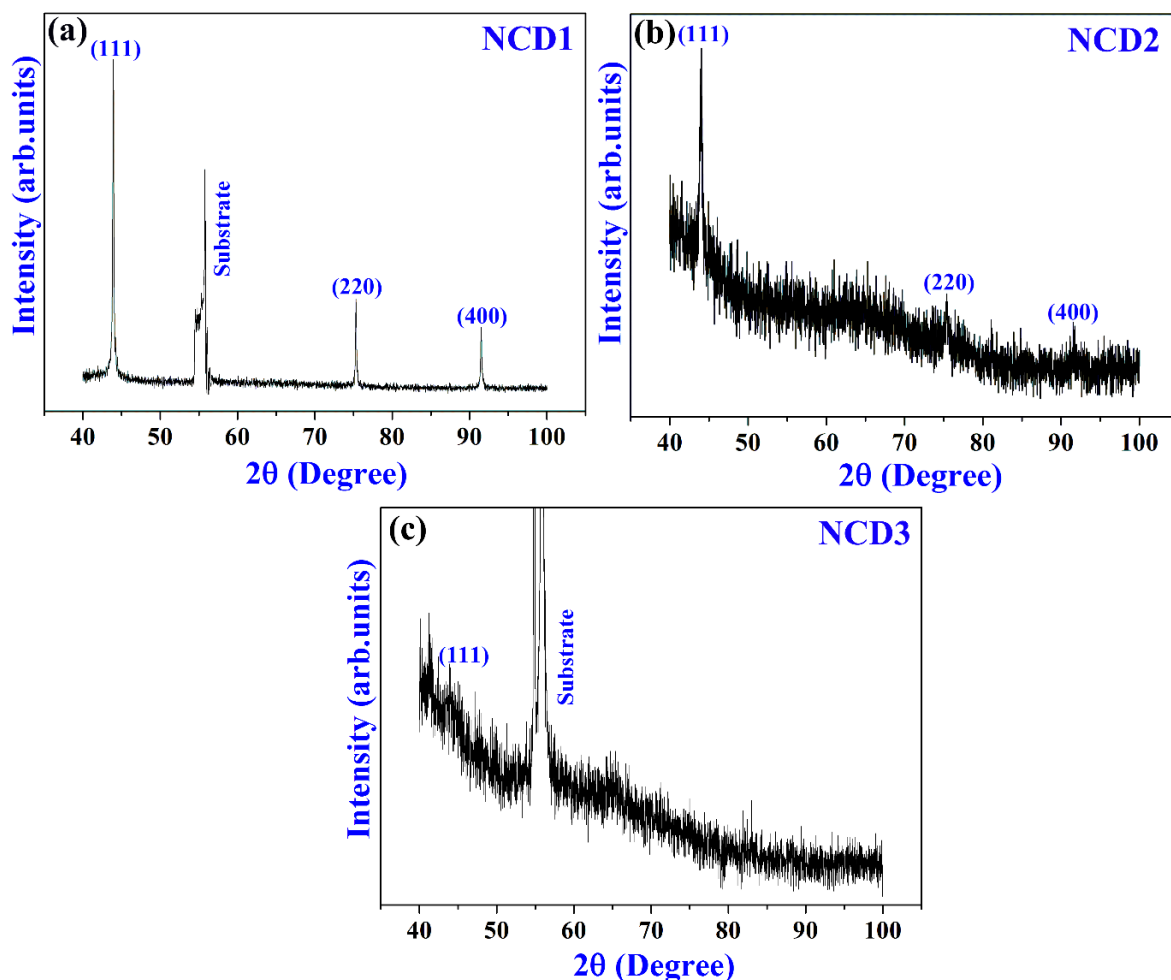


Figure 4.2 Grazing incidence X-ray diffractograms of as-deposited (a) NCD1, (b) NCD2 and (c) NCD3 thin films.

Results and Discussion

Raman spectra of NCD1, NCD2 and NCD3 are shown in Fig. 4.3. In all cases, a slightly blue shifted (from 1332 cm^{-1} to a higher wavenumber) and broadened peak corresponding to zone-center phonon in diamond is observed [6-18]. The blue shift indicates compressive stress in the film due to the diamond film's thermal mismatch with the substrate [19]. The broadening of diamond peak is due to the nanometer size of diamond grains [20, 21] well-complementing with the GIXRD results. The broad Raman signal at $\sim 1500\text{ cm}^{-1}$ is the characteristic G band corresponding to the sp^2 bonded graphitic carbon at the grain boundaries in the thin films [13-15]. NCD2 and NCD3 show important broad bands centered at ~ 970 and $\sim 1140\text{ cm}^{-1}$ (in addition to ~ 1332 , and ~ 1500 - 1600 cm^{-1} bands) corresponding to 2nd order phonon mode of Si (from the 'Si' substrate indicating that the film is thin) and trans-polyacetylene (t-pa) portions [12,22,23] at diamond grain boundaries and surfaces in the film. On the contrary NCD1 showed only the t-pa band at $\sim 1124\text{ cm}^{-1}$. In the case of NCD3, $\sim 970\text{ cm}^{-1}$ band is sharper than in NCD2 indicating that NCD3 film is thinner than NCD2 film. This correlates well with the noise observed in the corresponding GIXRD patterns shown in Fig. 4.2. The broadening of zone-center phonon band is the maximum in the case of NCD3 followed by that in NCD2 and then NCD1, another observation which correlates well with the diamond grain sizes as calculated from GIXRD patterns. The estimated intensity ratio $\frac{I_{\text{Diamond}}}{I_{\text{Diamond}}+I_{\text{G}}}$ values (after proper peak fitting [24]) for NCD1, NCD2 and NCD3 are 0.4, 0.28 and 0.25, respectively indicating that NCD1 is good quality (diamond quantity wise) nanodiamond film as compared to NCD2 and NCD3 films. The NCD2 and NCD3 films have more amount of graphitic carbon as compared to NCD1 film which is due to the presence of smaller grains in these films as compared to NCD1 film. The carbon K-edge and oxygen K- near edge X-ray absorption fine structure (NEXAFS) spectra of NCD1, NCD2 and NCD3 films are shown in Fig. 4.4. The peak at energy $\sim 284.5\text{ eV}$ in pre-edge region corresponds to $\text{C } 1s \rightarrow \pi^*$ transition [25]. This peak indicates the existence of sp^2 -hybridized carbon at the diamond grain boundaries. The peak at $\sim 289.5\text{ eV}$ corresponds to $\text{C } 1s \rightarrow \sigma^*$ transition in diamond [25]. The absorption edge at $\sim 289.0\text{ eV}$ and a dip owing to second band gap of diamond at 302.0 eV are exclusive features of high quality of diamond [26] that is constituted in the films. These bands are consistent in all the cases, confirming that the diamond present in these films is of high quality. The O K-edge in all the three cases is observed at 532.9 eV ($\text{O } 1s \rightarrow \pi^*$ transition) and 539.7 eV ($\text{O } 1s \rightarrow \sigma^*$ transition) [27]. All in all, the results show that the diamond films considered in this work are very good for irradiation experiments mainly owing to the quality of diamond present in the thin films and to the quantity of diamond phase in the thin films in the order $\text{NCD1} > \text{NCD2} > \text{NCD3}$.

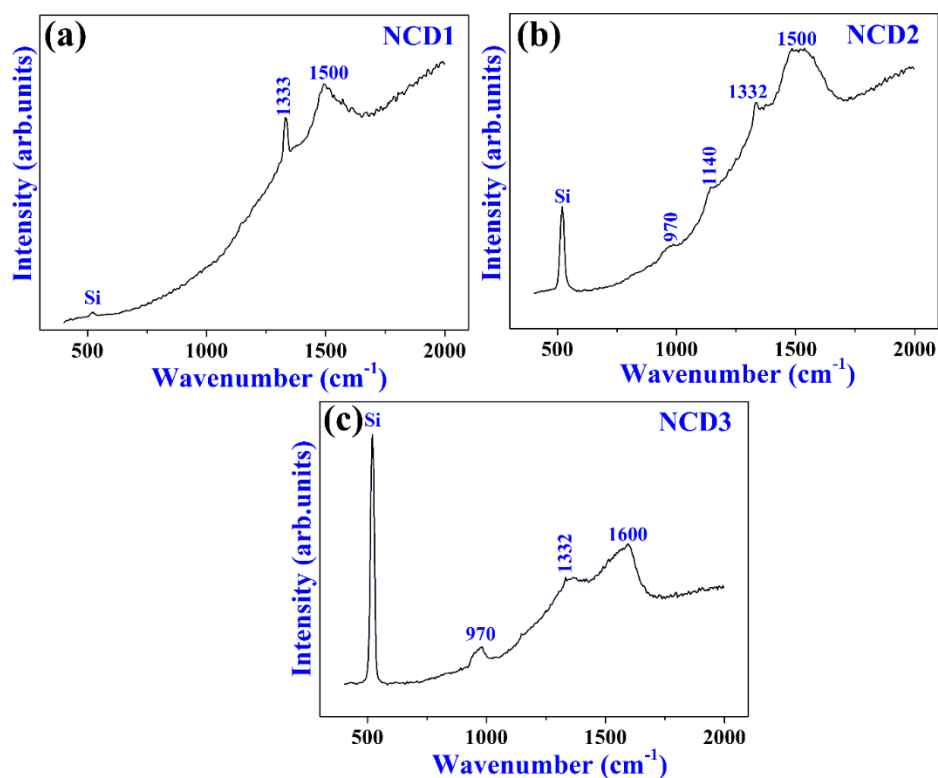


Figure 4.3 Raman spectra of as-deposited (a) NCD1, (b) NCD2 and (c) NCD3 thin films.

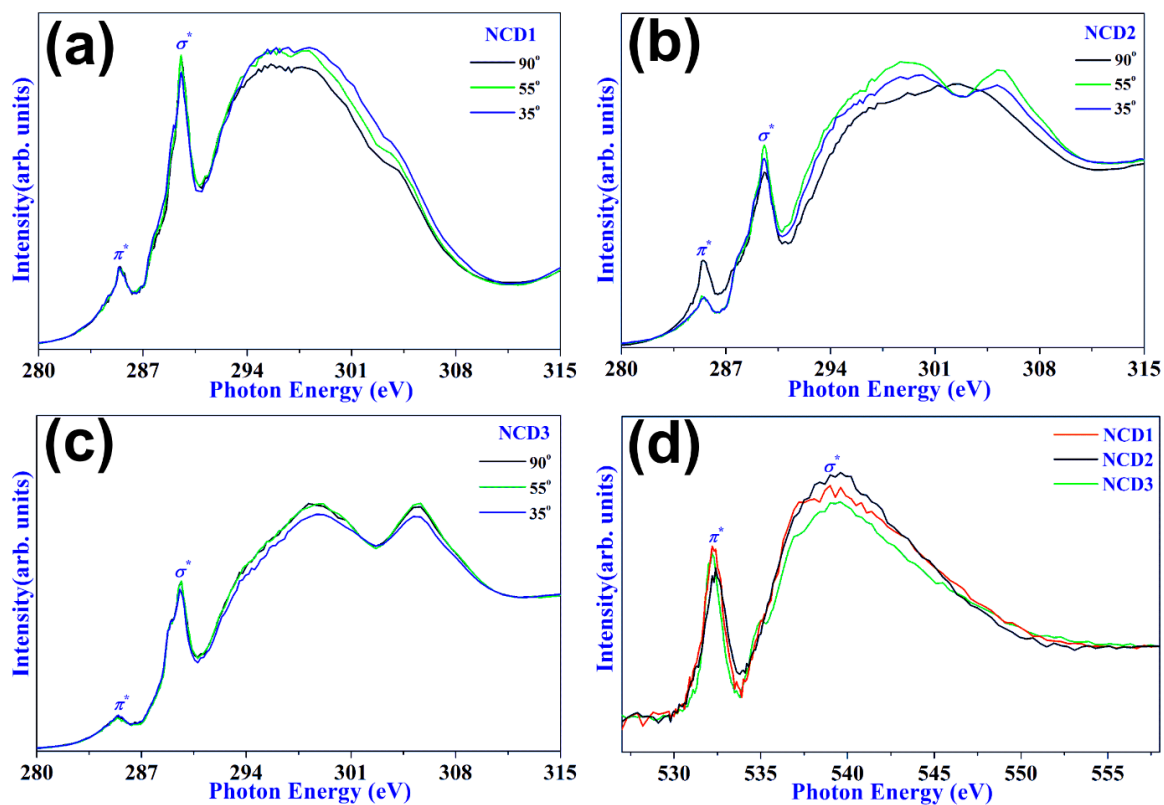


Figure 4.4 Near edge X-ray absorption fine structure spectra of the as-deposited (a) NCD1, (b) NCD2 and (c) NCD3 thin films; (d) O K-edge spectra in all the three cases.

4.1.2 Characteristics of the γ -irradiated diamond thin films

Low and high magnification plane view secondary electron micrographs of gamma (γ) irradiated (with doses of 100, 1000 and 2000 kGy) NCD1, NCD2 and NCD3 films in comparison to the respective as-deposited NCD1, NCD2 and NCD3 films are shown in Fig. 4.5, Fig. 4.6, and Fig. 4.7, respectively. It can be clearly observed from the surface morphology images of the irradiated surfaces that after the irradiation, there is no appreciable change in surface morphology of these films except for the slight rounding-off of the edges of diamond grains in the films. GIXRD patterns (Fig. 4.8) and Raman spectra (Fig. 4.9) of gamma irradiated NCD1, NCD2 and NCD3 films in comparison to the respective as-deposited NCD1, NCD2 and NCD3 films show miniscule or no changes indicating that the considered diamond films are stable w.r.t crystallinity and phase to the considered γ irradiation unlike in the cases reported in the literature and discussed in Chapter 2. All in all, it is clear from the characterization results that in all diamond films (NCD1, NCD2, NCD3), the carbon material undergoes internal $sp^2 \leftrightarrow sp^3$ or $sp^3 \leftrightarrow sp^2$ bonding interconversions upon γ -radiation without changing its overall sp^3/sp^2 composite character [28].

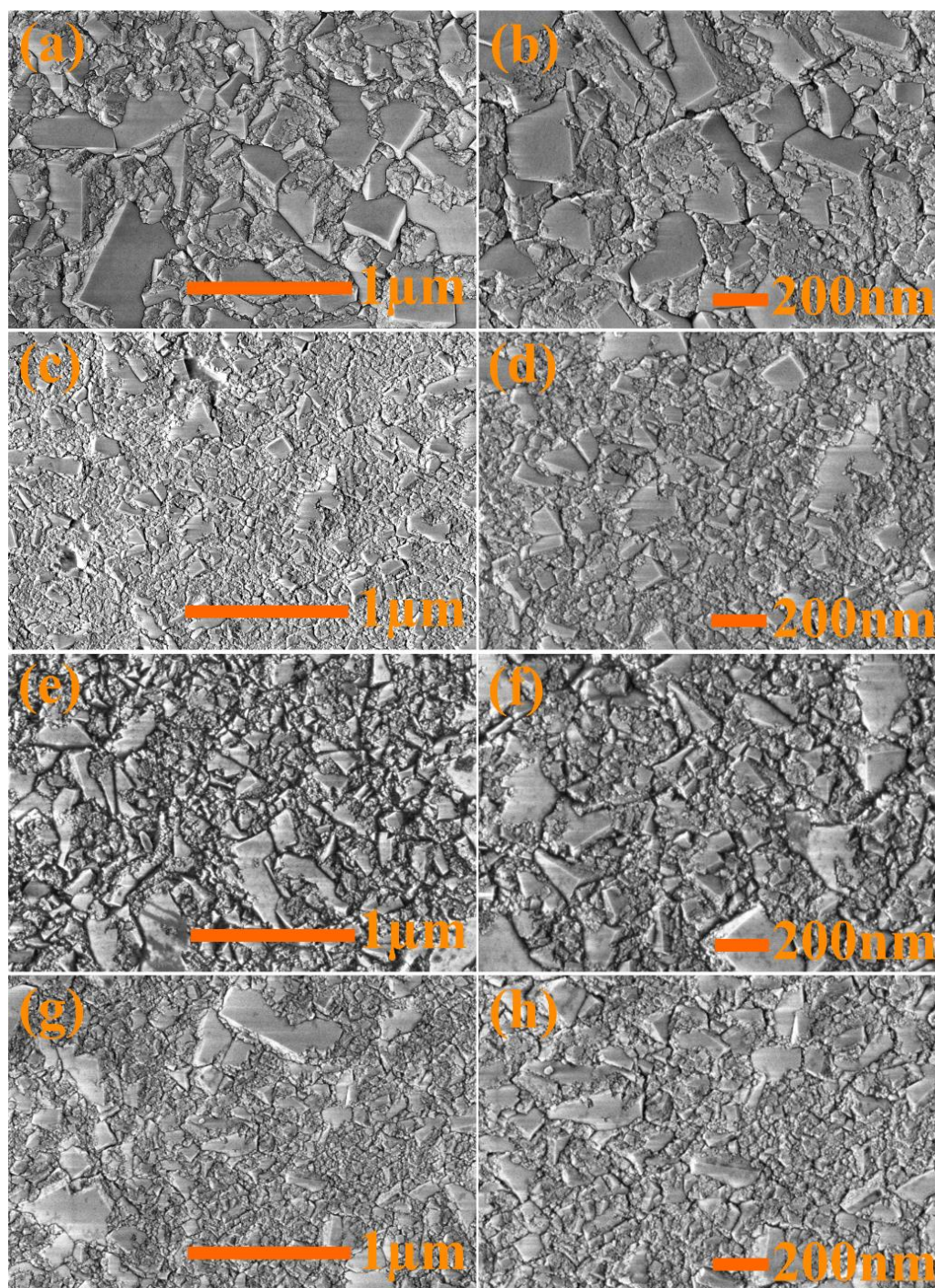


Figure 4.5 Low and high magnification plane view SE micrographs of (a), (b) NCD1; (c), (d) NCD1-100; (e), (f) NCD1-1000; and (g), (h) NCD1-2000 film surfaces after undergoing γ -irradiation.

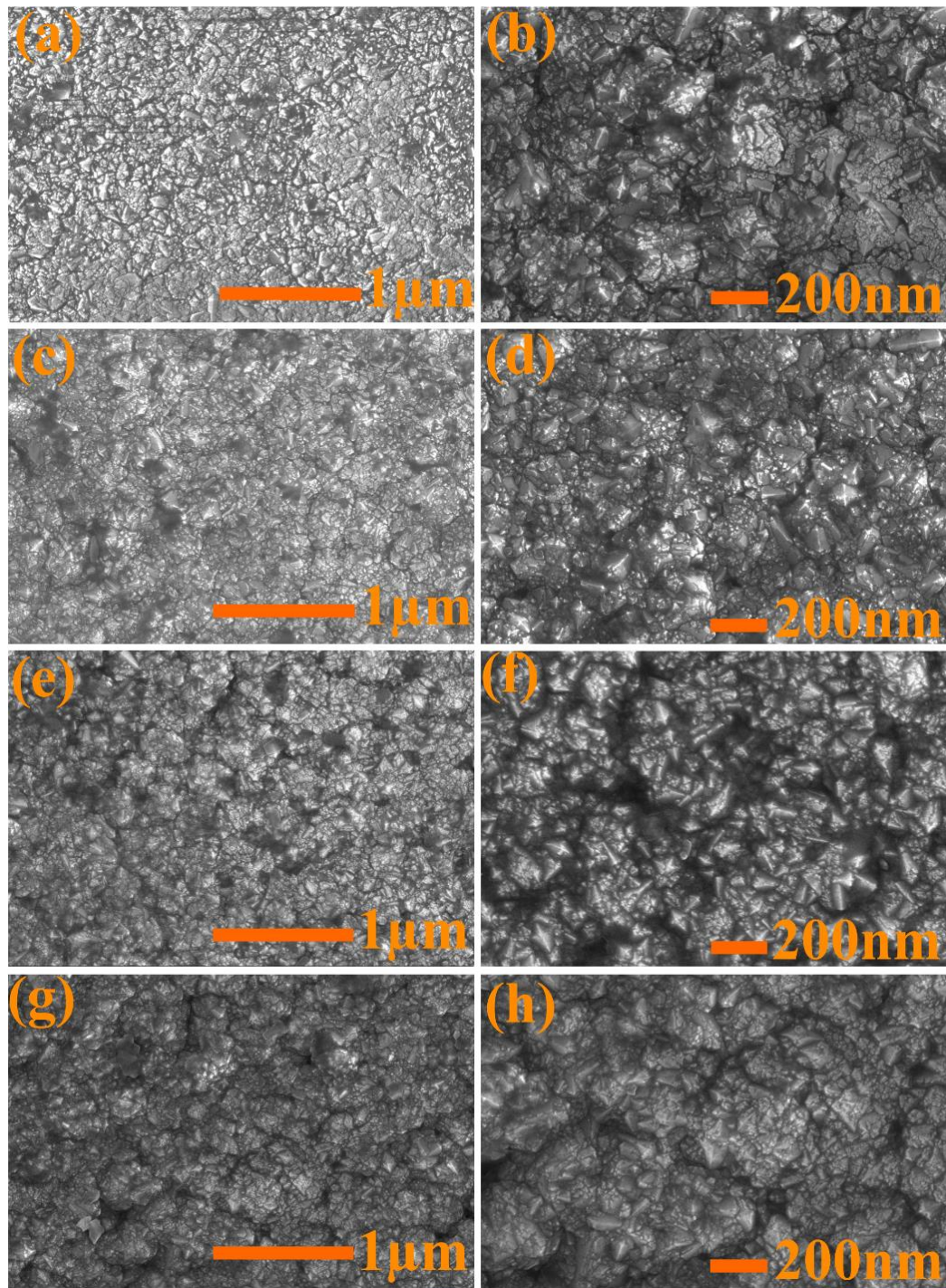


Figure 4.6 Low and high magnification of plane view SE micrographs of (a), (b) NCD2; (c), (d) NCD2-100; (e), (f) NCD2-1000; and (g), (h) NCD2-2000 film surfaces after undergoing γ -irradiation.

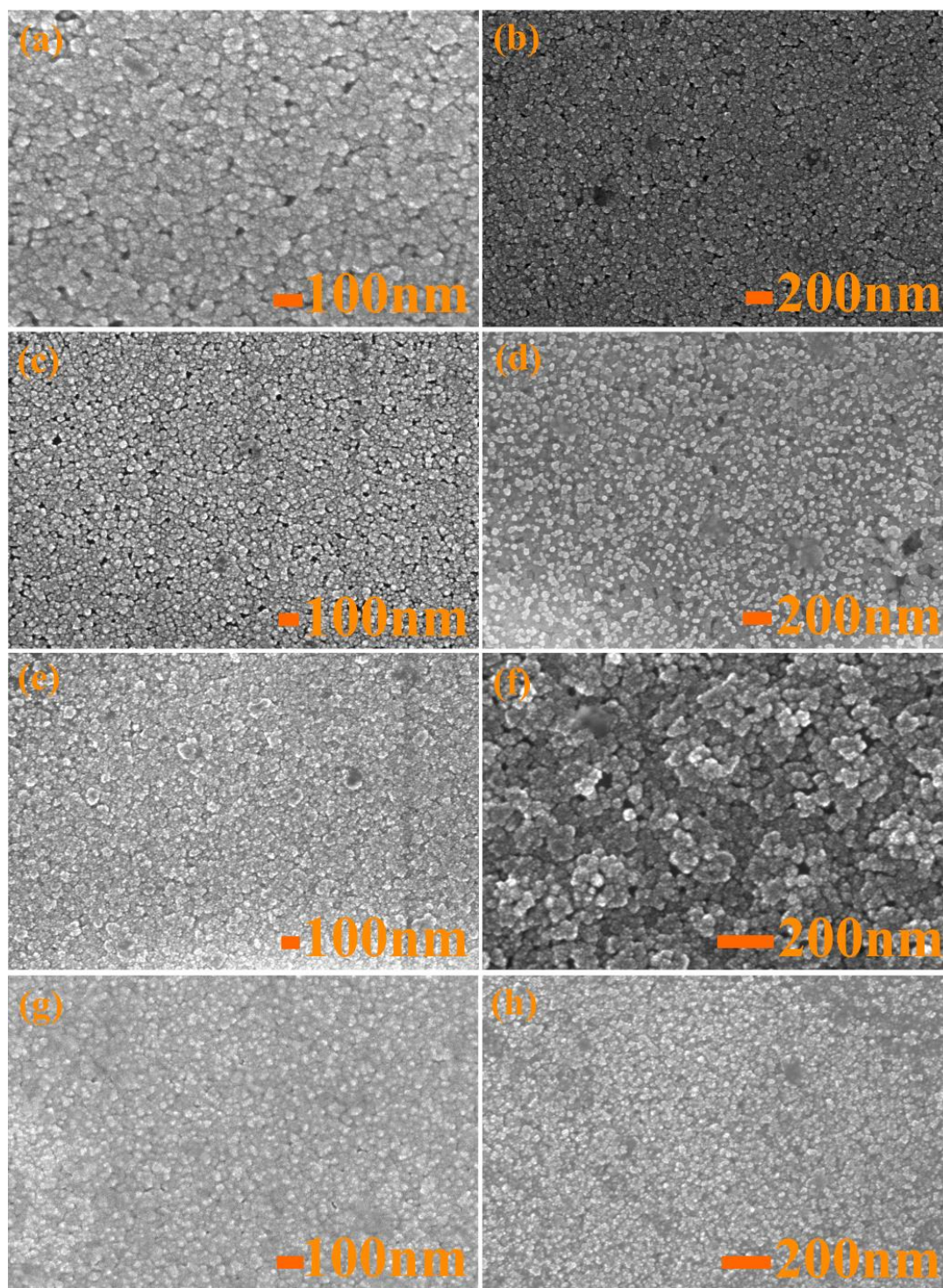


Figure 4.7 Low and high magnification of plane view SE micrographs of (a), (b) NCD3; (c), (d) NCD3-100; (e), (f) NCD3-1000; and (g), (h) NCD3-2000 film surfaces after undergoing γ -irradiation.

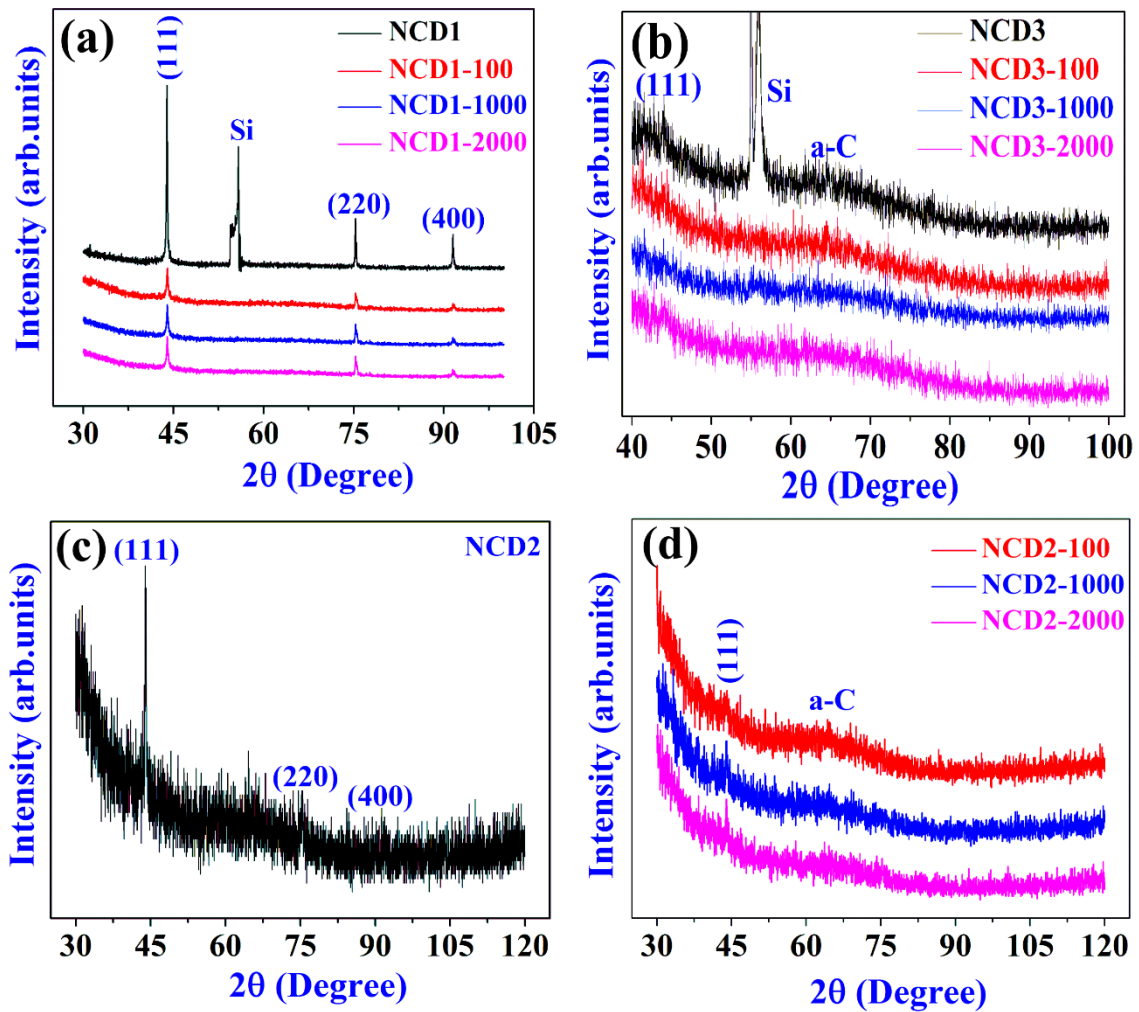


Figure 4.8 Grazing incidence X-ray diffractograms of γ -irradiated (a) NCD1, (b) NCD3 films along with the their pristine films; (c) pristine and (d) corresponding γ -irradiated NCD2 film.

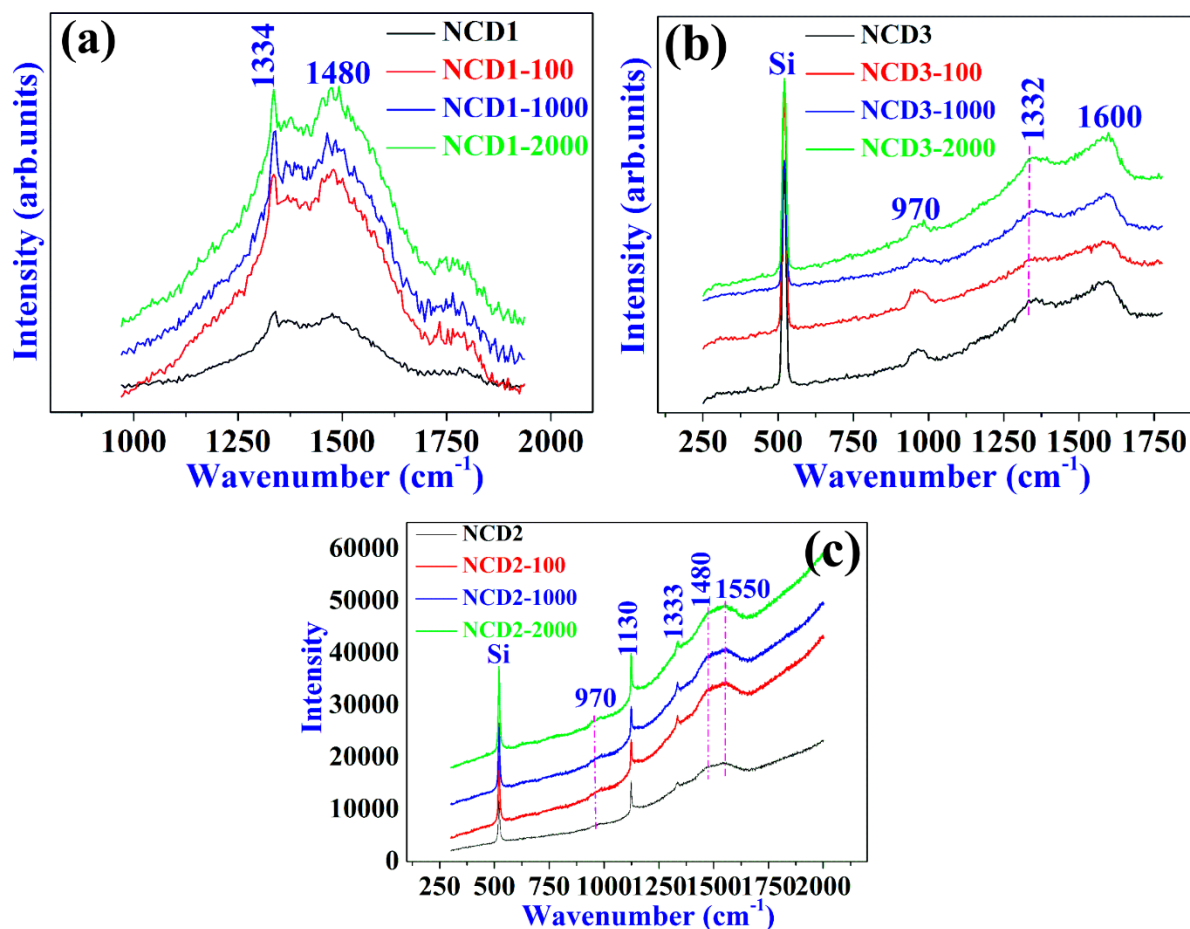


Figure 4.9 Raman spectra of γ -irradiated (a) NCD1, (b) NCD2 and (c) NCD3 films along with that of the as-deposited films.

4.2 Nitrogen Irradiated Diamond Thin Films

Plane view SE micrographs of 12 keV N^+ -ion irradiated NCD1 film with $1E16$ ions/cm² fluency (NCD1L-1E16) in comparison to the as-deposited NCD1's surface are shown in Fig. 4.10. The surface features of NCD1L-1E16 film (Fig 4.10 (c, d)) are more or less same as compared to the as-deposited NCD1 sample. GIXRD patterns (Fig. 4.11) and Raman spectra (Fig. 4.12) of 12 keV N^+ -ion irradiated NCD1 film in comparison to the as-deposited NCD1 film show miniscule changes indicating that the irradiation has effected the crystallinity and phase of the diamond film. In the case of GIXRD pattern the intensities of the diamond diffraction peaks have decreased indicating that the irradiation has reduced the crystalline quality of diamond. In the case of Raman spectrum, the Raman band centered at ~ 1427 cm⁻¹ could be resolved unlike in the case of NCD1. This observation indicates a change in the phase composition post-irradiation. In both NCD1 and NCD1L-1E16, the broad Raman band centered at ~ 1332 cm⁻¹ corresponds to zone-center phonons in diamond. The simultaneous

Results and Discussion

presence of the band at $\sim 1124\text{ cm}^{-1}$ and $\sim 1427\text{ cm}^{-1}$ is one of the characteristics of a nanocrystalline diamond thin film [22, 23]. G band in the case of NCD1L-1E16 appeared at $\sim 1530\text{ cm}^{-1}$ while it appeared at $\sim 1500\text{ cm}^{-1}$ in the case of NCD1. The Raman scattering observations indicate a definite change in the phase content of the film and/or formation of defects in the film post-irradiation. The Resonant Rutherford backscattering spectra (RRBS) (Fig. 4.13) showed the presence of carbon in pristine NCD1 and the presence of C and N in NCD1L-1E16 sample. The calculated 12 keV nitrogen ion beam implanted depth in NCD1 film is $\sim 30\text{ nm}$.

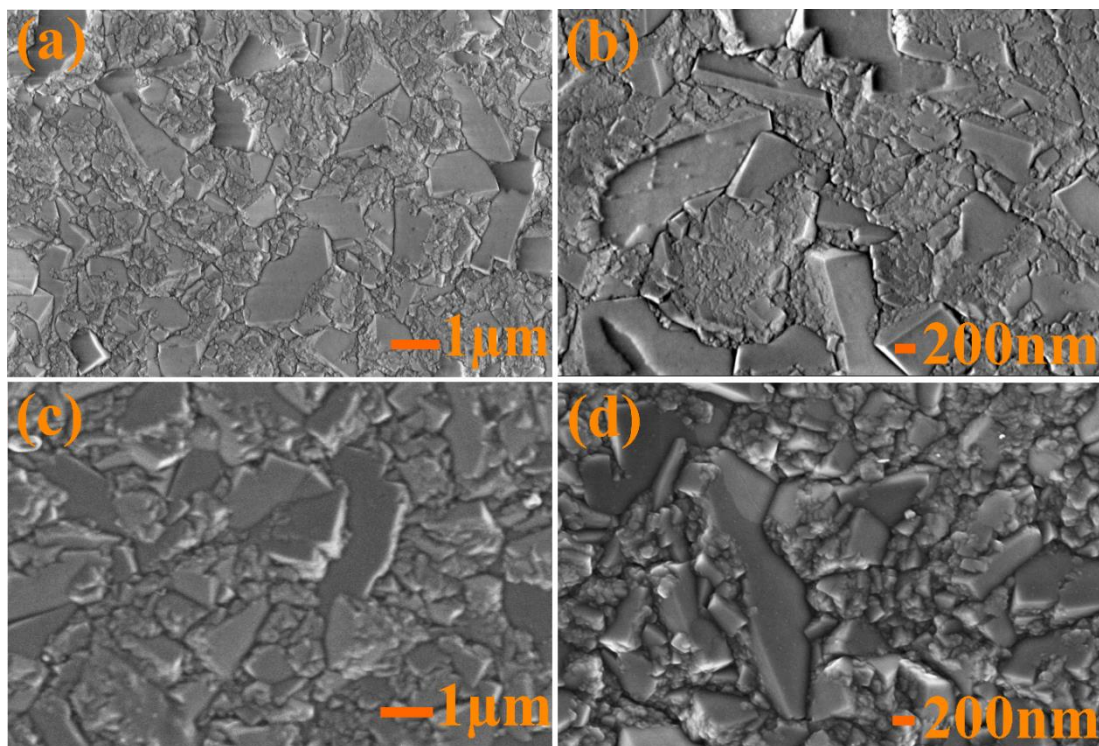


Figure 4.10 Low and high magnification of plane view SE micrographs of (a), (b) NCD1; (c), (d) NCD1L-1E16 film surfaces (after undergoing 12 keV N^+ ion irradiation).

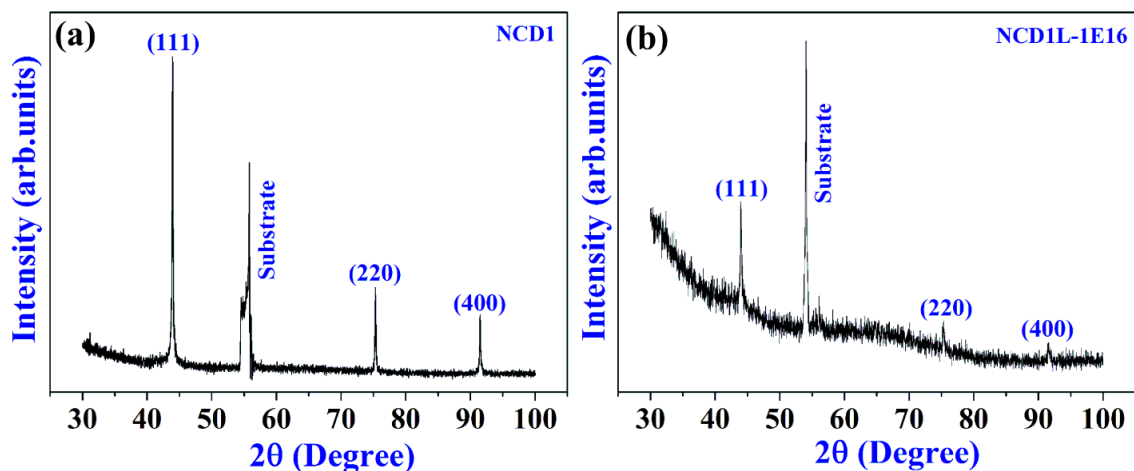


Figure 4.11 Grazing incidence X-ray diffractograms of (a) NCD1 film and (b) NCD1L-1E16 film (after 12 keV N^+ -ion).

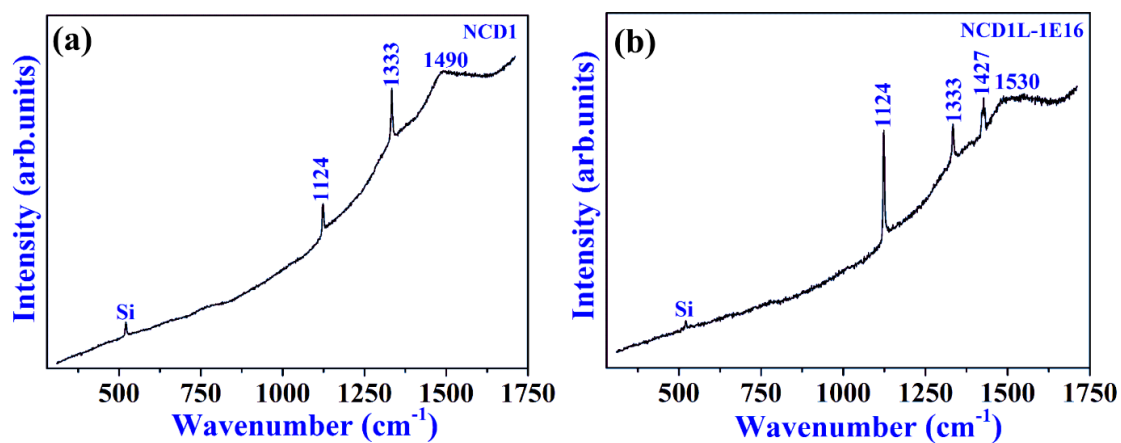


Figure 4.12 Raman scattering of (a) NCD1 film and (b) NCD1L-1E16 film (after 12 keV N^+ -ion irradiation).

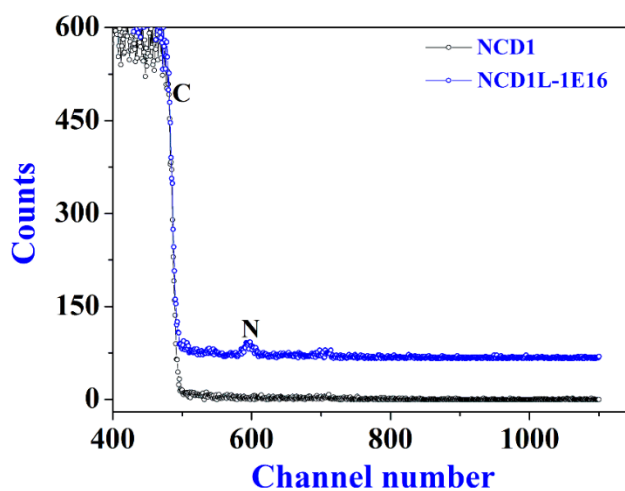


Figure 4.13 Rutherford back scattering spectra of (a) NCD1 film and (b) NCD1L-1E16 film (after 12 keV N^+ -ion irradiation).

Results and Discussion

HRTEM images of NCD1 and NCD1L-1E16 films are depicted in Fig. 4.14. Fig 4.14(a) shows diamond crystals, graphitic shells and amorphous carbon in NCD1. SAED pattern (inset of Fig 4.14(a)) is indicative of the polycrystalline nature of diamond in NCD1 correlating well with the GIXRD result for the same. Fig. 4.14 (b) depicts the branching and interconnection of the graphitic layers (indicated by circles). It shows that these carbon nanostructures are not perfectly spherical but spheroidal-like carbon onions [29, 30]. Moreover, these carbon nanoions (CNOs) have different shapes including elliptical, polyhedral, quasi spherical and deformed onions. A dimensional analysis of the CNOs was carried out by observing a large number of micrographs recorded for several CNOs present in NCD1 film. The obtained CNOs have multiple shells and each CNO contains 8-10 graphitic shells and maximum of 13. The inter-layer spacing of these layers is seen to be $\sim 0.3\text{--}0.4$ nm. In Fig. 4.14(a) and (b), the branching of the graphitic layers was observed at many places. Similar features are also observed in the case of NCD1L-1E16 film (Fig 4.14(d)) but are found to be defective in nature. In the case of NCD1L-1E16 film, SAED pattern clearly shows that post-irradiation, the film has been amorphousized to a great extent.

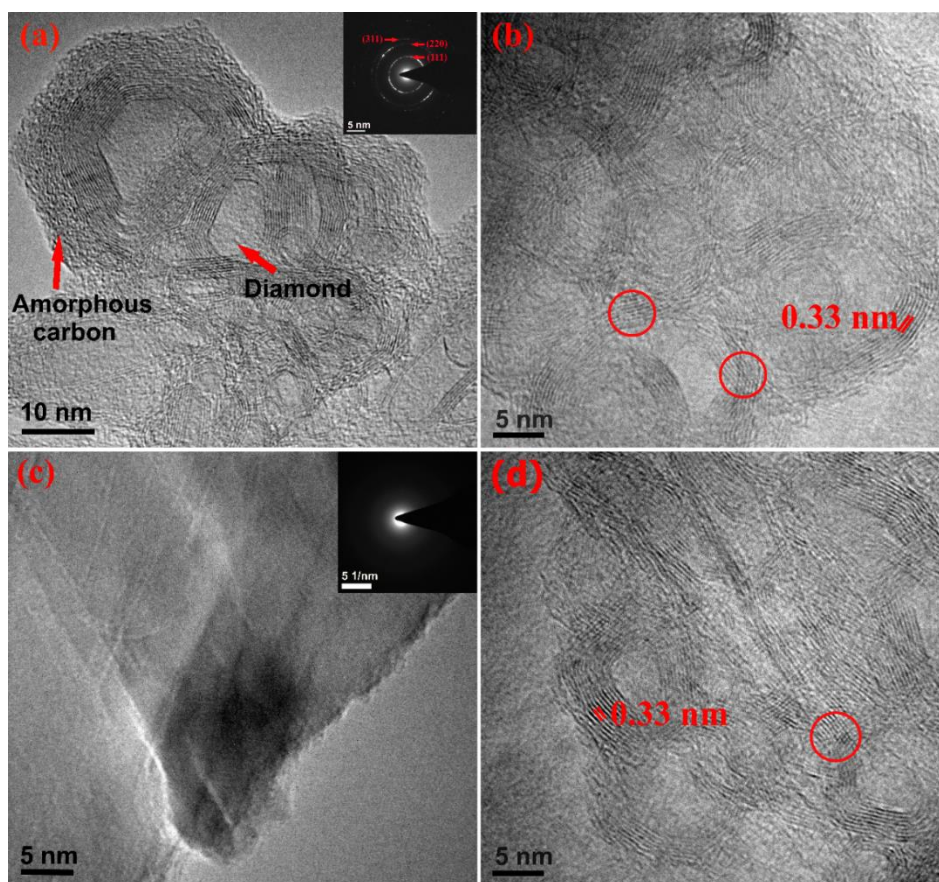


Figure 4.14 High resolution transmission electron micrographs of (a) (b) NCD1 film and (c), (d) NCD1L-1E16 film (after 12 keV N^+ -ion irradiation).

Results and Discussion

XRD patterns of as-deposited (named as NCD1) and 100 keV N⁺ ions' implanted diamond films are shown in Fig. 4.15. The reflections representing (111), (220) and (400) crystal planes in diamond are observed at $2\theta = \sim 45.9, \sim 75.2$ and $\sim 91.4^\circ$, respectively, in all the samples implying that the crystallinity of the diamond thin films after implantation is intact. Moreover, no other reflections corresponding to any other crystalline phase was observed post implantation implying that the implantation did not convert diamond into any new phase unlike in reference [31] which is an important work that is closely related to this part of the work. The diffraction peak broadening post implantation is negligible indicating that the implantation has not effected the grain size in the diamond films. Figure 4.16 shows the plane-view FESEM images, which clearly depict the typical randomly oriented (sub-micron and few tens of nm sized) diamond grains of the as-deposited and N⁺ ions' implanted diamond films. However, in the case of implanted samples, the grain edges appeared to be rounded-off most plausibly due to selective sputtering effect of the N⁺ ion beam on the grain boundary regions, which are mostly graphitic (sp² carbon) [32,33] in nature. To further understand the phase stability of diamond and presence of any other phases in small quantities, Raman spectra of as-deposited and implanted samples are recorded and shown in Fig. 4.17.

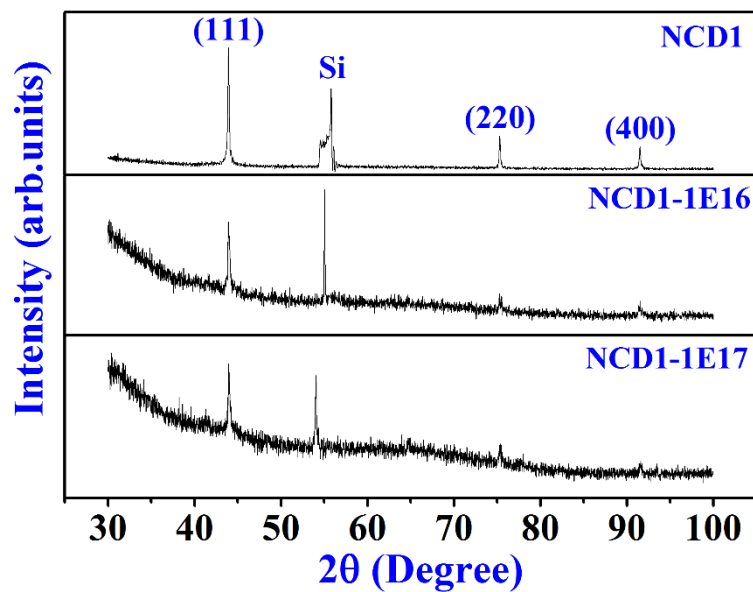


Figure 4.15 Glancing incidence X-ray diffractograms of (a) NCD1, (b) NCD1-1E16 and (c) NCD1-1E17. (b) and (c) after 100 keV N⁺-ions' implantation.

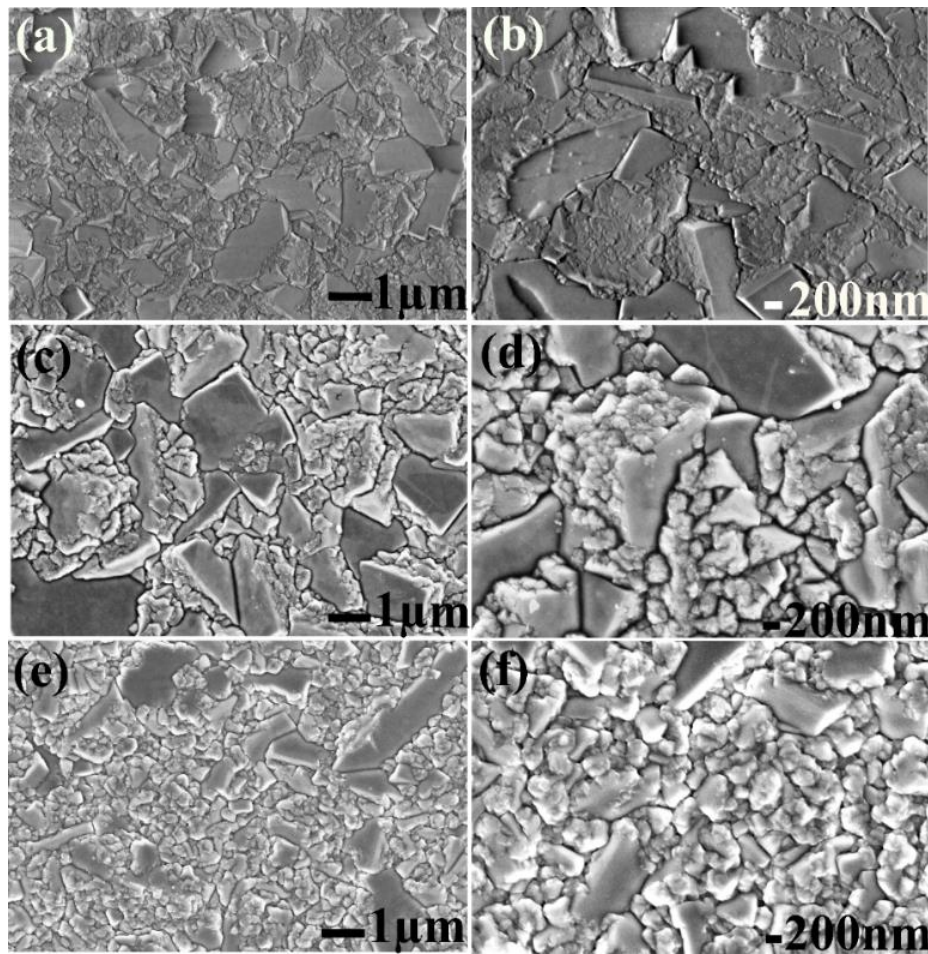


Figure 4.16. Plane-view FESEM images (at different magnifications) of (a, b) NCD1, (c, d) NCD-1E16 and (e, f) NCD-1E17. (c-f) are after 100 keV N^+ -ions' implantation.

As-deposited sample exhibits the characteristic zone center phonon in diamond at $\sim 1333 \text{ cm}^{-1}$ and graphitic band (G band, stretching mode of planar sp^2 C at the grain boundaries) at $\sim 1500 \text{ cm}^{-1}$, which are typical for MWCVD diamond films [33]. The spectra of implanted samples (Figs. 4.17 (b) and (c)) indicate a change in the bonding environment in the implanted films. The peak fitted spectra (the need of fitting if given in Reference [34]) are shown in Figs. 4.17 (d-f). It is noticed that bandwidth, position and relative intensity of diamond band, D band (1350 cm^{-1} , breathing mode of planar sp^2 C at the grain boundaries) and G band are different in NCD1, NCD1-1E16 and NCD1-1E17 indicating differences in phase content in these samples. Diamond, and D and G Raman bands in the case of implanted samples are slightly red-shift in comparison to that in NCD1 indicating that implantation has induced in-plane tensile stresses, and formation of sp^2 clusters and amorphous carbon in the diamond grain boundaries [34], respectively. It is important to note that the appearance of Raman spectra shown in Figs. 4.17 (b) and (c) is indicative of overlapping of spatially unresolved Raman bands in the considered spectral range. Moreover, carbon allotropes have different Raman

Results and Discussion

scattering cross-sections for the same incident laser (for instance, Raman scattering cross-section for graphite is far greater than that of diamond implying that the intensity of G band will be more intense than that of zone center phonon band of diamond even when graphitic content in the film is far less than that of diamond). Therefore by following careful curve fitting procedure [34], deconvolution of Raman spectra of NCD1, NCD1-1E16 and NCD1-1E17 samples in the spectral range 900-1800 cm^{-1} was carried out. The intensity ratios $\frac{I_G}{(I_G+I_{\text{Diamond}})}$ and $\frac{I_{\text{Diamond}}}{(I_{\text{Diamond}}+I_G)}$ which provide an insight on sp^2 C disorder and quality of films before and after implantation are calculated from the best fitted spectra. In Fig. 4.17(d), the peak at $\sim 1332 \text{ cm}^{-1}$ is assigned to sp^3 diamond bonding. The peaks at ~ 1360 and 1560 cm^{-1} correspond to D and G bands of sp^2 -bonded carbon, respectively. The D and G bands are accredited to breathing and stretching of planar carbon at the grain boundaries of diamond films. The peaks at 1135 and 1485 cm^{-1} correspond to C-H in plane bonding and C=C stretch of trans-polyacetylene (t-pa), respectively. The peak around $\sim 1210 \text{ cm}^{-1}$ is generally considered in the case of large amount of disorder in the diamond films. The peak around $\sim 1320 \text{ cm}^{-1}$ (F_{2g} mode) is attributed to the presence of sp^3 diamond bonding with long range order and considered to obtain the best fit. The fitted Raman data for NCD-1E16 film is shown in Fig. 3(e). It shows a peak around $\sim 1325 \text{ cm}^{-1}$ which is the signature of carbon bonded in the diamond configuration (F_{2g}). The peaks at 1185 and 1470 cm^{-1} are the signature of C-H in plane bonding and t-pa, respectively. The peaks around ~ 1350 and 1546 cm^{-1} are D band and G band respectively. All of these peaks (Fig. 4.17(f)) are also observed in NCD1-1E17 film. Different Raman band observations are tabulated in Table 4.1. It is very clear from the table that graphitization increased due to implantation. When a fast moving ion travels through a solid it loses energy due to inelastic interaction with the electrons. When an incoming ion moves with low energy, it interacts with atomic system through elastic collisions and transfers its energy (kinetic) through nuclear energy loss process. This energy transfer causes the atom to displace from its position and further collides with nearby atoms further resulting in cascade collision of atoms inside the target. The collision cascade breaks the atomic bonds and results in sharp rise of local temperature which is supported through Thermal Spike Model. It is expected that a similar thermal spike might have formed in ion irradiated diamond films, and as a consequence graphitic content is formed in the implanted films.

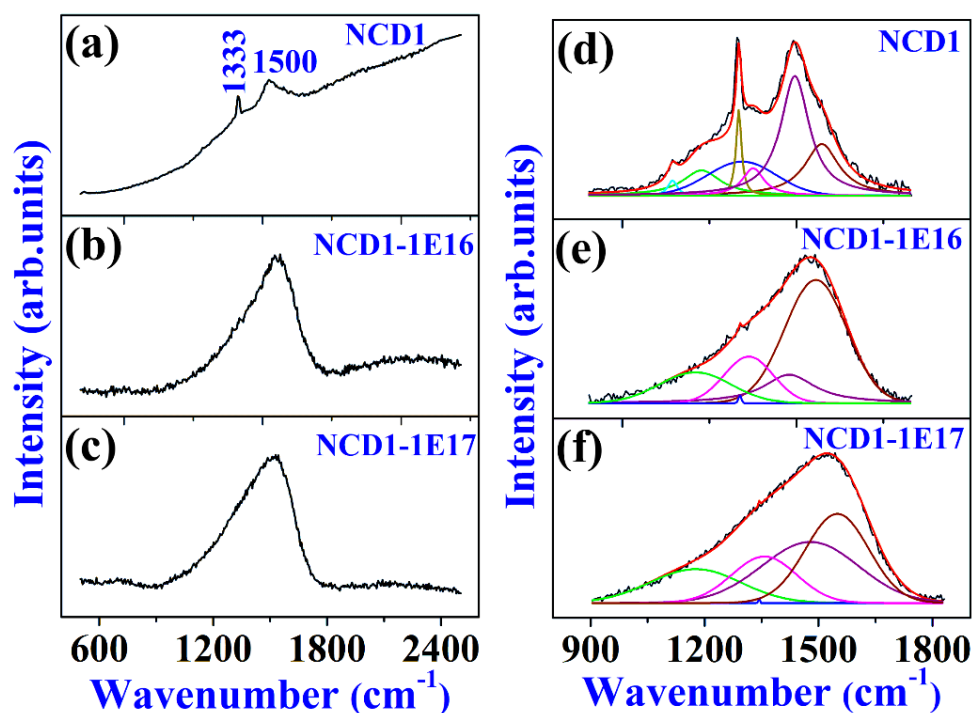


Figure 4.17 Raman spectra of (a) NCD1, (b) NCD1-1E16 and (c) NCD1-1E17 and the corresponding best fitted spectra in (d), (e) and (f), respectively.

Table 4.1 Fitted parameters of Raman data for pristine and nitrogen implanted NCD1 films with different fluences.

| Sample | Diamond Peak (cm ⁻¹) | D band (cm ⁻¹) | G band (cm ⁻¹) | FWHM diamond (cm ⁻¹) | Intensity Ratios | |
|-----------|----------------------------------|----------------------------|----------------------------|----------------------------------|--|--|
| | | | | | $\frac{I_{\text{Diamond}}}{(I_{\text{Diamond}} + I_{\text{G}})}$ | $\frac{I_{\text{G}}}{(I_{\text{G}} + I_{\text{Diamond}})}$ |
| NCD1 | 1332 | 1360 | 1560 | 232 | 0.4 | 0.6 |
| NCD1-1E16 | 1326 | 1350 | 1545 | 8.6 | 0.07 | 0.94 |
| NCD1-1E17 | 1330 | 1345 | 1540 | 3 | 0.04 | 0.97 |

RBS spectra of all the samples are shown in Fig. 4.18. In the case of NCD1-1E16 and NCD1-1E17, both C and N peaks are observed in the corresponding RBS spectra. The width of N peak is ~75 nm which is close to the calculated (Stopping and Range of Ions in Matter (SRIM) software based) depth of 88 nm for N atoms in diamond. The combined effect of induced graphitization along the diamond grain boundaries and N atom incorporation is expected to greatly enhance the electrical conductivity [35].

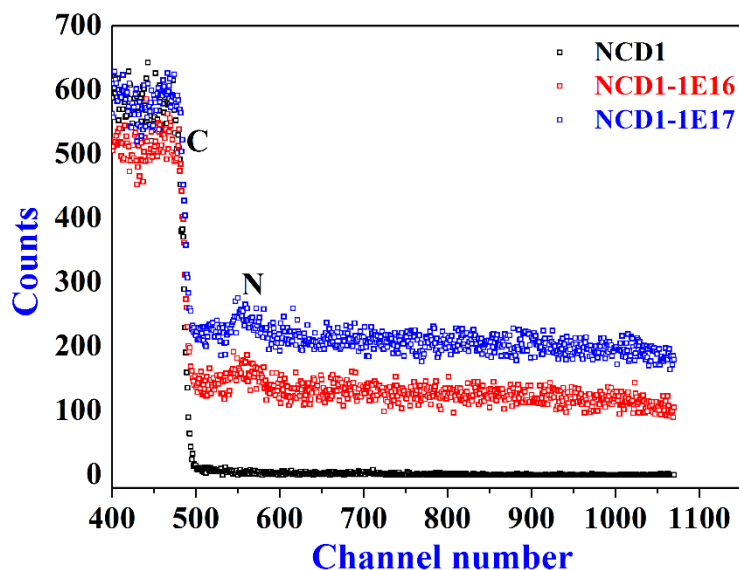


Figure 4.18 RBS spectra of NCD1-1E16 and NCD1-1E17 in comparison to NCD1.

As-expected, the I-V characteristics (Fig. 4.19) of NCD-1E16 and NCD-1E17 in comparison to NCD clearly indicate a considerable increase in the electrical conductivity in them. At 5 V, the current values in NCD, NCD-1E16 and NCD-1E17 are 4.4 nA, 3 μ A and 140 μ A, respectively.

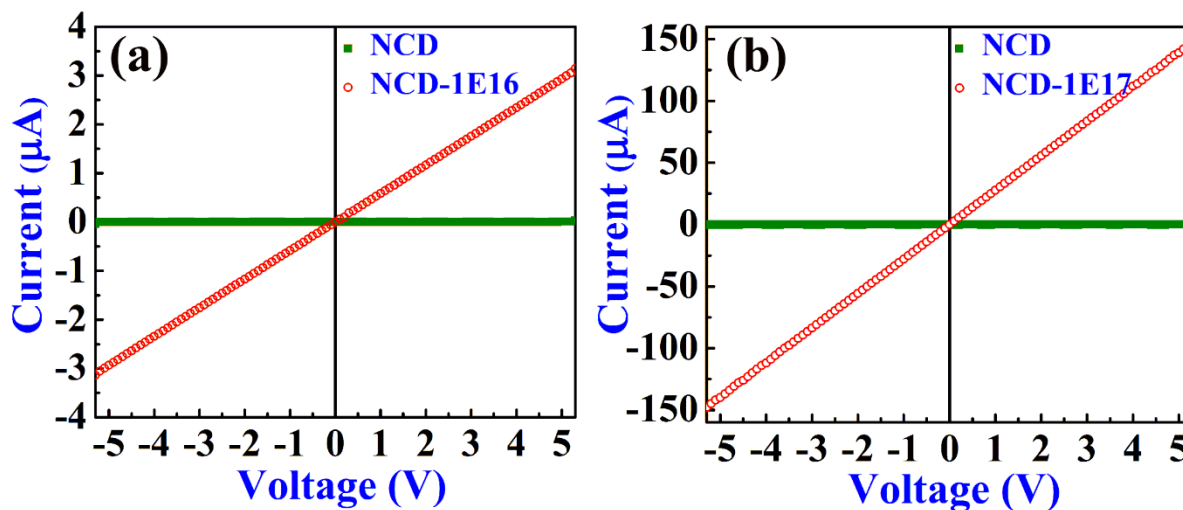


Figure 4.19 I-V characteristics of NCD1-1E16 and NCD1-1E17 in comparison to NCD1. In the figure please read NCD as NCD1.

The above results clearly show that the polycrystalline diamond thin films can be made suitable for the fabrication of robust metal-insulator-semiconductor (here conductive diamond/diamond/Si) type devices when the near-surface regions of diamond films that are deposited on doped Si substrates are made electrically conductivity.

Results and Discussion

Further N^+ -ion beam irradiation energy on NCD1 films has been increased to 70 MeV. These films are irradiated with fluences $1E12$ and $1E13$ ions/cm² are named as NCD1-1E12 and NCD1-1E13, respectively. Figure 4.20 shows the plane-view FESEM images of NCD1-1E12 and NCD1-1E13 in comparison with NCD1 clearly depict the typical randomly oriented diamond grains of the N^+ ions' implanted diamond films. Like in the previous case of 100 keV irradiation, in this case of implanted samples also the grain edges appeared to be rounded-off. Moreover, typical charging effects (small dark spot-like features in the micrographs) are observed. This effect is more in the case of $1E13$ ions/cm².

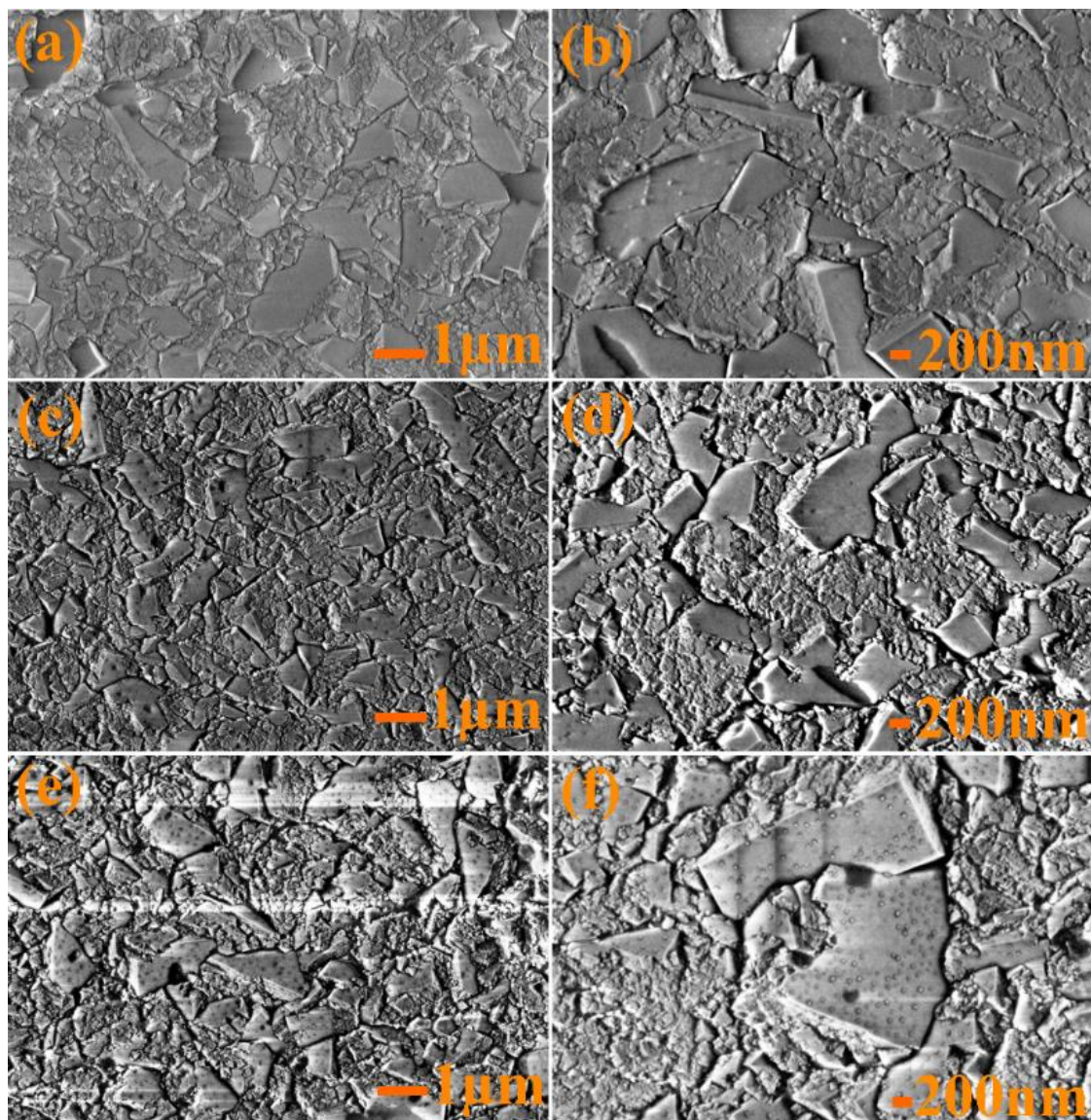


Figure 4.20 Low and high magnification of plane view SE micrographs of (a), (b) NCD1; (c), (d) NCD1-1E12; and (e), (f) NCD1-1E13 films (after 70 MeV N^+ -irradiation).

Results and Discussion

GIXRD patterns of NCD1, NCD1-1E12 and NCD1-1E13 are shown in Fig. 4.21. The reflections representing (111), (220) and (400) crystal planes in diamond are recorded at $2\theta = \sim 45.9, \sim 75.2$ and $\sim 91.4^\circ$, respectively, in all the samples implying that the crystallinity of the diamond thin films after implantation is intact. However, the back ground noise in the case of NCD1-1E12 and NCD1-1E13 films are high as compared to NCD1 film which is attributed to the decrease of diamond phase purity. Raman spectra (Fig. 4.22) of NCD1-1E12 and ND1-1E13 samples showed two broad peaks at ~ 1333 and 1500 cm^{-1} which are attributed to zone-center phonon band in diamond and graphitic (G) band, which are similar to NCD1's case.

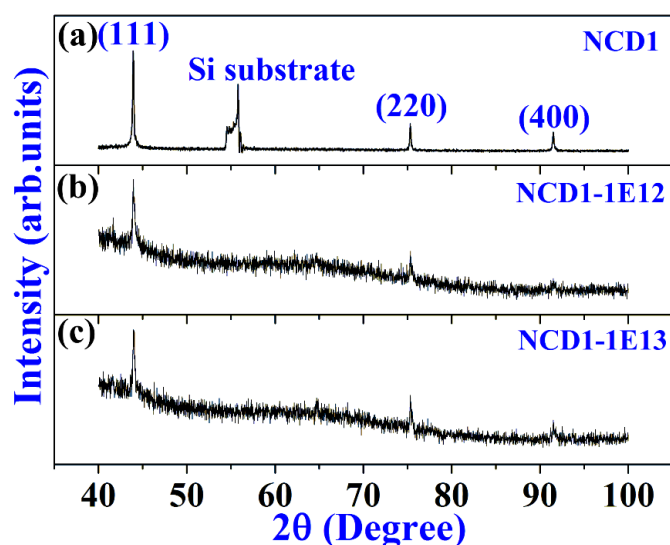


Figure 4.21 GIXRD patterns of (a) NCD1, (b) NCD1-1E12 and (c) NCD1-1E13 films.

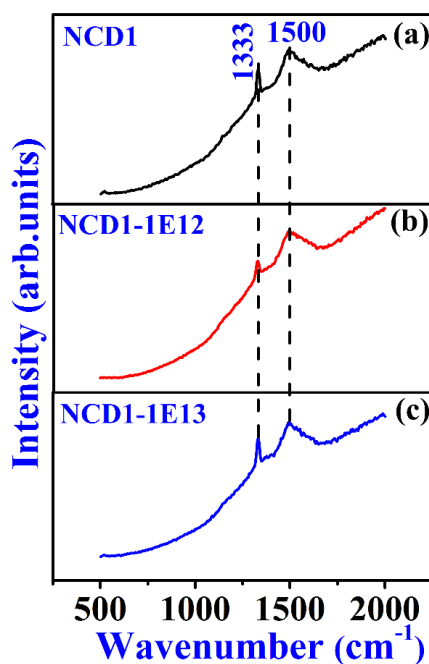


Figure 4.22 Raman spectra of (a) NCD1, (b) NCD1-1E12, (c) NCD1-1E13 films.

Results and Discussion

The NCD2 and NCD3 films are also irradiated with 12 keV N^+ -ion beam. The plane view SE micrographs of as-deposited and 12 keV N^+ -irradiated NCD2 (NCD2L-1E16) and NCD3 (NCD3L-1E16) films with $1E16$ ions/cm² fluence are shown in Fig. 4.23. After the nitrogen ion irradiation surface features of NCD2 film are rounded off, which is shown in Fig. 4.23 (b). The similar kind of surface modifications are noticed in the case of NCD3L-1E16 film shown in Fig. 4.23 (d). The X-ray diffractograms of NCD2L-1E16 and NCD3L-1E16 (Fig. 4.24) did not show any obvious changes in comparison to NCD2 and NCD3, respectively.

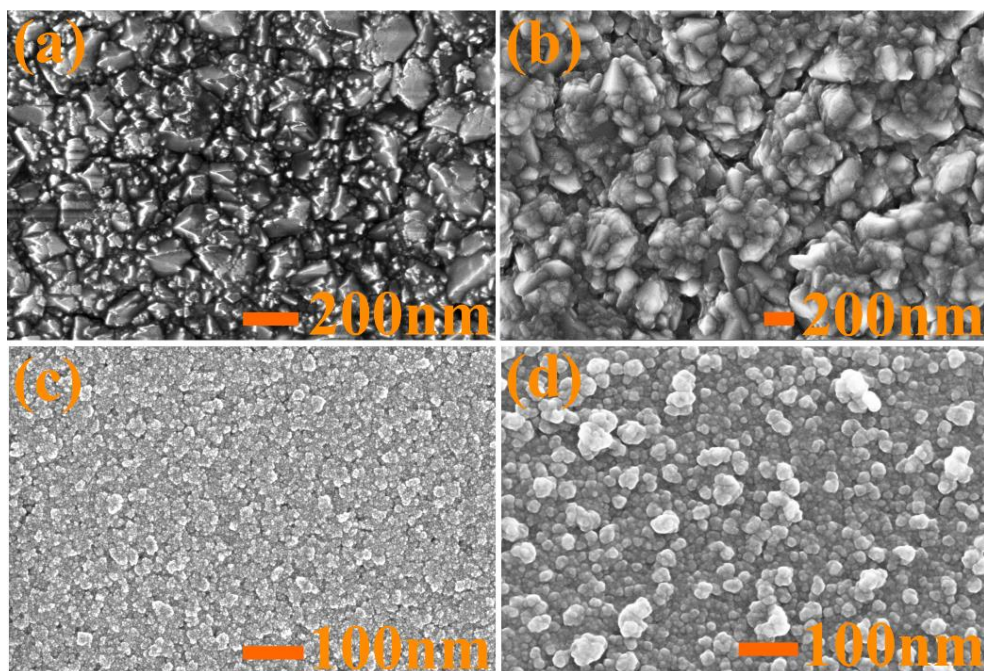


Figure 4.23 Low and high magnification of plane view SE micrographs of (a) NCD2, (b) NCD2L-1E16, (c) NCD3 and (d) NCD3L-1E16 film surfaces.

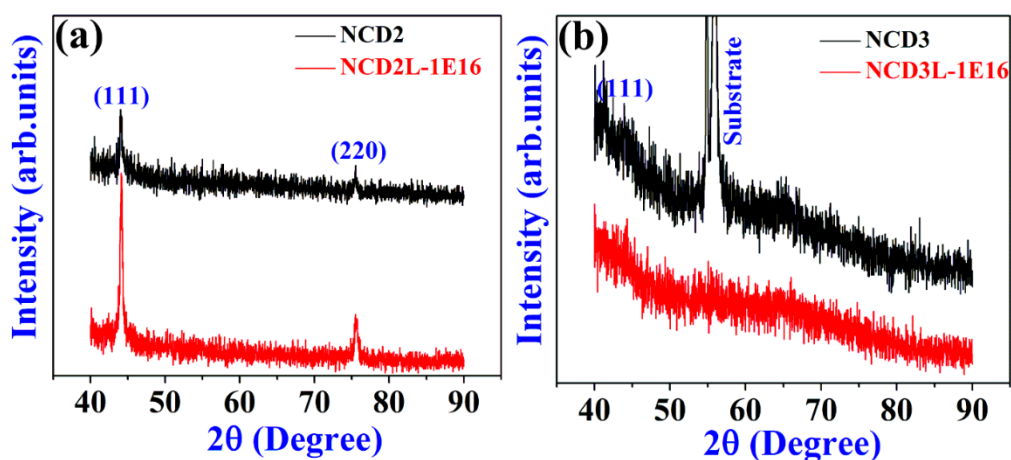


Figure 4.24 GIXRD patterns of (a) NCD2 and NCD2L-1E16 and (b) NCD3 and NCD3L-1E16.

Results and Discussion

Raman spectra of NCD2L-1E16 and NCD3L-1E16 (Fig. 4.25) did not show any obvious changes in comparison to NCD2 and NCD3, respectively.

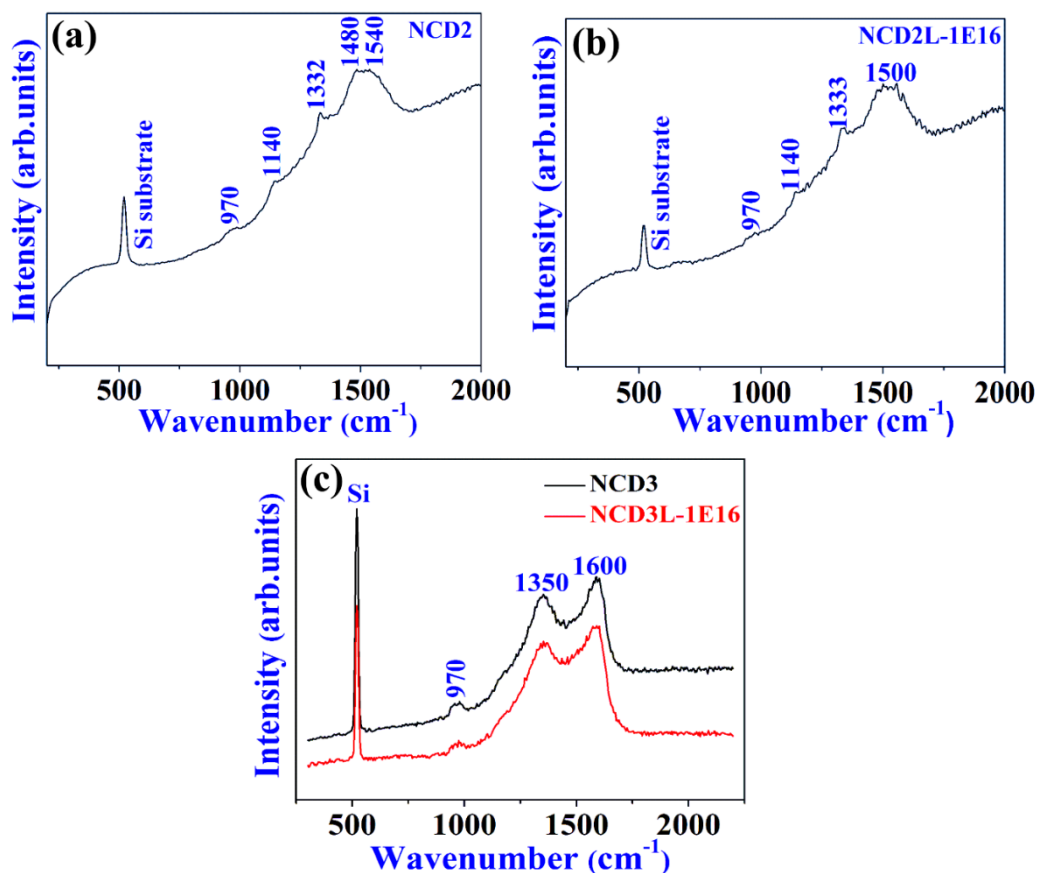


Figure 4.25 Raman spectra of (a) NCD2 and NCD2L-1E16 and (b) NCD3 and NCD3L-1E16.

N^+ -ion beam irradiation energy on NCD2 and NCD3 films is increased to 100 keV. The irradiation fluence on these films was 1×10^{16} and 1×10^{17} ions/cm² respectively. The 100 keV N^+ -implanted NCD2 and NCD3 films with 1E16 and 1E17 ions/cm² fluencies are named as NCD2-1E16, NCD2-1E17, NCD3-1E16 and NCD3-1E17, respectively. The surface morphology of NCD2-1E16 and NCD2-1E17 are shown in Fig. 4.26. The surface features of N^+ -irradiated films are rounded off as compared to NCD2 film. The same kind of surface features are observed in NCD3-1E16 and NCD3-1E17 films shown in Fig. 4.27 (c, d, e, f). The X-ray diffractograms of NCD2-1E16 and NCD2-1E17 shown in Fig 4.28 (b, c) are similar to those of NCD2 and NCD3. After the 100 keV N^+ -irradiation on NCD2 and NCD3 films, surface of these films get amorphised. To understand the effect of ion energy and dose on structural modifications and bonding configurations of carbon atoms resulting from N^+ -ion implantation, Raman spectra were deeply studied. Raman spectra of NCD2-1E16 and NCD2-1E17 films showed broad peak at 1530 cm⁻¹ shown in Fig. 4.29 (b, c) which assigned to G

Results and Discussion

band. The NCD2-1E16 showed a vibrational mode at 245 cm^{-1} which is assigned to radial breathing mode (RBM) in diamond nanocrystals [36]. Raman spectra of NCD3-1E16 and NCD3-1E17 films (shown in Fig. 4.30 (b, c)) showed a single broad peak at $\sim 1560\text{ cm}^{-1}$ which is assigned to G band comes from graphite present at grain boundaries and surface. The amorphisation of the NCD2 and NCD3 films after irradiation is also confirmed from XRD results.

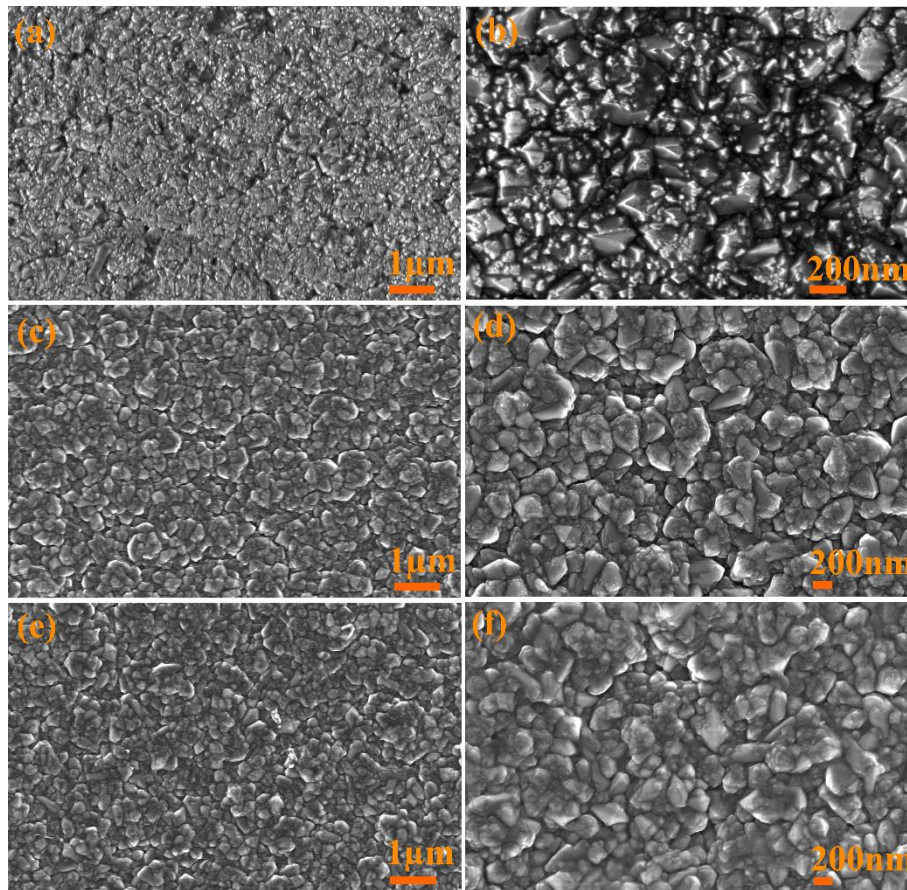


Figure 4.26 Low and high magnification of plane view SE micrographs of (a), (b) NCD2; (c), (d) NCD2-1E16; and (e), (f) NCD2-1E17 film surfaces (after 100 keV N^+ -irradiation).

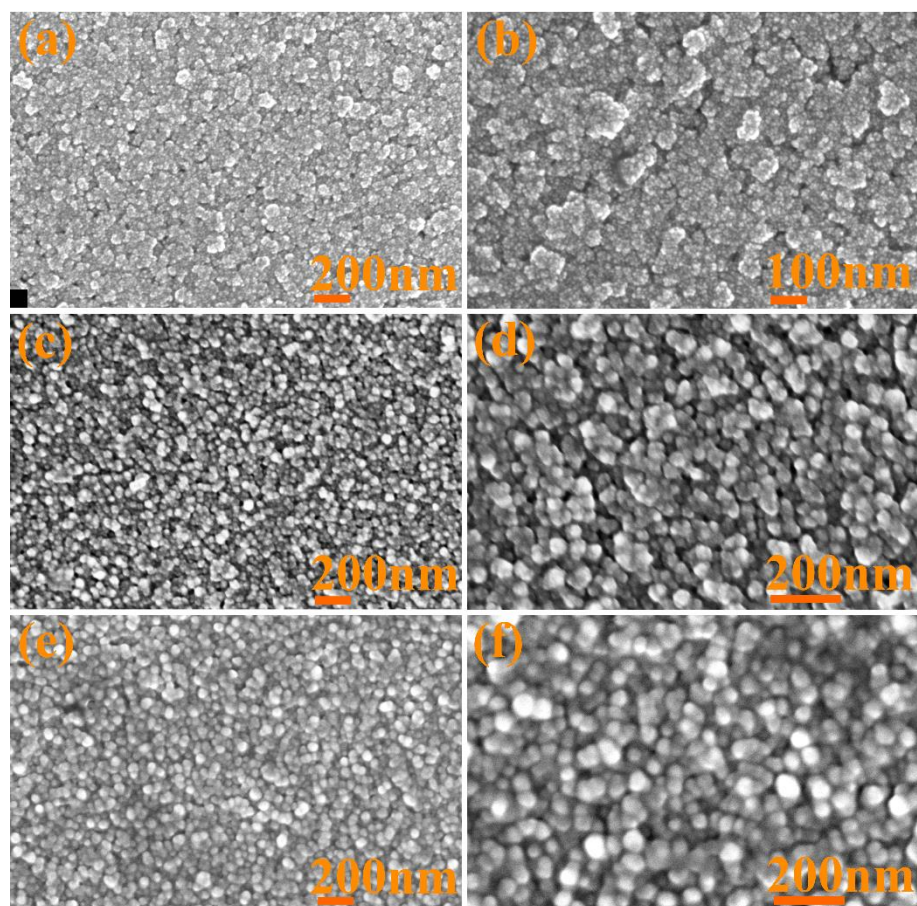


Figure 4.27 Low and high magnification of plane view SE micrographs of (a), (b) NCD3; (c), (d) NCD3-1E16; and (e), (f) NCD3-1E17 film surfaces (after 100 keV N^+ -irradiation).

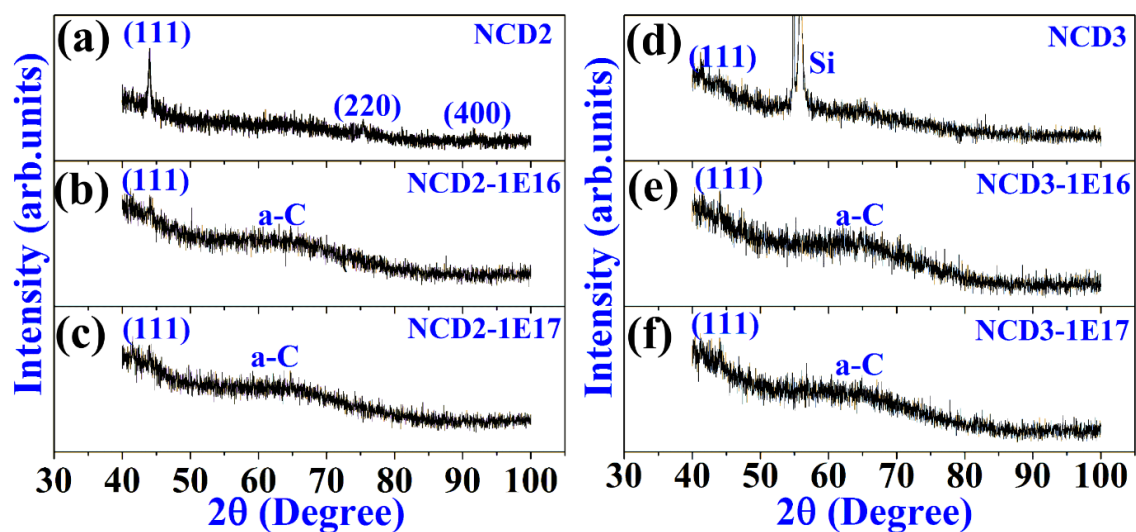


Figure 4.28 Grazing incidence X-ray diffractograms of (a) NCD2, (b) NCD2-1E16, (c) NCD2-1E17, (d) NCD3, (e) NCD3-1E16 and (f) NCD3-1E17 films.

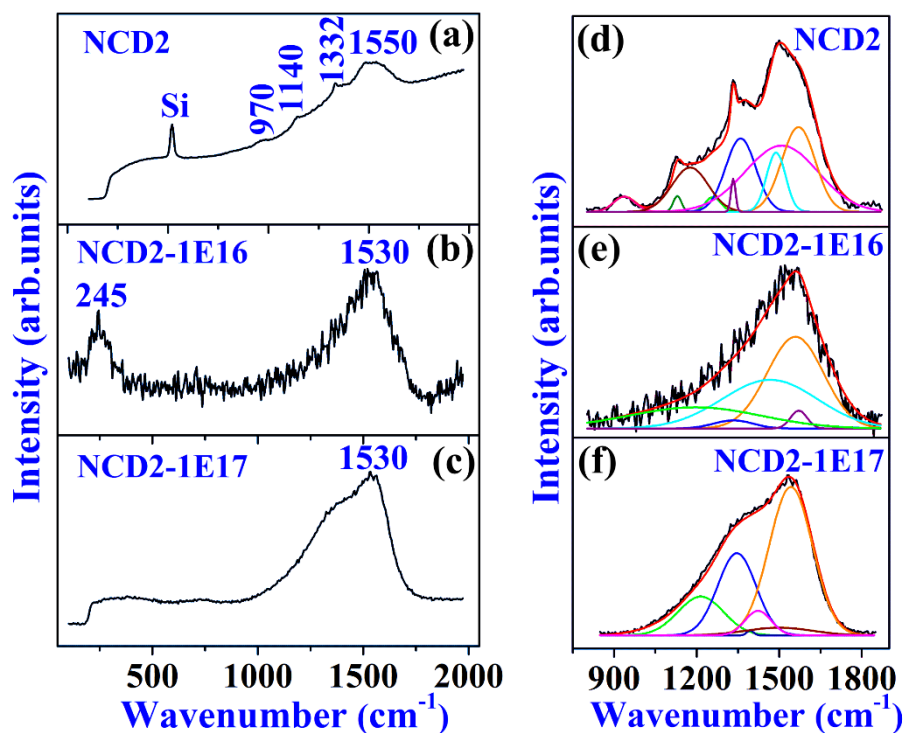


Figure 4.29 Raman spectra of (a) NCD2; (b) NCD2-1E16, (c) NCD2-1E17 films after 100 keV N^+ -ion irradiation and (d), (e) and (f) are the corresponding peak fitted Raman spectra.

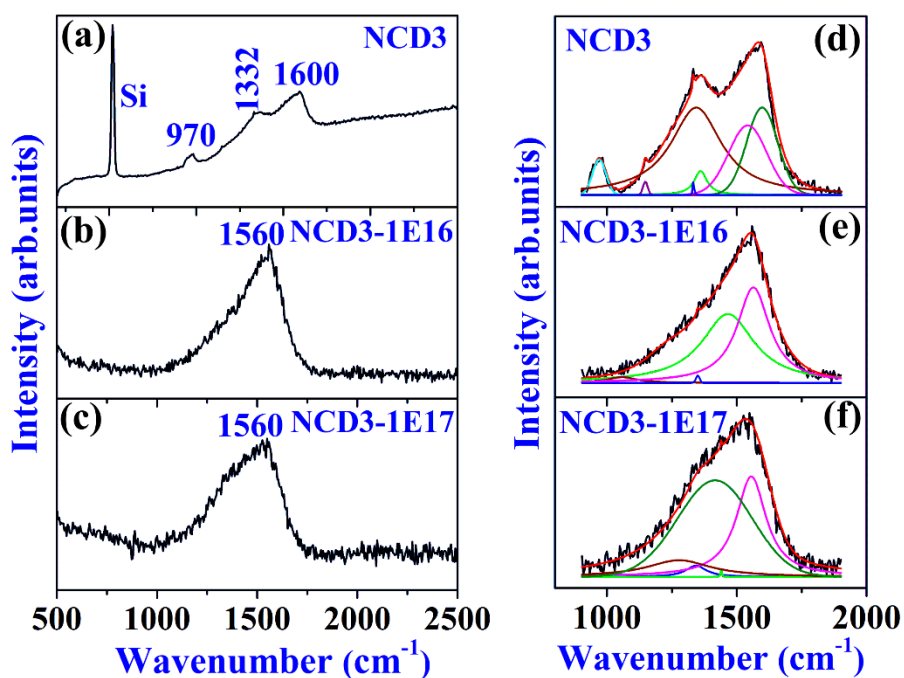


Figure 4.30 Raman spectra of (a) NCD3; (b) NCD3-1E16, (c) NCD3-1E17 films after 100 keV N^+ -ion irradiation and (d), (e) and (f) are the corresponding peak fitted Raman spectra.

Results and Discussion

The deconvolution of Raman spectra of NCD2, NCD2-1E16, NCD2-1E17 and NCD3, NCD3-1E16, NCD3-1E17 samples were done in the range of 900-1800 cm^{-1} is shown Fig. 4.29 (d-f) and Fig. 4.30 (d-f). The careful curve fitting procedure has been carried out to estimate the intensity ratios of $\frac{I_G}{(I_G+I_{\text{Diamond}})}$ and $\frac{I_{\text{Diamond}}}{(I_{\text{Diamond}}+I_G)}$ thereby to estimate the sp^2 -C binding and quality of diamond films before and after implantation process. From Fig. 4.29 (d) for NCD2, the fitted peaks are observed at ~ 970 , ~ 1140 , ~ 1177 , ~ 1252 , ~ 1320 , ~ 1345 , ~ 1480 and ~ 1540 cm^{-1} . For NCD3 (Fig. 4.30 (d)), the fitted peaks are at ~ 970 , ~ 1140 , 1330 , 1345 , 1530 and 1590 cm^{-1} . The peak at ~ 970 cm^{-1} corresponds to 2nd order phonon mode of silicon, which is emerging from the silicon substrate. A small shoulder-like feature at ~ 1140 cm^{-1} accompanied with band at 1480 cm^{-1} are assigned to trans-polyacetylene segments present at grain boundaries and surfaces. The peak at 1320 cm^{-1} in NCD2 is assigned to diamond. The vibrational density of states (VDOS) of diamond is dominated by contributions from X points (1175 cm^{-1}), resulting broad features around 1200 cm^{-1} . The phonon wave vectors from vibrational domains in density of states lead to a broad peak most notably at ~ 1250 cm^{-1} which is corresponding to nanodiamond [37]. The fitted bands at 1345 and 1530 - 1600 cm^{-1} are assigned to D and G bands respectively. The peak at 1330 cm^{-1} in NCD3 film is from sp^3 diamond. The diamond peak broadening of NCD3 (FWHM ~ 276 cm^{-1}) more as compared to NCD2 (FWHM ~ 18 cm^{-1}) which indicates smaller crystallite size in NCD3 as compared to NCD2 which also accompanies with XRD results. For NCD2-1E16 and NCD2-1E17 films (shown in Fig. 4.29 (e, f)), the fitted peaks at ~ 1200 and 1332 cm^{-1} are assigned to the diamond peak. It is observed from the fitting that, the intensity of diamond peak decreased as well as broadening (FWHM) of 1332 cm^{-1} diamond peak increased. For NCD2-1E16 broadening (FWHM ~ 157 cm^{-1}) is less as compared to NCD2-1E17 (~ 163 cm^{-1}) which indicates smaller diamond grain size in case of NCD2-1E17 as compared to NCD2-1E16. These results complement well with the XRD results discussed earlier. For NCD2-1E16 sample, the broad peak at ~ 1460 cm^{-1} is from t-PA and band at ~ 1550 cm^{-1} is assigned to G band. For NCD2-1E17 sample, broad peaks at ~ 1480 and 1530 cm^{-1} are assigned to t-pa and G band respectively. The estimated intensity ratios $\frac{I_{\text{Diamond}}}{(I_{\text{Diamond}}+I_G)}$ of NCD2 NCD2-1E16 and NCD2-1E17 films are 0.28, 0.07 and 0.06 respectively. For NCD3-1E16 and NCD3-1E17 films, the fitted peaks are observed at ~ 1200 and 1332 cm^{-1} are assigned to the diamond peak. The peak at ~ 1450 cm^{-1} is assigned to t-pa and the broad 'G' band is observed. The diamond peak intensity is decreased as well as FWHM increased from 13 cm^{-1} to 94 cm^{-1} and the corresponding crystallite size decreases for NCD3-1E16 and NCD3-1E17, respectively. This implies that presence of

Results and Discussion

diamond grains amount and size of diamond grains on surface has been decreased (see SEM Fig. 4.27 (d, f)). The increase in intensity of ‘G’ band in all 100 keV N⁺-ion implanted diamond films confirms the graphitization has been taken place by ion implantation process. The estimated intensity ratio $\frac{I_{\text{Diamond}}}{(I_{\text{Diamond}}+I_{\text{G}})}$ values pertaining to NCD3, NCD3-1E16 and NCD3-1E17 film surfaces are ~ 0.25, 0.1 and 0.08 respectively. From the peak fitting of Raman spectra clearly indicates that all diamond films (NCD1, NCD2 and NCD3) after 100 keV N⁺- ion implantation has induced graphitization in the present study. The Resonant RBS spectra of 100 keV implanted NCD2 and NCD3 films are shown in Figure 4.31 (a) and (b) respectively. The implanted nitrogen ion depth into NCD2 and NCD3 films are 45 and 60 nm respectively.

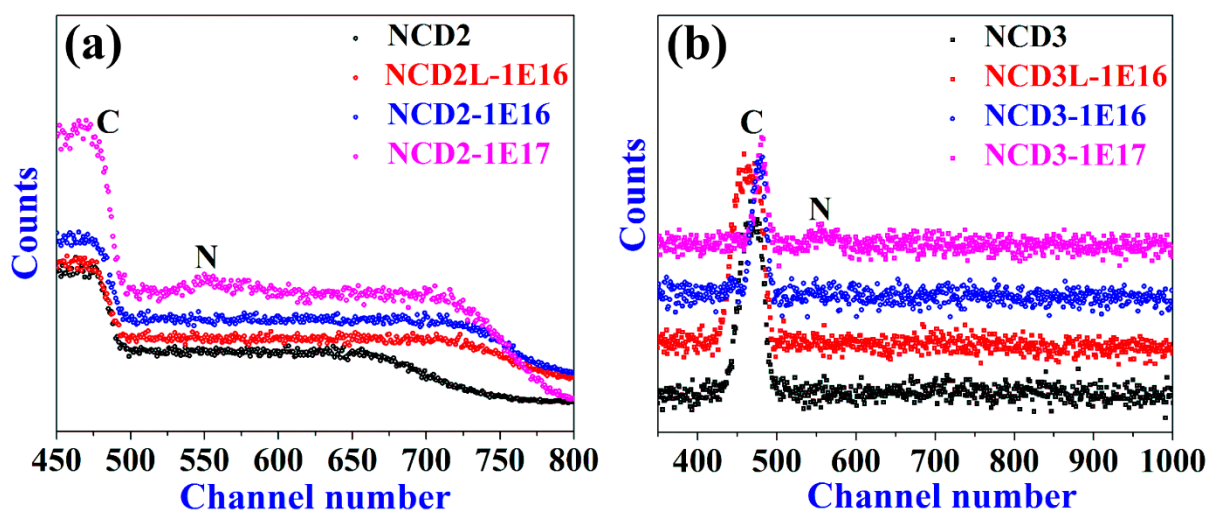


Figure 4.31 Resonant Rutherford back scattering spectra of (a) NCD2 and (b) NCD3 film before and after 100 keV N⁺-ion irradiation.

Further N⁺ - ion beam irradiation energy on NCD2 and NCD3 films has been increased to 70 MeV. These films are irradiated with 1E12 and 1E13 ions/cm² fluence are named as NCD2-1E12, NCD2-1E13, NCD3-1E12 and NCD3-1E13 respectively. Obtained surface morphology (secondary electron micrographs) of NCD2, NCD2-1E12 and NCD2-1E13 films are shown in Fig. 4.32. The surface features of NCD2-1E12 and NCD2-1E13 (shown in Fig. 4.32 (c, d) and (e, f)) are randomly oriented with different grain size of diamonds. SE micrographs of NCD3, NCD3-1E12 and NCD3-1E13 films are shown in Fig. 4.33. The surface features of irradiated NCD3 film showed granular clusters. The X-ray diffractograms attributed from irradiated NCD2 and NCD3 films are shown in Fig. 4.34 (b, c and e, f). The NCD2-1E12, NCD2-1E13, NCD3-1E12 and NCD3-1E13 samples are observed (111) diffraction peak at $2\theta = 43.9^\circ$ and amorphous carbon band at $\sim 64^\circ$ respectively. Raman spectra for NCD2-1E12 and NCD2-1E13 samples showed two broad peaks at ~ 1332 and 1550 cm^{-1} are attributed to diamond and

Results and Discussion

graphitic (G) band (shown in Fig. 4.35 (b), (c)) along with other bands which are similar to NCD2 sample (shown in Fig. 4.35 (a)). Also, Raman spectra for NCD3-1E12 and NCD3-1E13 samples showed two broad peaks at ~ 1332 and 1600 cm^{-1} are attributed to diamond and graphitic (G) band (shown in Fig. 4.35 (e), (f)) along with 2nd order Si band at $\sim 970\text{ cm}^{-1}$ which are similar to NCD3 sample (shown in Fig. 4.35 (d)).

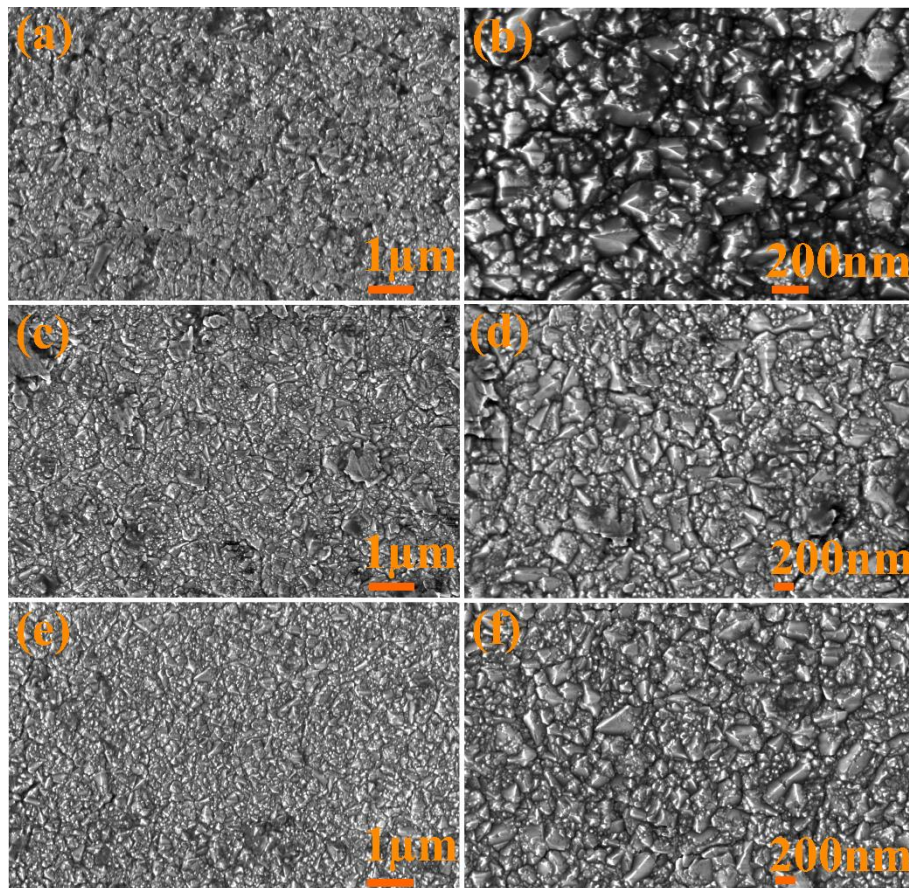


Figure 4.32 Low and high magnification of plane view SE micrographs of (a), (b) NCD2; (c), (d) NCD2-1E12; and (e), (f) NCD2-1E13 film surfaces after 70 MeV N⁺-irradiation.

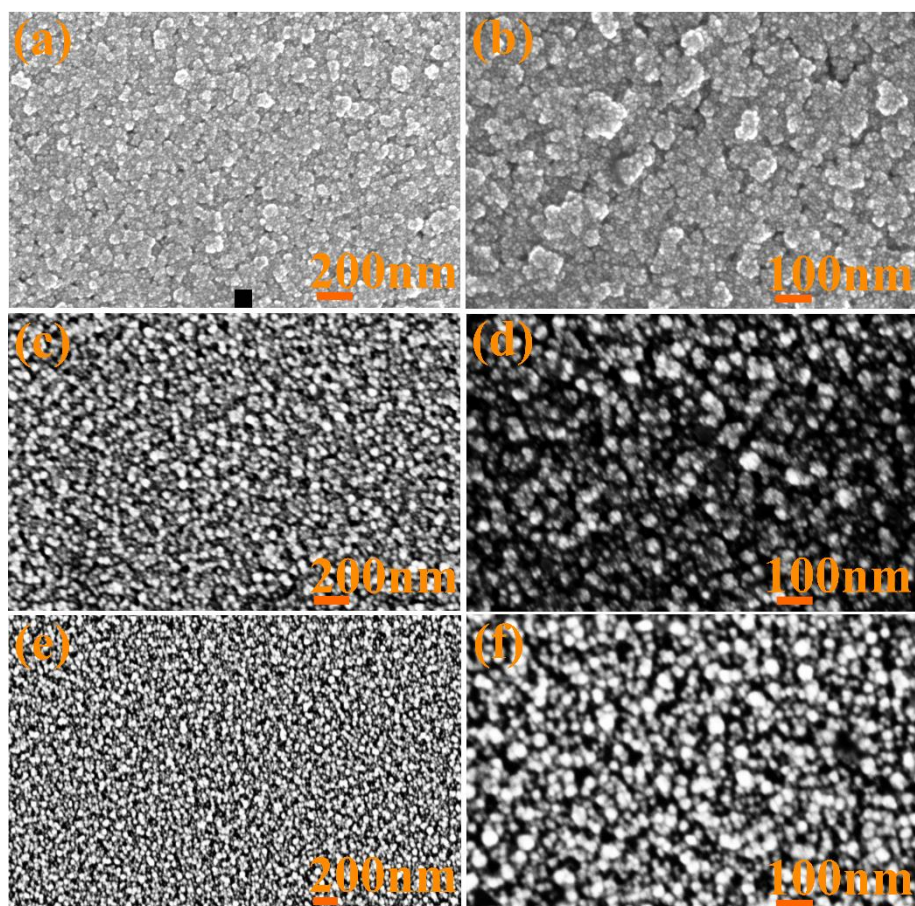


Figure 4.33 Low and high magnification of plane view SE micrographs of (a), (b) NCD3; (c), (d) NCD3-1E12; and (e), (f) NCD3-1E13 film surfaces after 70 MeV N^+ -irradiation.

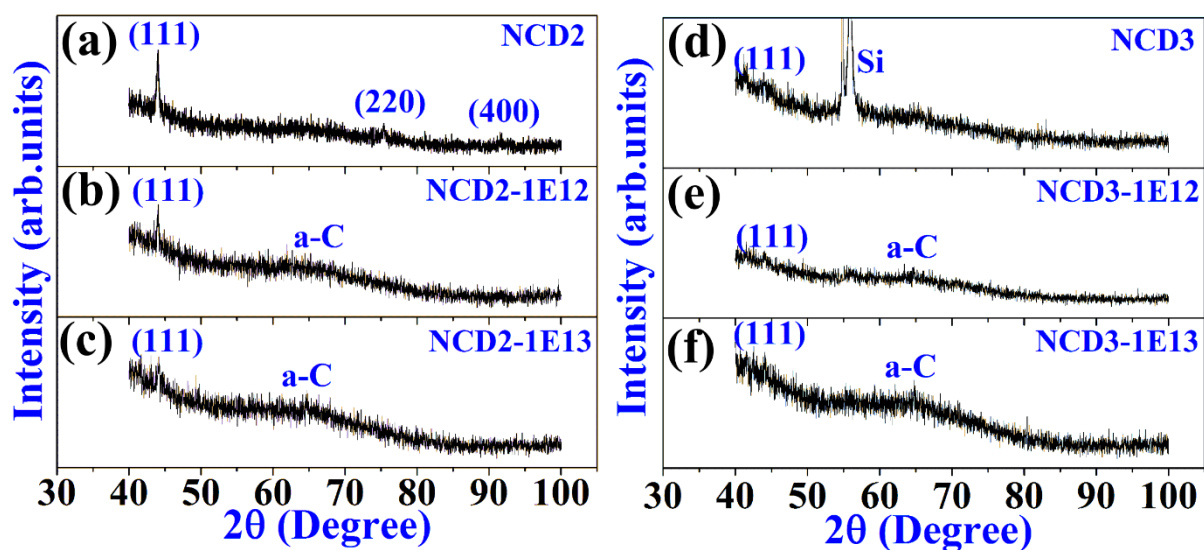


Figure 4.34 Glancing angle X-ray diffractograms of (a) NCD2, (b) NCD2-1E12, (c) NCD2-1E13 (d) NCD3, (e) NCD3-1E12 and (f) NCD3-1E13 films.

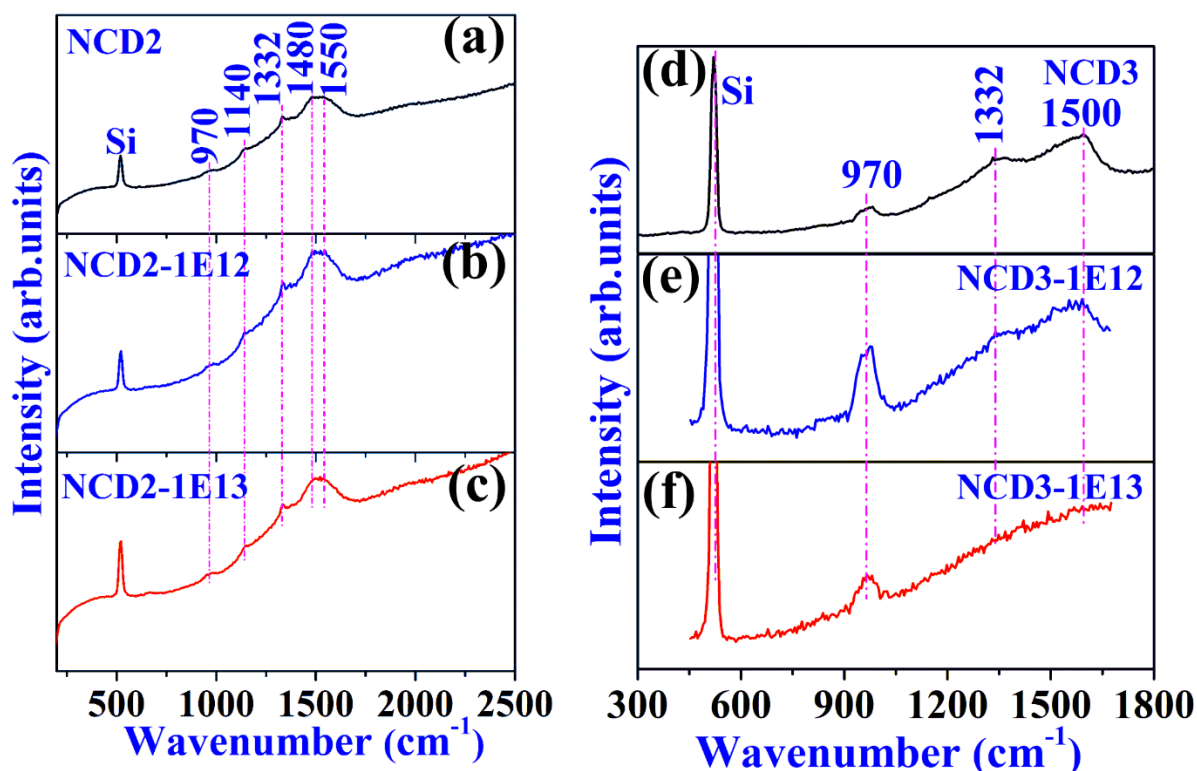


Figure 4.35 Raman spectra of (a) NCD1; (b) NCD1-1E12, (c) NCD1-1E13 films (after 70 MeV N^+ -ion irradiation).

4.3 Indentation Behavior of Diamond and Diamond/ β -SiC Thin Films

SEM micrographs of the indented impressions on various films grown on manually treated W are shown in Fig. 4.36. For a 30 kgf (294 N) load, no noticeable delamination events could be observed; however, the central region of the indentation impression presented continuous and equally spaced circumferential cracks. Lateral cracks with small lengths could be observed upon the application of the next higher load. When an indentation load of 60 kgf (600 N) was used, short and irregular cracks are nucleated on the periphery of the indentation zone. The central region of the indentation zone still maintained continuous and equally spaced circumferential cracks. It is observed that with an increase in the load, not only the circumferential crack number increases but also crater diameter increases. It is also observed that with an increase in the load, the lateral crack number as well as its length increases. When the normal load has been increased to 125 kgf, the stress field produced a discernible delamination in the case of pure diamond film. In the case of diamond/ β -SiC nanocomposite films delamination and/or rupture events did not occur up to a load of 125 kgf; for loads equal and/or greater than 60 kgf the result is a crater having a certain diameter with emanating lateral cracks of certain length. The films remained attached to the substrate unlike the diamond films.

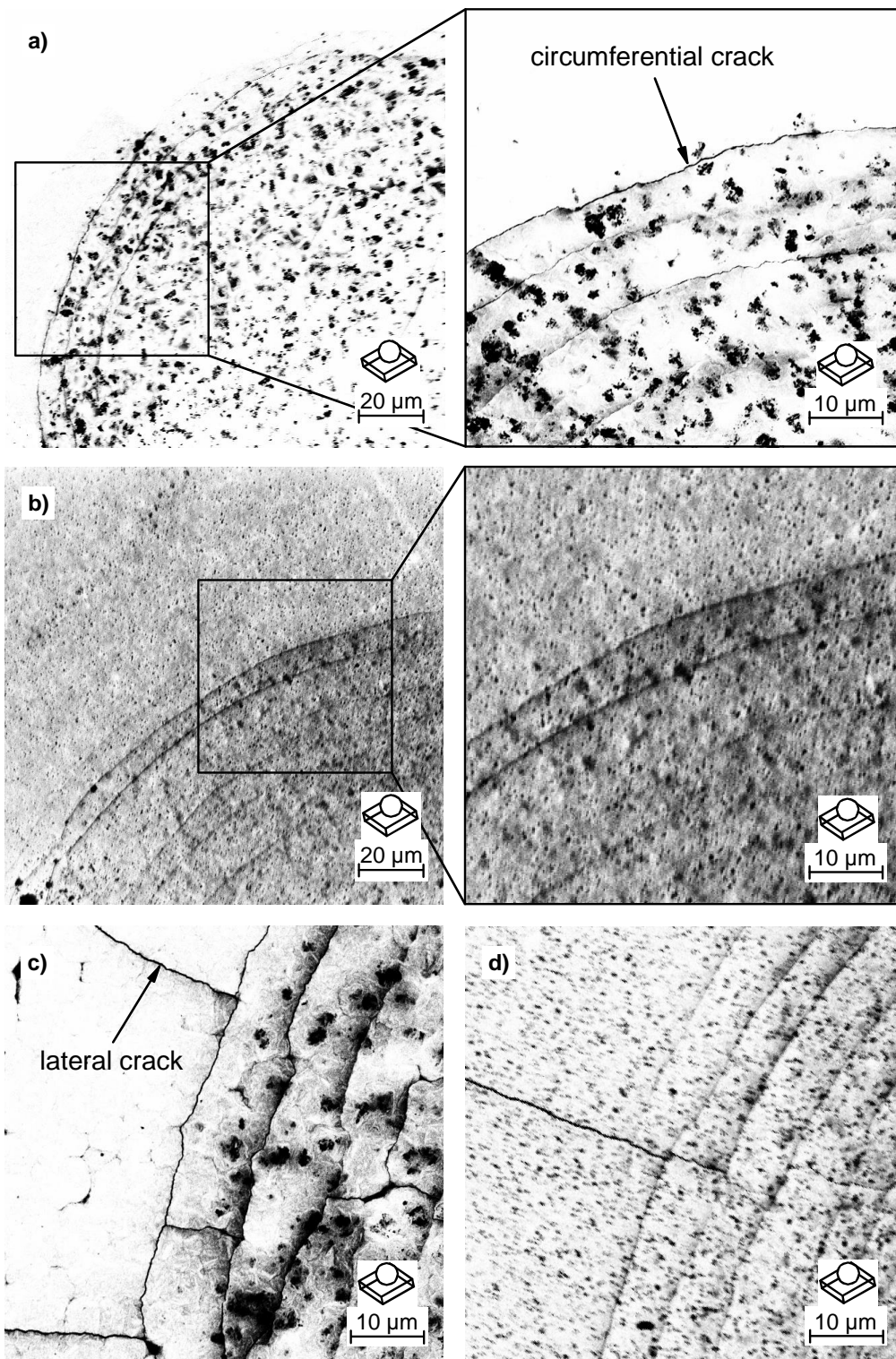


Figure 4.36 SEM image of the indentation zone that resulted by applying an indentation load of (a) 30 kgf on a diamond film, (b) 30 kgf on a homogeneous nanocrystalline diamond/ β -SiC composite film deposited, (c) 60 kgf on a diamond film, and (d) 60 kgf on a homogeneous nanocrystalline diamond/ β -SiC composite. The substrate is W. (b) and (d) represent the same film which is deposited with $F_{TMS} = 5$ sccm. (c) and (d) show the formation of lateral cracks at a load of 60 kgf which are otherwise absent in the 30 kgf case.

SEM micrographs of the indented impressions on homogeneous nanocrystalline diamond/ β -SiC composite films at higher loads (≥ 60 kgf) resemble a “shining sun” with rays. When closely examined, sections of the lateral cracks and the circumference of the indentation mark showed localized film cracking. The observed lateral cracking could possibly be due to two factors:

1. The external stresses imposed onto the coated-sample during indentation loading could effectively force the film to crack in order to dissipate stress and/or energy.
2. The underlying substrate could fail first and subsequently cause film cracking during plastic deformation at the substrate.

In any case it is observed that the films remained attached to their respective substrates.

The measured indentation fracture toughness G_c value is $0.377 \text{ MPa}\cdot\text{m}^{0.5}$ for the considered nanocomposite film. Toughening can be mainly attributed to the mechanisms such as residual stresses and crack deflection. The crack deflection can be directly interpreted by analyzing the crack evolution by SEM; greater the lateral crack length lesser the adhesion. The chemical bonds, Si-C and/or C-C are expected to ensure a better adhesion of the diamond/ β -SiC composite system. Added to it, SiC generally shows more adherence than diamond to many industrial substrates. This quality of SiC is thus expected to anchor the diamond crystallites in the composite to the substrate.

4.4 Electrical Conductivity of Diamond/ β -SiC Thin Films

The quite good linear I-V dependence obtained indicates the Ohmic contacts between silver electrodes and the samples. The scale of current increases from about 10^{-7} A to 10^{-3} A at 5 V (as shown in Fig. 4.37), which demonstrates an unambiguous decreasing trend of resistivities of the samples. I-V characteristics of film-substrate junction were measured in the voltage range of -10 V to 10 V which is shown in Fig. 4.38. There are no obvious rectifying effect observed. The transport properties of these films were investigated by Hall measurement using the Van der Pauw geometry at room temperature with a magnetic field of 0.5 T. The measurements confirmed that the diamond/ β -SiC composite films exhibited a n-type conductivity. The electron concentration of about $1.03 \times 10^{23} \text{ cm}^{-3}$ and electron mobility of $3.72 \times 10^{18} \text{ cm}^2 / \text{Vs}$ were measured. The electron mobility is considered to be due to the large amount of grain boundaries of these films. Moreover, in the case of the diamond thin film, the hole concentration is about $3.5 \times 10^{22} \text{ cm}^{-3}$ and hole mobility of $1.8 \times 10^{16} \text{ cm}^2 / \text{V s}$.

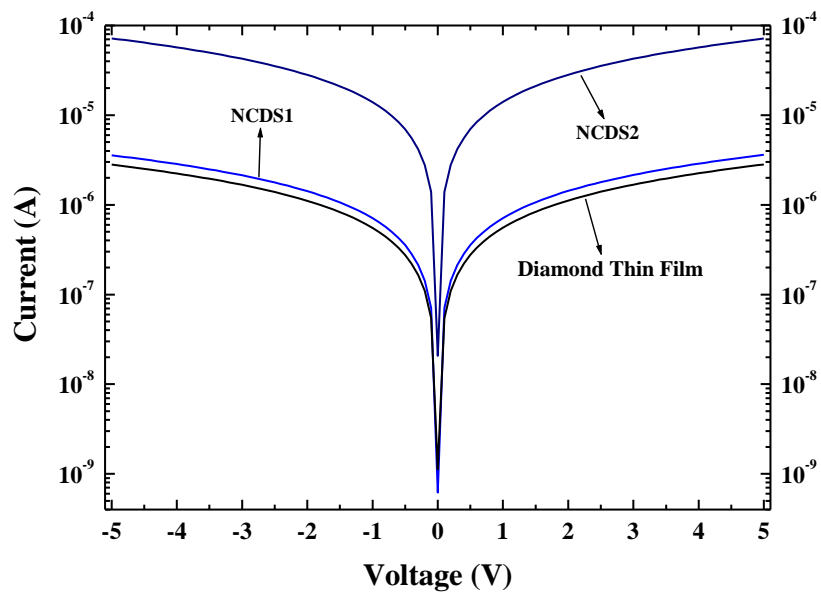


Figure 4.37 I-V characteristics of diamond/ β -SiC composite films' surfaces.

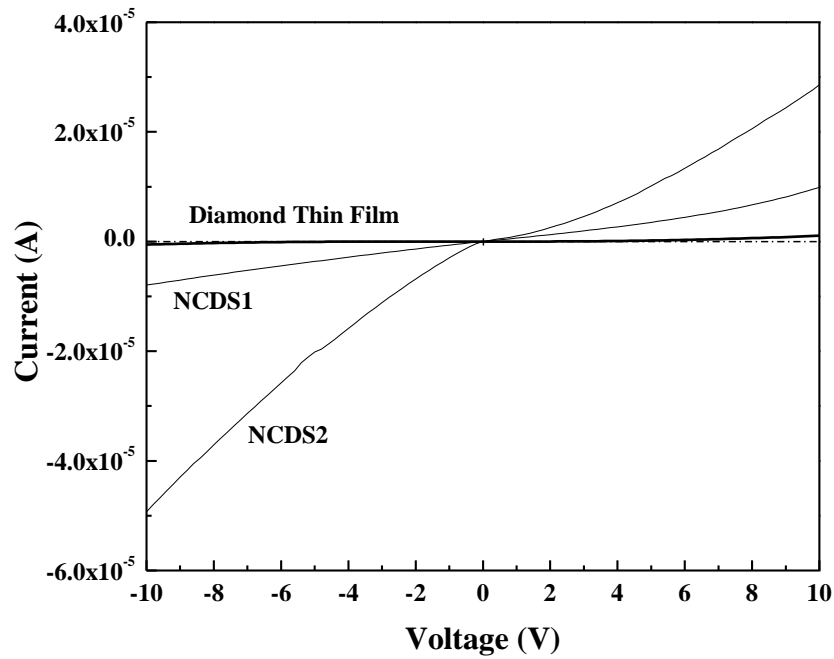


Figure 4.38 I-V characteristics of diamond/ β -SiC composite films' at thin film/substrate junction.

4.5 Si Irradiated g-C₃N₄

The plane view and cross-sectional morphology of as-synthesized graphitic carbon nitride (g-C₃N₄) are shown in Fig. 4.39. The g-C₃N₄ morphology have a typical sp² network (graphite-like layer structure) with weak Vander Walls interactions across the layers. Figure 4.40 (a) showed the X-ray diffractograms of g-C₃N₄. In g-C₃N₄, XRD showed the peaks at 2θ = ~13.5 °, ~27.5 °, ~ 44.2 ° and ~ 56.7° which are related to reflections from (100), (002), (200) and (004) crystal planes, respectively [38, 39]. The calculated inter-atomic spacing (d-spacing) corresponding to (100) and (002) reflection planes are 6.55 and 3.24 Å, respectively. Similar d-spacing values are reported in reference [40]. Fourier transform Infrared spectra obtained for synthesized g-C₃N₄ are shown in Fig. 4.40 (b). From FTIR spectrum, the peak at 808 cm⁻¹ corresponds to S-triazine ring [41-44]. Several bands in the range 1200–1650 cm⁻¹ correspond to C=N and aromatic C–N stretching modes [45,46]. The peaks at 1640, 1566, 1410 cm⁻¹ are attributed to stretching modes of heptazine derived repeating units. Furthermore, the peaks at 1319 and 1240 cm⁻¹ are assigned to the stretching modes of connected trigonal units of C–N(–C)–C or bridging C–NH–C [47]. The intensity of the peak from the g-C₃N₄ network is very strong owing to its high crystallinity.

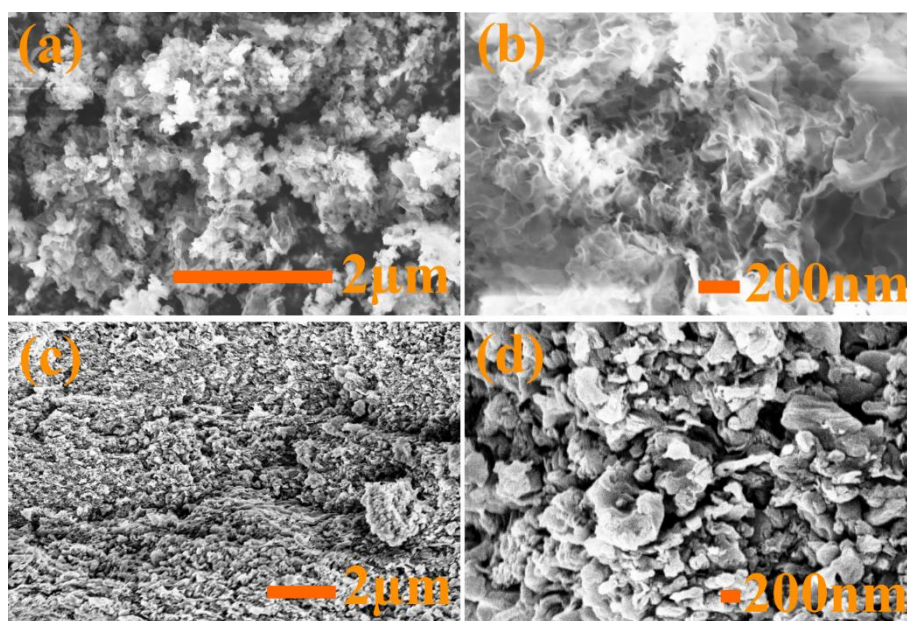


Figure 4.39 Low and high magnification plane view SE micrographs of synthesized g-C₃N₄ (a), (b) and (c), (d) are the corresponding cross-section micrographs.

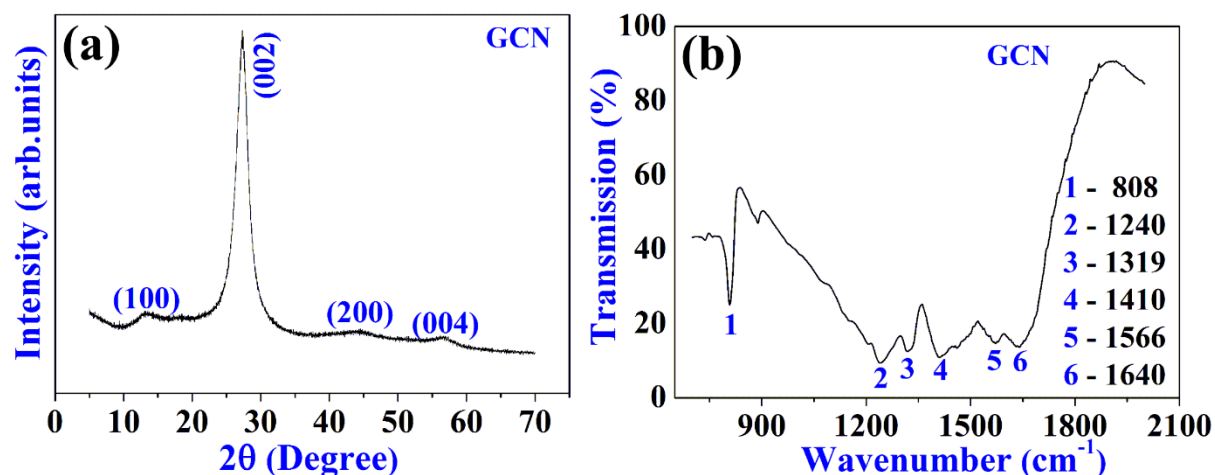
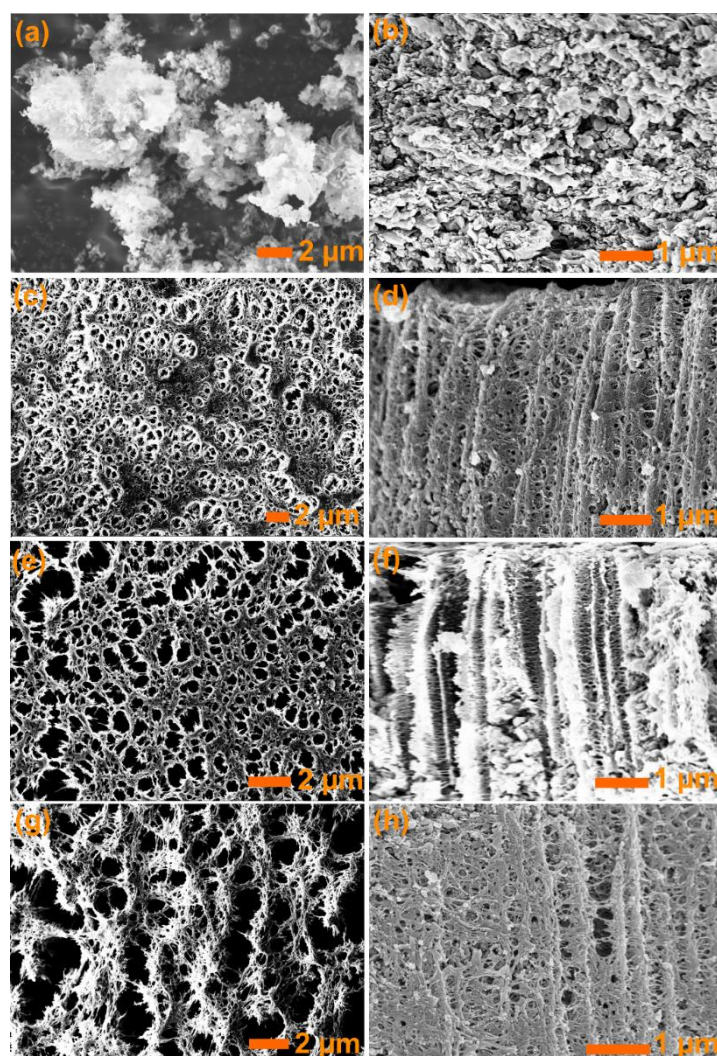


Figure 4.40 (a) X-ray diffractogram and (b) Fourier transform infrared spectrum of g-C₃N₄.

Plane-view and cross-sectional SE micrographs of pristine and Si implanted g-C₃N₄ samples with different fluencies are namely 2E15, 3E15, 5E15, 1E16, 2E16 and 3E16 ions/cm² are shown in Fig. 4.41. The corresponding Energy Dispersive X-ray spectra, X-ray diffractograms and Fourier transform Infrared spectra are shown in Fig. 4.42, 4.43 (a) and 4.43 (b).



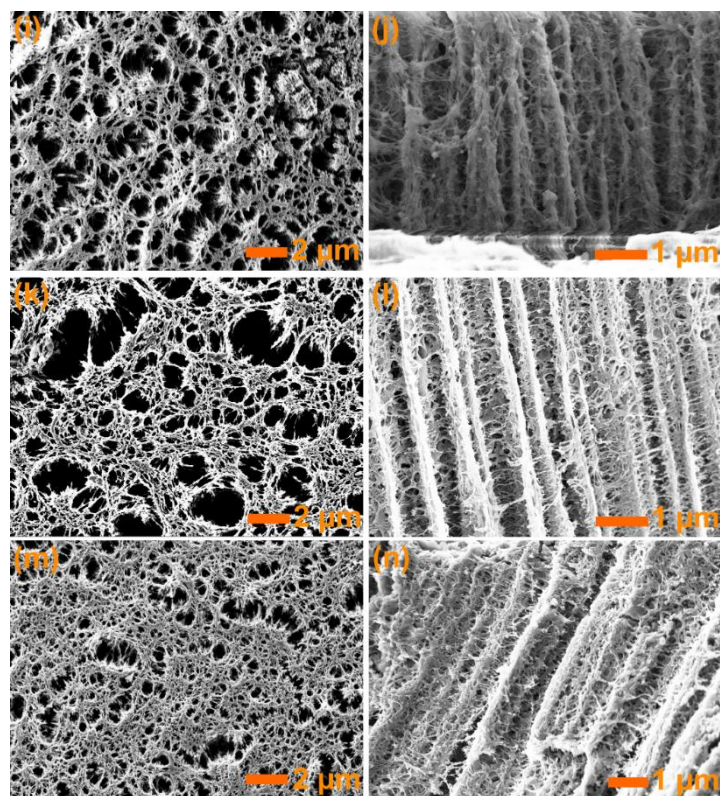


Figure 4.41 SEM plane view images of (a) pristine $g\text{-C}_3\text{N}_4$ and Si implanted $g\text{-C}_3\text{N}_4$ with fluencies of (c) $2\text{E}15$, (e) $3\text{E}15$, (g) $5\text{E}15$ (i) $1\text{E}16$, (k) $2\text{E}16$ and (m) $3\text{E}16$ Si ions/ cm^2 . The corresponding cross-sectional SEM images are (b), (d), (f), (h), (j), (l) and (n), respectively.

Implantation of Si in $g\text{-C}_3\text{N}_4$ results in the morphological and elemental changes as evident from FESEM micrographs and Energy Dispersive X-ray (EDX) analysis, respectively. From Fig. 4.41, it can be clearly revealed that the pristine $g\text{-C}_3\text{N}_4$ have original network-like surface morphology. After the Si implantation into $g\text{-C}_3\text{N}_4$, implanted surface looks like sponge which formed as sheets like morphology. Figure 4.42 showed the presence of C and N elements in pristine and $2\text{E}15$, $3\text{E}15$ ions/ cm^2 implanted $g\text{-C}_3\text{N}_4$. Also, showed the presence of Si, and C elements in $5\text{E}15$, $1\text{E}16$, $2\text{E}16$ and $3\text{E}16$ ions/ cm^2 implanted $g\text{-C}_3\text{N}_4$ and the Si content increases with an increase in fluence which is shown in table 1. This confirms that below $5\text{E}15$ ions/ cm^2 fluence Si does not implant into $g\text{-C}_3\text{N}_4$ with 200 keV Si ion beam. Figure 4.43 (a) showed the X-ray diffractograms of pristine and silicon implanted $g\text{-C}_3\text{N}_4$. Pristine samples showed the peaks at $2\theta = 13.5^\circ$, 27.5° , 44.2° and 56.7° which are related to (100), (002), (200) and (004) crystal plane reflections, respectively, in $g\text{-C}_3\text{N}_4$ [38,39].

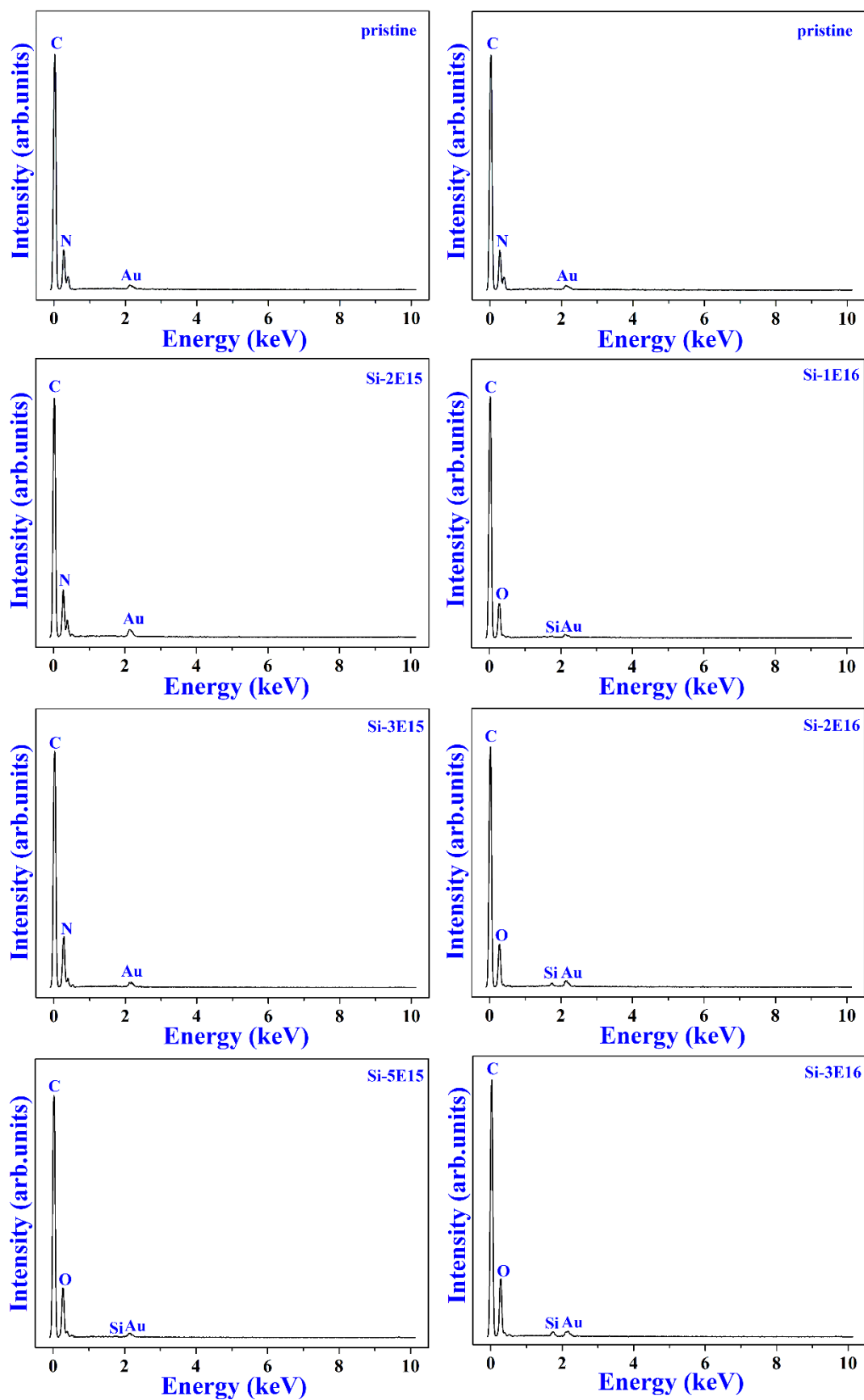
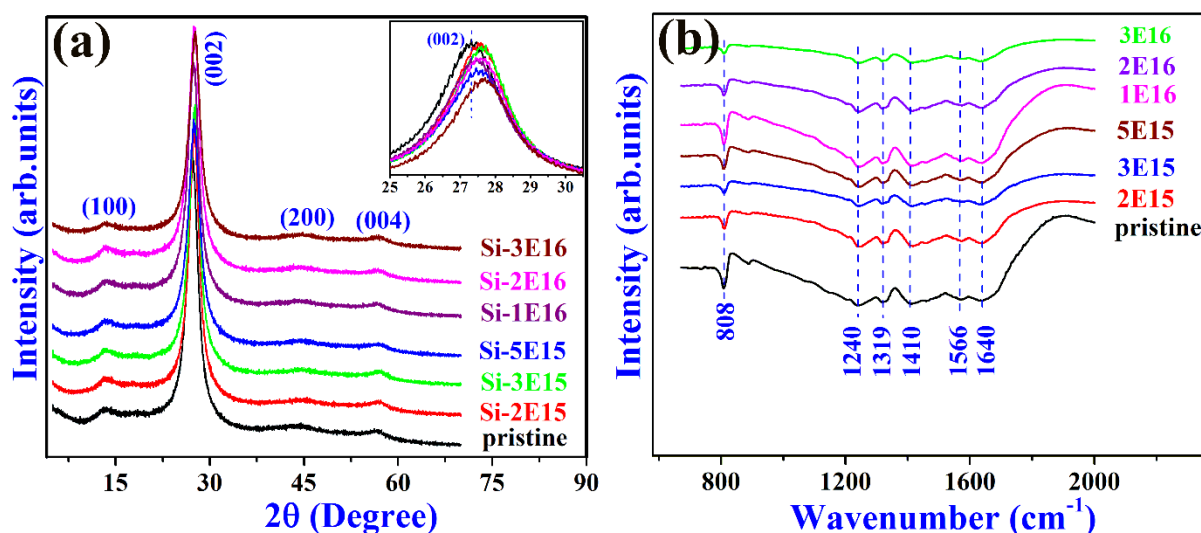


Figure 4.42 Energy dispersive X-ray spectra of pristine and Si implanted g-C₃N₄.

Table 4.2 Si atomic% variation with fluence in different samples considered in this work.

| Fluence (ions/cm ²) | Si atomic% |
|---------------------------------|------------|
| Pristine | 0 |
| 5E15 | 0.38 |
| 1E16 | 0.63 |
| 2E16 | 1.10 |
| 3E16 | 1.14 |


Figure 4.43 Pristine and silicon implanted (a) X-ray diffractograms and (b) Fourier transform infrared spectra with different fluencies.

The calculated d-spacing values corresponding to (100) and (002) reflection planes are 6.55 and 3.24 Å, respectively. There is no change in peak positions of implanted g-C₃N₄ when compared to the peak positions observed in pristine surface. By using Scherrer's formula and considering (002) (high intense) reflection peak in X-ray diffractogram, crystallite sizes are estimated. It can be seen from Fig. 4.43 (a) that the intensity of reflections from (002) planes of ion implanted g-C₃N₄ samples are almost remained the same as that of the pristine sample. This indicates that the crystallinity remained almost unchanged owing to ion plantation. However, a careful observation of the (002) reflections (inset of Fig. 4.43(a)) in an ion implanted samples showed a slight shift in their peak positions (in comparison to that of the pristine sample) towards the higher diffraction angles clearly indicates the lattice strain owing to ion implantation. X-ray diffraction reveals that silicon implantation has lattice strain effect and has no phase change in g-C₃N₄. The above mentioned observations are reflected in FTIR analysis to be discussed here. Fourier transform Infrared spectra obtained from pristine and silicon implanted g-C₃N₄ are shown in Fig. 4.43 (b). In detail, the peak at 808 cm⁻¹ represents

Results and Discussion

the S-triazine ring showing that the melon structure units were retained in the implantation treatment process. Several bands in the range 1200–1650 cm^{-1} correspond to C=N and aromatic C–N stretching modes. The peaks at 1640, 1566, 1410 cm^{-1} are assigned to stretching modes of heptazine derived repeating units. Furthermore, the peaks at 1319 and 1240 cm^{-1} are assigned to the stretching modes of connected trigonal units of C–N(–C)–C or bridging C–NH–C. Broad bands around 3000–3500 cm^{-1} are accredited to the stretching vibration of amine groups (secondary and primary amines) and their intermolecular N–H vibration [48–51]. After the Si implantation also the peaks are recorded at same wavenumber. The transmittance of implanted samples was higher in comparison to the pristine. The intensity of the peak from the g- C_3N_4 network is very strong owing to its high crystallinity.

The compositional values (Table 4.2 and FTIR spectra) show that there is no dissociation of C–N bonds. Moreover, the FTIR spectra does not show the presence of any ‘Si functional groups’ in Si-implanted g- C_3N_4 . FTIR spectra reveals that there is no distinct peak shift, any no other impurity phases and Si functional group formation has been observed after the implantation. However, the presence of Si in the implanted samples was confirmed with Fig. 4.42 (EDX). This complements well with the corresponding X-ray diffractogram and Energy dispersive x-ray spectra observations discussed earlier. Owing to the above-discussed observations, it can be strongly believed that Si is implanted in g- C_3N_4 and the implantation doping can be increased by increasing fluence.

References

- [1] S. Praver and R. J. Nemanich, *Phil. Trans. R. Soc. Lond. A* 362, 2537 (2004).
- [2] A. C. Ferrari and J. Robertson, *Phil. Trans. R. Soc. Lond. A* 362, 2477 (2004).
- [3] D. M. Gruen, *Annu. Rev. Mater. Sci.* 29, 211 (1999).
- [4] H. Kuzmany, R. Pfeiffer, N. Salk, and B. Günther, *Carbon* 42, 911 (2004).
- [5] O. A. Williams, and M. Nesládek, *Phys. Stat. sol. (a)* 203, 3375 (2006).
- [6] A. K. McQuillan, W. R. L. Clements, and B. P. Stoicheff, *Phys. Rev. A*, 1, 628 (1970).
- [7] E. Anastassakis and E. Burstein *Phys. Rev. B*, 2, 1952 (1970).
- [8] M. H. Grimsditch and A. K. Ramdas, *Phys. Rev. B*, 11, 3139 (1975).
- [9] S. A. Solin and A. K. Ramdas, *Phys. Rev. B*, 1, 1687 (1970).
- [10] A. Sawabe and T. Inuzuka, *Appl. Phys. Lett.* 46, 146 (1985).
- [11] Y. Hirose and Y. Terasawa, *Jpn. J. Appl. Phys.* 25, L519 (1986).
- [12] A. C. Ferrari and J. Robertson, *Phys. Rev. B*, 63, 121405 (R) (2001).

Results and Discussion

- [13] W. Zhu, C. A. Randall, A. R. Badzian, and R. Messier, *J. Vac. Sci. Technol. A* 7, 2315 (1989).
- [14] R. J. Nemanich, J. T. Glass, G. Lucovsky, and R. E. Shroder, *J. Vac. Sci. Technol. A* 6, 1783 (1988).
- [15] L. Fayette, B. Marcus, M. Mermoux, L. Abello, and G. Lucazeau, *Diam. Relat. Mater.* 3, 438 (1994).
- [16] H. Windischmann, G. F. Epps, Y. Cong, and R. W. Collins, *J. Appl. Phys.* 69, 2231 (1991).
- [17] J. W. Ager and M. D. Drory, *Phys. Rev. B*, 48, 2601 (1993).
- [18] V. G. Ralchenko, A. A. Smolin, V. G. Pereverzev, E. D. Obratsova, K. G. Korotoushenko, V. I. Konov, Y. V. Lakhotkin and E. N. Loubnin, *Diam. Relat. Mater.* 4, 754 (1995).
- [19] W. A. Yarbrough and R. Messier, *Science* 247, 688 (1990).
- [20] J. Lee, R. W. Collins, R. Messier, and Y. E. Strausser, *Appl. Phys. Lett.* 70, 1527 (1997).
- [21] L. C. Nistor, J. Van Landuyt, V. G. Ralchenko, E. D. Obratsova, and A. A. Smolin, *Diam. Relat. Mater.* 6, 159 (1997).
- [22] R. Pfeiffer, H. Kuzmany, P. Knoll, S. Bokova, N. Salk, and B. Günther, *Diam. Relat. Mater.* 12, 268 (2003).
- [23] A. C. Ferrari and J. Robertson, *Phys. Rev. B*, 64, 075414 (2001).
- [24] S. Reich and C. Thomsen, *Phil. Trans. R. Soc. Lond. A* 362, 2271 (2004).
- [25] F. L. Coffman, R. Cao, P.A. Pianetta, S. Kapoor, M. Kelly, and L.J. Terminello, *Appl. Phys. Lett.* 69, 568 (1996).
- [26] A. R. Konicek, D. S. Grierson, P. U. P. A. Gilbert, W. G. Sawyer, A. V. Sumant, and R. W. Carpick, *Phys. Rev. Lett.*, 100, 235502 (2008).
- [27] M. E. Drew, A. R. Konicek, P. Jaroenapibal, R. W. Carpick, and Y. Yamakoshi, *J. Mater. Chem.* 22, 12682 (2012).
- [28] S. Gupta, B. L. Weiss, B. R. Weiner, L. Pilione, A. Badzian, and G. Morell, *J. Appl. Phys.* 92, 3311 (2002).
- [29] D. Ugarte, *Chem. Phys. Lett.* 209, 99 (1993).
- [30] D. Ugarte, *Carbon* 33, 989 (1995).
- [31] H.-P. Xin, C.-L. Lin, J.-X. Wang, and S.-C. Zou, *Science In China (Series E)* 40, 361 (1997).
- [32] V.V.S.S. Srikanth and X. Jiang, *Synthesis of diamond films*, in: E. Brillas and C.A.M. Huitle (Eds.), *Synthetic Diamond Films: Preparation, Electrochemistry, Characterization and Applications*, John Wiley and Sons Inc., New Jersey, 2010, pp. 22-55.

- [33] M. K. Kuntumalla, H. Ojha, and V.V.S.S. Srikanth, *Thin Solid Films* 541, 62 (2013).
- [34] V.V. S. S. Srikanth, T. Staedler, and X. Jiang, *Diam. Relat. Mater.* 18, 1326 (2009).
- [35] V. I. Polyakova, A. I. Rukovishnikova, N. M. Rossukanyia, V. G. Pereverzevb, S. M. Pimenovb, J. A. Carlislec, D. M. Gruenc, and E. N. Loubnind, *Diam. Relat. Mater.* 12, 1776 (2003).
- [36] M. A. Abdulsattar, *Beilstein J. Nanotechnol.* 4, 262 (2013).
- [37] S. Osswald S, V. N. Mochalin, M. Havel, G. Yushin, and Y. Gogotsi, *Phys. Rev. B* 80, 075419 (2009).
- [38] Y. H. Han, J. F. Luo, C. X. Gao, H. A. Ma, A. M. Hao, Y. C. Li, X. D. Li, J. Liu, M. Li, H. W. Liu, and G. T. Zou, *Chin. Phys. Lett.* 22, 1347 (2005).
- [39] X.C. Wang, K. Maeda, A. Thomas, K. Takane, G. Xin, J.M. Carlsson, K. Domen, and M. Antonietti, *Nat. Mater.* 8, 76 (2009).
- [40] S. Matsumoto, E. Q. Xie, and F. Izumi, *Diam. Relat. Mater.* 8, 1175 (1999).
- [41] M. J. Bojdys, J. O. Muller, M. Antonietti, and A. Thomas, *Chem. Eur. J.* 14, 8177 (2008).
- [42] Y. Zhao, D. Yu, H. Zhou, Y. Tian, and O. Yanagisawa, *J. Mater. Sci.* 40, 2645 (2005).
- [43] X. Li, J. Zhang, L. Shen, Y. Ma, W. Lei, Q. Cui, and G. Zou, *Appl. Phys. A* 94, 387 (2009).
- [44] Q. Xiang, J. Yu, and M. Jaroniec, *J. Phys. Chem. C* 115, 7355 (2011).
- [45] H. J. Yan, Y. Chen, and S.M. Xu, *Int. J. Hydrogen Energy* 37, 125 (2012).
- [46] Y. Zang, L. Li, X. Li, R. Lin, and G. Li, *Chem. Eng. J.* 246, 277 (2014).
- [47] J. H. Liu, T. K. Zhang, Z. C. Wang, G. Dawson, and W. Chen, *J. Mater. Chem.* 21, 14398 (2011).
- [48] S. Kumar, T. Surendar, A. Baruah, and V. Shanker, *J. Mater. Chem. A* 1, 5333 (2013).
- [49] Y. Cao, W. Wu, S. Wang, H. Peng, X. Hu, and Y. Yu, *J. Fluoresc.* 26, 739 (2016).
- [50] Y. Shi, S. Jiang, K. Zhou, C. Bao, B. Yu, X. Qian, B. Wang, N. Hong, P. Wen, Z. Gui, Y. Hu, and R.K. Yuen, *ACS Appl. Mater. Interfaces* 6, 429 (2014).
- [51] B. Zhu, P. Xia, W.-K. Ho, and J. Yu, *Appl. Surf. Sci.* 344, 188 (2015).

Chapter 5 Conclusions and Future Scope

5.1 Conclusions

This thesis describes the systematic study of deposition as well as characterization of diamond, diamond/ β -SiC nanocomposite films. Also, the synthesis and characterization of graphene nitride (g-C₃N₄) have been studied. The diamond films and g-C₃N₄ material surfaces have been modified (i.e., structural and/or morphological) for suitable electronic and energy applications by utilizing the irradiation techniques: ion implantation/irradiation. The diamond/ β -SiC nanocomposite films mechanical and electrical characteristics also been presented. The diamond/ β -SiC nanocomposite film significantly increases the normal load bearing capacity in comparison to the diamond film before the first crack initiation in a ball-indentation-test. Also, the Hall and electrical measurements of these films showed the n-type and increased conductivity as compared to the diamond film. In this work, high and low energy facing capabilities of micro wave chemical vapor deposited (MWCVD) diamond films have been tested using gamma and ion irradiation. The surface and structural changes of gamma irradiated diamond films have been studied and showed no significant changes in them. Also, in this thesis low and high energy nitrogen ion irradiation on diamond films have been studied. The 12 keV nitrogen implanted diamond films showed no appreciable surface and structural changes. In this work, the surface and structural modifications of diamond films with 100 keV nitrogen ion implantation has been reported. The increase in sp²-C network and decrease in diamond phase purity of these implanted diamond films have been explained. Also, no new bonds like C-N, C=N, etc., are formed in these films. In this work, the high energy (70 MeV) nitrogen ion irradiation of diamond films also explained. These irradiated films did not show surface and structural changes. Similarly, no new phases are formed. The 70 MeV nitrogen ion irradiated energy was more and it penetrates through out of the diamond films without any interaction. That means the interaction time was less in this case. In this work, the silicon implantation/irradiation of graphene nitride have been studied. The morphological changes of silicon implanted g-C₃N₄ have been presented. The morphology of silicon implanted graphene nitride showed sheet like morphology with no change in phase, structure of g-C₃N₄ which can be used for energy applications. Also in this work, how the Metal-Insulator-Semiconductor (MIS) structures can be constructed on diamond films with nitrogen ion implantation has been explained. The nitrogen implanted diamond surface up to a shallow depth of 80 nm behaves as a metal. From a depth of 80 nm to the film/substrate interface, it behaves as an insulator. Silicon substrate behaves as a semiconductor. These three layers within diamond and silicon form a

Conclusions and Future Scope

film substrate system which can be used as MIS active surfaces in electronic device applications.

5.2 Future Scope

The gamma irradiation alone did not bring any surface and structural changes in MWCVD diamond films. Also, the very low energy nitrogen ion implantation (10-20 keV) did not bring any structural changes. The combination of these two irradiation may lead to surface/structural changes of these films. By increasing of the nitrogen ion implantation energy into diamond films from 100 keV to few hundreds of keV, one can get the more sp^2 C networks in implanted surfaces. So that, one can obtain much increased surface conductivity which can be used in electronic applications. The Metal-Insulator-Semiconductor (MIS) active surfaces are observed only in NCD1 film. The other two films (NCD2 and NCD3) has to characterize to check the MIS active surfaces. Also, the 100 keV nitrogen ion implantation energy was not adequate to form any kind of bonds (ex: C-N, C=N, etc) between C and N in all these diamond films (NCD1, NCD2 and NCD3). To form any kind of bonds (ex: C-N, C=N, etc) between C and N in these diamond films, energy of nitrogen ion has to increase from 100 keV. The high energy (70 MeV) nitrogen irradiated diamond films did not show any structural and these films has to anneal for knowing any structural changes. All irradiated diamond films has to anneal for defects and stress related studies. The morphological changes of silicon implanted graphene nitride is not sufficient to use this material in energy applications. The other energy based characterizations (like I-V, C-V, etc.) are also required. Also, only one energy (i.e.200 keV) is not sufficient to tell g-C₃N₄ material in energy and catalysis applications. This material has to implanted/irradiated with other energies to check the energy applications.